

1994

Numerical evaluation of corona discharge as a means of boundary layer control and drag reduction

Samir Hamza El-Khabiry
Iowa State University

Follow this and additional works at: <https://lib.dr.iastate.edu/rtd>

 Part of the [Aerospace Engineering Commons](#), and the [Mechanical Engineering Commons](#)

Recommended Citation

El-Khabiry, Samir Hamza, "Numerical evaluation of corona discharge as a means of boundary layer control and drag reduction " (1994). *Retrospective Theses and Dissertations*. 10696.
<https://lib.dr.iastate.edu/rtd/10696>

This Dissertation is brought to you for free and open access by the Iowa State University Capstones, Theses and Dissertations at Iowa State University Digital Repository. It has been accepted for inclusion in Retrospective Theses and Dissertations by an authorized administrator of Iowa State University Digital Repository. For more information, please contact digirep@iastate.edu.

1

95

03549

U·M·I

MICROFILMED 1994

INFORMATION TO USERS

This manuscript has been reproduced from the microfilm master. UMI films the text directly from the original or copy submitted. Thus, some thesis and dissertation copies are in typewriter face, while others may be from any type of computer printer.

The quality of this reproduction is dependent upon the quality of the copy submitted. Broken or indistinct print, colored or poor quality illustrations and photographs, print bleedthrough, substandard margins, and improper alignment can adversely affect reproduction.

In the unlikely event that the author did not send UMI a complete manuscript and there are missing pages, these will be noted. Also, if unauthorized copyright material had to be removed, a note will indicate the deletion.

Oversize materials (e.g., maps, drawings, charts) are reproduced by sectioning the original, beginning at the upper left-hand corner and continuing from left to right in equal sections with small overlaps. Each original is also photographed in one exposure and is included in reduced form at the back of the book.

Photographs included in the original manuscript have been reproduced xerographically in this copy. Higher quality 6" x 9" black and white photographic prints are available for any photographs or illustrations appearing in this copy for an additional charge. Contact UMI directly to order.

U·M·I

University Microfilms International
A Bell & Howell Information Company
300 North Zeeb Road, Ann Arbor, MI 48106-1346 USA
313/761-4700 800/521-0600



Order Number 9503549

**Numerical evaluation of corona discharge as a means of
boundary layer control and drag reduction**

El-Khabiry, Samir Hamza, Ph.D.

Iowa State University, 1994

U·M·I

300 N. Zeeb Rd.
Ann Arbor, MI 48106



**Numerical evaluation of corona discharge as a means of boundary layer control
and drag reduction**

by

Samir Hamza El-Khabiry

A Dissertation Submitted to the
Graduate Faculty in Partial Fulfillment of the
Requirement for the Degree of
DOCTOR OF PHILOSOPHY

Department: Mechanical Engineering
Major: Mechanical Engineering

Approved:

Signature was redacted for privacy.

In Charge of Major Work

Signature was redacted for privacy.

~~For the Major Department~~

Signature was redacted for privacy.

~~For the Graduate College~~

**Iowa State University
Ames, Iowa**

1994

TABLE OF CONTENTS

LIST OF TABLES	vi
LIST OF FIGURES	vii
NOMENCLATURE	xii
ACKNOWLEDGMENTS	xiv
1. INTRODUCTION	1
1.1 Corona Discharge	1
1.1.1 Commercial uses of corona	2
1.2 Boundary Layer Structure	3
1.2.1 Drag reduction	4
1.3 Literature Review	6
1.4 Scope of the Present Study	10
2. DESCRIPTION OF THE PHYSICAL MECHANISMS	12
2.1 Corona Polarity	13
2.1.1 Positive corona	13
2.1.2 Negative corona	14
2.2 Corona Setup	14
2.3 Drag	15
2.4 Mechanism of Drag Reduction by Corona Discharge on a Flat Plate	15
2.5 Surface Conductivity of Glass	18
2.6 Modeling of the Present Study	20
2.6.1 Study case 1	20
2.6.2 Study case 2	21

4.1.1	Boundary layer equations	52
4.1.2	Electrostatic equations	53
4.2	Appropriate Computational Domain	54
4.3	Clustered Grid	55
4.3.1	Interpolation scheme	60
4.4	Finite Differencing	61
4.4.1	Integration scheme	69
4.4.2	Thomas algorithm	71
4.4.3	Convergence criteria	72
4.4.4	Stability condition of five-point scheme	73
4.4.5	Relaxation scheme	73
4.5	Drag Calculations	74
4.6	Computational Procedure	75
4.7	Computational Parameters	81
5.	RESULTS AND DISCUSSION	83
5.1	Corona Discharge	83
5.1.1	Corona onset voltage	83
5.1.2	Corona current	85
5.1.2.1	Seaver's equation and Soetomo's data	85
5.1.3	Boundary conditions of the charge density at the interface ..	92
5.1.4	Electrostatic study cases	92
5.1.4.1	Study case 1	92
5.1.4.2	Study case 2	101
5.2	Corona Effect on Boundary-Layer	112
5.3	Corona Effect and Drag Reduction	130

5.4	Stability Conditions	140
5.5	Relaxation Scheme	141
6.	CONCLUSIONS	142
	REFERENCES	145
APPENDIX A	EFFECTIVE ELECTROMAGNETIC FORCE ON CHARGED PARTICLES	151
APPENDIX B	CORONA CURRENT	154
APPENDIX C	DERIVATION OF BOUNDARY LAYER EQUATIONS WITH CORONA DISCHARGE	158
APPENDIX D	ANALYTIC SOLUTION OF CHARGE DENSITY AT THE INTERFACE BETWEEN THE TWO ELECTRODES FOR OHMIC SURFACE	165
APPENDIX E	ELECTRIC POTENTIAL DISTRIBUTION AT THE EXTENSION OF THE FLAT PLATE	170
APPENDIX F	DRAG FORCE BY MOMENTUM INTEGRAL METHOD ..	174
APPENDIX G	PHYSICAL PARAMETERS	177

LIST OF TABLES

Table 4.1:	Non uniform grid analysis	58
Table 4.2:	Zeros and weights for Gauss quadrature	71
Table 5.1:	Output results for study case 2 with $U = 3.0$ m/sec	118
Table 5.2:	Boundary layer information without corona effect (Stretching parameter = 1.05)	126
Table 5.3:	Output results for various flow velocities ($\Delta \phi = 4000$ volts, $L = 25$ mm, $L_3 = 25$ mm)	131
Table 5.4:	Stability conditions	140
Table B.1:	Soetomo's current-voltage measurements	154

LIST OF FIGURES

Figure 2.1:	Mutual effect between the plate and the fluid flow	16
Figure 2.2:	Model setup	17
Figure 2.3:	Corona discharge effect on velocity profile and resulting thrust force on the plate	19
Figure 2.4:	Force acting on the positive electrode due to repelling action of the positive ions	19
Figure 3.1:	Magnetic field due to electric current	26
Figure 3.2:	Surface current along a dielectric plate	38
Figure 3.3:	Surface current with ion-deposition contribution	41
Figure 4.1:	Grid spacing vs stretching parameter	59
Figure 4.2:	Non uniform grid general view	62
Figure 4.3:	General algorithm of the numerical solution	78
Figure 5.1:	Corona onset voltage for various corona wire sizes at different gap lengths between electrodes	84
Figure 5.2:	Fitting of Soetomo's data into Seaver's equation for $d_s=2.0 \mu m$, $L=25.0 mm$, $L_2=28.0 mm$, $V_0=680.27 volts$ (Seaver's equation coefficients; $a_0=0.365 [kV]^{-1}$, $b=7615 [mA]^{-1}$)	86
Figure 5.3:	Corona current due to 2- μm -diameter corona wire for various potential differences and gap lengths between electrodes	87
Figure 5.4:	Corona current due to 10- μm -diameter corona wire for various potential differences and gap lengths between electrodes	88
Figure 5.5:	Corona current due to 50- μm -diameter corona wire for various potential differences and gap lengths between electrodes	89
Figure 5.6:	Corona current due to 100- μm -diameter corona wire for various potential differences and gap lengths between electrodes	90

Figure 5.7:	Corona current due to 500- μm -diameter corona wire for various potential differences and gap lengths between electrodes	91
Figure 5.8:	Numerical solution versus analytic solution of the charge density distribution at the interface between the two electrodes	93
Figure 5.9:	Electric potential distribution at different levels above the surface with ion deposition to surface ($U = 0.0$ m/sec, corona wire is upstream) .	95
Figure 5.10:	Electric potential distribution at different levels above the surface with no ion deposition to surface ($U = 0.0$ m/sec, corona wire is upstream)	96
Figure 5.11:	Vector plot of electric field strength at different levels above the surface with gas phase current and ion deposition to surface ($U = 0.0$ m/sec, corona wire is upstream)	97
Figure 5.12:	Vector plot of electric field strength at different levels above the surface with gas phase current and no ion deposition to surface ($U = 0.0$ m/sec, corona wire is upstream)	98
Figure 5.13:	Charge density distribution at different levels above the surface between the two electrodes with ion deposition to surface ($U = 0.0$ m/sec, corona wire is upstream)	99
Figure 5.14:	Charge density distribution at different levels above the surface between the two electrodes with no ion deposition to surface ($U = 0.0$ m/sec, corona wire is upstream)	100
Figure 5.15:	Corona current to predicted corona current ratio across control surfaces around the corona wire between the two electrodes with ion deposition to surface ($U = 0.0$ m/sec, corona wire is upstream) .	102
Figure 5.16:	Vector plot of current density at different levels above the surface between electrodes with ion deposition to surface ($U = 0.0$ m/sec, corona wire is upstream)	103
Figure 5.17:	Vector plot of current density at different levels above the surface between electrodes with no ion deposition to surface ($U = 0.0$ m/sec, corona wire is upstream)	104
Figure 5.18:	Electric potential distribution at different levels above the surface with ion deposition to surface ($U = 0.0$ m/sec, corona wire is upstream) .	106

Figure 5.19:	Electric potential distribution at different levels above the surface between electrodes with ion deposition to surface (U = 0.0 m/sec, corona wire is upstream)	107
Figure 5.20:	Electric potential distribution at different levels above the surface with no ion deposition to surface (U = 0.0 m/sec, corona wire is upstream)	108
Figure 5.21:	Electric potential distribution at different levels above the surface between electrodes with no ion deposition to surface (U = 0.0 m/sec, corona wire is upstream)	109
Figure 5.22:	Vector plot of electric field strength at different levels above the surface with gas phase current and ion deposition to surface (U = 0.0 m/sec, corona wire is upstream)	110
Figure 5.23:	Vector plot of electric field strength at different levels above the surface with gas phase current and no ion deposition to surface (U = 0.0 m/sec, corona wire is upstream)	111
Figure 5.24:	Charge density distribution at different levels above the surface between the two electrodes with ion deposition to surface (U = 0.0 m/sec, corona wire is upstream)	113
Figure 5.25:	Charge density distribution at different levels above the surface between the two electrodes with no ion deposition to surface (U = 0.0 m/sec, corona wire is upstream)	114
Figure 5.26:	Corona current to predicted corona current ratio across control surfaces around the corona wire between the two electrodes with ion deposition to surface (U = 0.0 m/sec, corona wire is upstream)	115
Figure 5.27:	Vector plot of current density at different levels above the surface between electrodes with ion deposition to surface (U = 0.0 m/sec, corona wire is upstream)	116
Figure 5.28:	Vector plot of current density at different levels above the surface between electrodes with no ion deposition to surface (U = 0.0 m/sec, corona wire is upstream)	117
Figure 5.29:	Velocity profiles without and with corona effect with ion deposition to surface at 3.0 mm downstream of the corona wire (U = 3 m/sec, corona wire is upstream)	119

Figure 5.30:	Velocity profiles without and with corona effect with ion deposition to surface at 13.0 mm downstream of the corona wire (U =3 m/sec, corona wire is upstream)	120
Figure 5.31:	Velocity profiles without and with corona effect with ion deposition to surface at the edges of the corona strip (U =3 m/sec, corona wire is upstream)	122
Figure 5.32:	Local shear stress without and with corona effect with ion deposition to surface (U =3 m/sec, corona wire is upstream)	123
Figure 5.33:	Local skin friction coefficient without and with corona effect with ion deposition to surface (U =3 m/sec, corona wire is upstream) ...	124
Figure 5.34:	Boundary-layer thickness without and with corona effect with ion deposition to surface (U =3 m/sec, corona wire is upstream)	125
Figure 5.35:	Ratio of body force components between the two electrodes at different levels above the surface (U =3 m/sec, corona wire is upstream) ...	128
Figure 5.36:	Vector plot of current density at different levels above the surface between electrodes with ion deposition to surface (U =3 m/sec, corona wire is upstream)	129
Figure 5.37:	Corona effect on drag forces based on momentum and shear vs Reynolds number with ion deposition to surface and corona wire is upstream ($\Delta \phi =4000$ volts, $L=25$ mm, $L_3=25$ mm, $d_s=2$ μ m)	132
Figure 5.38:	Corona effect on drag force based on shear vs Reynolds number with ion deposition to surface and corona wire is upstream ($\Delta \phi =4000$ volts, $L=25$ mm, $L_3=25$ mm, $d_s=2$ μ m)	133
Figure 5.39:	Corona effect on drag coefficient based on momentum and shear vs Reynolds number with ion deposition to surface and corona wire upstream ($\Delta \phi =4000$ volts, $L=25$ mm, $L_3=25$ mm, $d_s=2$ μ m)	135
Figure 5.40:	Corona effect on percentage drag reduction based on momentum vs Reynolds number for various potential difference between electrodes with ion deposition to surface and corona wire is upstream ($L=25$ mm, $L_3=25$ mm, $d_s=2$ μ m)	136

Figure 5.41:	Corona effect on percentage drag reduction based on momentum vs Reynolds number for various gap length between electrodes with ion deposition to surface and corona wire is upstream ($\Delta \phi = 4000 \text{ volts}$, $L_3 = 25 \text{ mm}$, $d_s = 2 \mu\text{m}$)	137
Figure 5.42:	Corona effect on percentage drag reduction based on momentum vs Reynolds number for various locations of the corona setup downstream from plate leading edge with ion deposition to surface and corona wire is upstream ($\Delta \phi = 4000 \text{ volts}$, $L = 25 \text{ mm}$, $d_s = 2 \mu\text{m}$)	138
Figure 5.43:	Corona effect on percentage drag reduction based on momentum vs Reynolds number for various corona wire diameters with ion deposition to surface and corona wire is upstream ($\Delta \phi = 4000 \text{ volts}$, $L = 25 \text{ mm}$, $L_3 = 25 \text{ mm}$)	140
Figure E.1:	Transformation of (x', y') plane to (x, y) plane	170
Figure F.1:	Control volume on a flat plate	174

NOMENCLATURE

Some of the key variables used in this dissertation are listed below. Where appropriate, some symbols may have more than one meaning.

A	Area
\vec{B}	Magnetic field intensity
C_f	Local skin friction coefficient
C_D	Drag coefficient
D	Drag force
$DR\%$	Percentage drag reduction
d_s	Corona wire diameter
\vec{E}	Electric field strength
E_c	Critical electric field strength
\vec{F}	Body force due to corona discharge
f	Geometric factor
h	Computational domain height
I	Corona current
I_c	Predicted corona current
\vec{i}	Unit vector along x-axis
\vec{J}	Electric current density
k	Ion mobility
K	Dielectric constant of glass
L	Gap length between electrodes
L_1	Distance downstream of plate leading edge where b. l. equations are valid
L_2	Length of electrode used by Soetomo
L_3	Distance between plate leading edge and upstream electrode
L_4	Distance between downstream electrode and end of computational domain
\vec{l}	Unit vector
N	Newton
n	Number of ions per unit volume
p	Pressure
q	Ion charge

Re_L	Reynolds number based on L
Re_x	Reynolds number based on distance "x" measured from plate leading edge
R	Resistance
R'	Surface resistivity
S_n	Dimensionless number
t	Time
U	Free stream velocity
\bar{u}	Fluid velocity
V_o	Corona onset voltage
\bar{v}	Ion drift velocity
x	Distance measured along positive direction of x-axis
y	Distance measured along positive direction of y-axis
β	Stretching parameter
δ	Boundary-layer thickness
ϕ	Electric potential
ϵ_o	Permittivity of free space
σ_c	Bulk electric conductivity
σ_{cs}	Surface electric conductivity
ρ_c	Electric charge density per unit volume
ρ_{co}	Electric charge density at the corona wire
ρ	Density of air
μ	Dynamic viscosity of air
ν	Kinematic viscosity of air
μ_o	Permeability of free space
τ	Shear stress

ACKNOWLEDGMENTS

I wish to express my sincere gratitude to my major professor, Dr. Gerald M. Colver, for his support, patience and guidance during my Ph.D. program. I greatly appreciate the invaluable advice and inspiration that he provided throughout this dissertation. I also wish to extend my gratitude to Dr. Richard H. Pletcher, Dr. Bruce R. Munson, Dr. Ambar K. Mitra, and Dr. Bruce N. Harmon for their willingness to be committee members and for their valuable discussions and suggestions. I also extend my gratitude to Dr. Joseph M. Prusa in Mechanical Engineering for his invaluable advice and discussions during the numerical part of this study and for his acceptance to act as a committee member during the defense of this dissertation. I am also grateful to the Department of Mechanical Engineering for my teaching assistantship to complete my graduate study, through which I learned a lot as an instructor.

I have a list of unforgettable names who have helped me in innumerable ways: Dr. James F. Hoburg in the Department of Electrical and Computer Engineering, Carnegie-Mellon University for his helpful discussions. Dr. William J. Cook in Mechanical Engineering for his encouragement and guidance. Mr. Frank A. Poduska in Durham Computation Center for his helpful discussions to resolve problems with the computer. My colleagues Thomas H. Ramin and Jiun-Shen Wang in room 210 ERI for their discussions.

I wish to thank my dear parents specially my father who passed away during the course of this study for their never-ending love and sacrifices for my family and me. I am also grateful to other families, relatives and friends for their concern and encouragement.

Special thanks to my wife, Sohair: I am heartily indebted to her for her unselfish love and sacrifices. Her unfailing support and faith make this dissertation possible.

Finally, our two kids, Howaida and Ehab: I am indebted to them for the time they deserve from me and always not available. Both of them have been the greatest source of happiness for both of us. We wish them to grow in God, to whom we express our thanks.

1. INTRODUCTION

The objective of this study is to evaluate numerically the effect of corona discharge as a means of drag reduction and boundary layer control on a flat plate. To accomplish this objective a coupling between electrostatics and fluid mechanics must be considered. A physical understanding of both the corona discharge phenomenon and the boundary layer fluid flow phenomenon is first achieved. Following this a comprehensive literature survey is given. Based on this review, a mathematical description of the effect of corona discharge on boundary layer flow is obtained as a set of five partial differential equations. These partial differential equations are coupled and solved simultaneously. A finite difference approach is used for the numerical solution of this model.

1.1 Corona Discharge

Corona is a type of localized discharge resulting from transient gaseous ionization in an insulation system when the voltage stress exceeds a critical value. This ionization process is taken to be localized over only a portion of the distance between the electrodes of the system. Corona discharge is familiar as an impressive glow surrounding the conductors suspended between the towers of high-voltage transmission lines.

Corona discharge occurs only in a gas and not in a solid or liquid. Corona consumes power as a high voltage and a low current. Corona discharges do not necessarily take place between a pair of conducting electrodes or surfaces.

Corona discharge can produce light, audible noise, and ozone, which are detectable by sensory capabilities of sight, hearing, and smell. In addition, corona discharge gives rise to other effects, such as [1]:

- 1- Ultraviolet radiation.
- 2- Nascent oxygen, also a strong oxidizing agent, as is ozone.

- 3- Nitric acid in the presence of moisture.
- 4- Heat generation in the discharge channel and power loss in the power supply.
- 5- Mechanical erosion of surfaces by ion bombardment.
- 6- Electric wind that blows in the direction of the traveling charged species.
- 7- Interference with radio communication within the usual broadcast band frequency spectrum.

With such effects as specially those leading to chemical and mechanical destruction of adjacent materials, it is readily seen that corona discharges are undesirable and it is preferred to be avoided for its destructive effects. On the other hand, corona discharges, on the basis of these very same properties, perform important commercial services in many areas ranging from xerography to ore separations.

1.1.1 Commercial uses of corona

Surprisingly, corona discharge enters into a large number of practical uses. However the general public is probably not familiar with these uses or the part that corona plays in them. Some of these uses can be listed here.

1- Lightning rods: A pointed ground rod produces ions under high-voltage gradients that exist during thunderstorms. These discharges help neutralize and reduce such gradients so the lightning is prevented from striking in the vicinity of the pointed rod.

2- Printing treatment of plastic films: Thin extruded films such as polyethylene refuse to be wetted by conventional printing inks which makes durable printing impossible. Instead if the film is run between two cylindrical electrodes and corona exists in the air gap (due to an r-f source of high voltage between the two cylinders) the chemical action of the corona on the polymer surface is modified by oxidation to a composition that inks will wet.

3- Electrostatic separation of ores: Many plants are using the effect of corona to separate conducting and non-conducting particles when the conducting particles are charged and adhere to a rotating of opposite charge roll that can be brushed later while the non-conducting particles are not adhering to this roll and can be separated.

4- Ozone generators: When oxygen is passed between two coaxial glass tubes at high potential difference ozone will be generated.

5- Electrostatic precipitator: When a gas carrying particles is made to pass between parallel plates which are maintained at sufficient d-c potential difference the particles are electrically charged and traveled towards one or the other of the plates and deposited where can be collected later. Electrostatic precipitators are used in industry to collect emissions such as fly ash, soot, or other entrained particles from the gases in stacks to prevent their discharge into the atmosphere for a cleaner environment.

6- Xerography: This process is too complicated to discuss in details but the first step is to distribute a uniform layer of static charge over the surface of the light-sensitive plate. This is done by a corona generating technique.

7- Ionic wind: When corona discharge takes place between two electrodes, the high speed traveling ions transfer momentum to the neutral particles creating what is known as the ionic wind. This ionic wind can help in reducing the total drag on a moving body and also can help in boosting heat transfer in some applications.

8- Enhance heat transfer: Corona discharge increases heat transfer at low velocities but this gain in heat transfer decreased to zero at high velocities [2].

1.2 Boundary Layer Structure

The character of the flow field around an object depends very strongly on its shape, size, orientation, speed, and fluid properties. Recall that the Reynolds number represents the

ratio of inertial effects to viscous effects, most external flows with very small Reynolds number are dominated by viscous effects while those with moderate and high Reynolds number are dominated by inertial effects. In low Reynolds number flows the viscous effects are effective far from the object in all directions but as the Reynolds number is increased the region in which viscous effects are important becomes smaller except downstream. In high Reynolds number flows the flow is dominated by inertial effects and the viscous effects are negligible everywhere except in a region very close to the object. Since the fluid viscosity is not zero, it follows that the fluid must stick to the solid surface (the no-slip boundary condition). There is a thin boundary layer region next to the object in which the fluid velocity changes from the upstream value to zero velocity on the object surface. The thickness of this layer increases in the direction of the flow starting from zero at the leading edge of the object. The boundary layer flow on a flat plate is governed by a balance between shear drag and a decrease in the momentum of the fluid. The flow within the boundary layer may be laminar or turbulent depending on various parameters involved [3].

1.2.1 Drag reduction

Previous research on "form" or "pressure" drag reduction decreased the drag coefficient of most air and underwater bodies to very low values. In fact, skin friction or viscous drag is currently considered as a major barrier to the further optimization of most aerodynamic and hydrodynamic bodies. Viscous drag represents a significant part of the total drag and its value varies from application to application. The order of the skin-friction drag is 30-40% for high-speed aircraft including aerospace planes and missiles, 50% for transport aircraft and cruise missiles, 70% or greater for most underwater bodies, and nearly 100% for long-distance pipelines. Small viscous drag reductions can have a tremendous economic impact if a large number of units are involved. For example, 5-10% viscous drag

reduction of the U.S. domestic airline fleet could save the order of half a billion dollars per year [4]. Lower drag can result in increased range, reduced fuel volume and usage, reduced vehicle size and weight, increased speed and payload, and/or greater acceleration and maneuverability. For these reasons, intense research to reduce this drag is still in progress.

Viscous drag reduction depends on the viscous flow over the bulk of the body whether it is laminar or turbulent. There are three different categories which can be described here as follows [4]:

1- Laminar flow: The body Reynolds number is relatively low (order of 10^6 or less) and no transition promoters are existing such as adverse pressure gradient, three-dimensional flow, roughness, waviness, and stream disturbances. In this case the boundary-layer flow is laminar and the viscous drag-reduction problem is one of reducing laminar skin friction.

Applicable techniques include:

a- Reducing the tangential momentum accommodation coefficient, e.g., introducing a slip velocity at the surface.

b- Use of convex longitudinal curvature.

c- Adverse longitudinal pressure gradients.

d- Fluid injection through the wall .

2- Transition flow: The body Reynolds number ranges from 10^6 to 10^7 . In this regime large portions of the body can be subjected to transitional flow and the obvious drag-reduction ploy is to delay the start of this transition process as long as possible. Typical techniques include:

a- Wall suction.

b- Favorable pressure gradient.

c- Wall heating (in water) or cooling (in air) .

3- Turbulent flow: The body Reynolds number is greater than 10^7 and the boundary-layer flow is turbulent and the viscous drag-reduction problem is one of alteration of the turbulence structure. This regime is of a great interest since it has many technological applications including high speed airplanes, spacecrafts, and missiles. Indeed, the area of turbulent drag reduction could be looked upon as part of a larger discipline termed "turbulence control". Applicable techniques include [4,5,6]:

a- Reduction of the near-wall longitudinal momentum by using adverse pressure gradient, wall mass transfer, ion wind, and boundary layer thickeners.

b- Alteration of the outer region turbulence structure by using large eddy breakup devices, local suction within the boundary layer, modification of Emmons spot formation.

c- Alteration of the wall boundary conditions by using riblets, relaminarization by massive wall suction, and bubbles (for liquids).

d- Use of a stabilizing body force by using convex curvature, MHD control, and wall cooling.

1.3 Literature Review

Over the years, the concept of corona discharge (and ionic wind) has found several engineering applications in heat and mass transfer problems [2,6,7,8,9,10]. For instance, it has been observed that proper generation of ion wind could augment heat transfer up to 200 percent [7]. Velkoff reported that the enhanced heat transfer with corona wind-free convection also exists at low air velocities over a flat heated plate under the condition that the stream velocity is of the order of the corona-wind velocity or less [2]. Kibler and Carter [10] have shown that electrocooling is an ionic drag phenomenon in which the convective heat-transfer coefficient is proportional to the fourth root of corona current and they also concluded that the electrocooling, as a particular type of forced convection, may be directly

compared with conventional mechanical devices such as blowers and air jets. Corona discharge has been used effectively in electrostatic precipitators which are used to control emissions of dusts, fumes, and mists from industrial furnaces and process gases. This emission control is essential to prevent heavy, devastating air pollution and to recover valuable materials such as copper, lead, and gold which may be lost by dispersion into the atmosphere [11,12,13,14,15]. Many experimental and computational researches have been conducted to improve the design and efficiency of electrostatic precipitators. Computationally, researchers obtained results which agree with experimental data by solving the charge continuity equation and Poisson's equation by making use of an iterative numerical procedure based on finite element techniques [16,17,18,19]. Lawton [20], and Weinberg [21] have conducted investigations on high voltage discharge in combustion and flame control. They found that the ion wind effects can be used to modify flame shape and stability, rates of flame propagation, entrainment of air into fuel, combustion intensity, heat transfer from flames to solid surfaces, and rates of flame spread in solid propellants. The corona discharge is a new technique for drag reduction. The problem is a difficult one in view of the scanty knowledge of the physics of corona discharge near a surface and requires further investigation [6,7,9]. Colver and Nakai [22] have qualitatively investigated the effect of corona discharge on a boundary layer near a semi-insulated wall, such as a hot glass, using a flame as a visual indicator. They observed that the electrical conductivity of the wall has a significant influence on the discharge and consequently on the momentum added to the boundary layer. The resulting ionic wind, which has an average velocity of several meters per second [6,7], will contribute to the momentum of the retarded flow inside the boundary layer in a way to reduce the total drag. Malik, et al. [7] conducted theoretical and experimental investigation on the effect of ion wind on viscous drag. The theoretical and experimental results agreed in indicating drag reductions of the order of 20 percent for an

applied voltage of 15 kV in plane Poiseuille flow at low speeds (compared to or less than the ion drift velocity). They also calculated laminar boundary layer flow with corona effect and their results did not show any such reductions and they explained that as a result of the lack of knowledge of physics of corona near an insulated surface. Chapman and Wintle [23] studied the transport of electric charge across the surface of insulators and they refer that to the humid environments which lead to monolayer or multilayer deposits of water on the surface and consequently the surface conductivity is then due to the water is ohmic and presumably electrolytic in nature. In their study, they considered only surface current and no electric charges are existing in the bulk space above the surface. They reported that in the steady state conditions $E_x E_y = \text{Constant}$ where E_x and E_y are the components of the electric field along and perpendicular to the surface between the two electrodes and consequently they concluded that the surface-charge-limited current is proportional to the square of the applied voltage. Sigmond and Goldman [24] reported the same results in a review paper of some developments of importance to the understanding of gas and surface phenomena. Soetomo [25] investigated experimentally the effect of corona discharge on a flat plate made of glass with finite surface conductivity in a low speed wind tunnel. In his experimental model, the two electrodes were fixed along the plate edges and the plate was suspended in the test section by a set of thin wires. He noticed the plate deflection when the discharge took place even without air flow and he explained that as a result of the thrust force acting on the corona electrode because of the repelling action between this electrode and the traveling (positive) ions in the space between the two electrodes. He then examined the effect of the corona on the plate at different air flow of speeds not more than 2 m/sec. He concluded that the high voltage discharge does play an important role in drag reduction in the range of velocities used in his experimental investigation. In a related work to measure the drag reduction, Weinstein, et al. [26] introduced an electrostatically driven wall, capable

of producing moderately large amplitudes at short wavelengths and at large frequencies, which produces two dimensional wall motions and can be used as an active wall for drag reduction experiments. Medvedev, et al. [27] investigated the effect of solid surface coating with magnetic fluid layer which is held by outer magnetic field on the free-stream flow structure and on the hydrodynamic drag force. They concluded that this technique can be used for flow separation control for fluid flows of low velocities (order of 1 m/sec).

Many researches about corona discharge from electrical point of view have been reported in literature. Abdel-Salam [28] has shown experimentally that at high voltages the corona current decreases as the relative humidity increases and he explained that the lower currents were due to the lower mobility of the ions as a result of their combination with polar water molecules when the relative humidity increases. He also found that the corona inception takes place at low voltages on increasing the relative humidity. Abdel-Salam, et al. [29, 30] conducted theoretical and experimental investigations on the triggering mechanisms for initiating corona near highly stressed electrodes and the development of the pulse mode in the positive discharge from a single and twin interacting thin needles. They found that when the needles are brought close together, both the onset and offset of the transition from burst pulses to continuous glow increase as the needle-to-needle spacing decreases with a subsequent decrease of the corona current for the same applied voltage. Chapman [31] calculated the corona point discharge current by an approximate quantitative theory and verified his calculations experimentally. He proposed a geometric fraction parameter "F" which may be interpreted as the fraction of the space charge sphere around the point that participates in the corona discharge current. This parameter can be estimated from the spherical cone of revolution generated by an angle which is the average of the emission angle and the angle subtended at the point at which the trajectory leaves the space charge sphere.

He found that ($F = 0.5$) is a reasonable choice that fits the experimental measurements of the current for a wide range of point potential and wind speed.

The history of numerical methods for boundary-layer equations goes back to the 1930's and 1940's. Finite difference methods in a form very similar to those now in use began emerging in the 1950's. The difference schemes for the boundary-layer equations are relatively well-developed and tested as compared to methods for some other classes of flows. Except for a few isolated papers based on similarity methods, the calculation methods for boundary-layer-type problems that appear in the current literature can generally be categorized as (1) integral methods, (2) finite-difference methods, or (3) finite-element methods [32]. The problem of viscous, incompressible, laminar, two-dimensional fluid flow on a flat plate is a well-known and classic one [32,33,34].

1.4 Scope of the Present Study

This study evaluates numerically the corona discharge as a new technique of drag reduction and boundary layer control. Theoretical analysis and numerical method are used to determine the solutions of the equations which govern the process. A coupling between electrostatics and fluid mechanics must be considered to accomplish this study. The model simulates a glass flat plate of finite surface conductivity as a simple geometry. The positive (corona) electrode is the only source of positive ions in the computational domain. The emitted unipolar ions induce an ionic wind between the electrodes. In order to precisely describe the phenomena under investigation, the boundary conditions between the two electrodes must consider both the surface current and the gas phase current. The numerical method employed is the finite-difference method. The model first generates the appropriate grid, then solves the electrostatic equations and calculates the body force term in the region under investigation, and then solves the boundary layer equations. The model will continue

iterating between the electrostatic equations and the boundary layer equations until the final solution is obtained. It is anticipated that this study will determine quantitatively the drag reduction gained by applying the corona discharge and the range of the flow velocity for which it will be effective. It could also lead to other applications heretofore not considered based on an understanding of the surface-gas interaction.

2. DESCRIPTION OF THE PHYSICAL MECHANISMS

Ions in an electric field gain momentum and this momentum is transferred to neutral molecules through collisions. The coupling between the electric field, the ions, and the neutrals gives rise to the electric, corona, or ionic wind. Corona discharge applied inside the boundary layer will create an ionic wind which will add momentum to the fluid flow inside the boundary layer. This added momentum will help to overcome the viscous effect in such a way as to reduce the total drag on the body.

Corona discharge, known as a partial gas discharge, is a type of localized discharge resulting from transient gaseous ionization when the voltage stress exceeds a critical value. Cobine [35] defines corona in a more specific way as a glow discharge at atmospheric pressure that results from gas breakdown near a surface at a voltage less than the spark-breakdown voltage for a given gap length. Leob [13] describes corona as a general class of luminous phenomena associated with a current jump to micro amperes at the highly stressed electrode preceding a spark breakdown of the gap.

To obtain gas ionization, it is necessary to exceed, at least locally, the electrical breakdown strength of the gas. Corona is a local breakdown charge that fails to propagate itself and can occur only in a non-uniform electric field. The uniformity [13] of the electric field obtained depends on the ratio of the linear dimensions of the electrode to the gap length. As the electrode radius becomes considerably smaller than the gap length the field is highly distorted because the electric field has higher intensity near the electrode than far from it. The field becomes sufficiently high for breakdown at these regions long before a spark can propagate across the gas space. Breakdown proceeds in two steps; first, is the breakdown at the electrodes, one or both, and second is the breakdown of the gap as a whole, i.e., the spark. Sparking is an advanced stage of corona in which a complete breakdown of the gas occurs along a given path.

The breakdown at the electrodes is manifested by an emission of light and is sometimes accompanied by an audible noise and by current fluctuations. If the potential is raised at a point or a wire in the absence of external ionization, there is no appreciable current until the potential reaches a value defined as the starting potential of the corona. The value of this voltage is known as the corona onset voltage. At atmospheric pressures the luminosity at the negative point of the wire is localized at points of small area while at the positive point it sometimes spreads as a thin film over the high field portions of the conductor. This thin film of glow surrounding the positive electrode is known as the corona sheath.

2.1 Corona Polarity

Depending on the polarity of the point electrode, the charge carriers will carry the same polarity as the point electrode, i.e., for positive point electrode the charge carriers are positive ions and this is known as positive corona while for the negative point electrode the charge carriers are electrons in addition to negative ions and this is known as negative corona.

2.1.1 Positive corona

In this case the electric field is very strong near the positive point electrode and any electron generated in the gas between the two electrodes by photon, gamma or cosmic rays will move toward the positive electrode. During its travel the electron will ionize and excite many gas particles by collision and produce an electron avalanche descending upon the wire and positive ions drift first rapidly and later slowly to the negative electrode. Excited gas particles emit radiation which are capable of ionizing the gas photoelectrically. As the potential is raised a continuous avalanches will produce a self-sustaining corona.

2.1.2 Negative corona

In this case the electric field is very strong near the negative point electrode and any electron generated will travel toward the positive electrode. The space in which the electron is traveling has a weaker electric field than near the negative electrode which make these electrons useless for producing adequate ionization. Positive ions produced by collision will travel towards the negative electrode with lower velocity than the electrons because of its larger mass. Thus the chances for heavy space-charge accumulation are less than the case of positive corona. The value of the starting potential for negative corona is higher than that for starting positive corona [13]. The principal drawback to the use of negative corona is the generation of a significant amount of ozone [52].

2.2 Corona Setup

There are two possibilities for the shape of the electrodes which can assist to initiate and maintain corona current if the potential difference between the electrodes is raised to a value higher than the corona onset voltage.

In a point-to-plane setup, the polarity of the charge carriers is the same as the polarity of the point electrode. Positive corona can be obtained by raising the potential of the point electrode to a value higher than the corona onset voltage.

In the wire-to-wire setup, it is clear from the definition of both positive and negative corona that the positive corona will be dominant. It is possible to control the polarity of the charge carriers by the value of the potential difference maintained between the two electrodes. There are two possible cases which can lead to positive corona between the two electrodes. The first possibility can be achieved if both the positive electrode and the negative electrode are maintained at the same magnitude of electric potential but with opposite signs and the potential difference between the electrodes is adjusted to a value

higher than the value required to initiate positive corona and lower than that to initiate negative corona. The second possibility can be achieved if the positive electrode is maintained at a potential higher than the corona onset voltage and the other electrode is grounded. This makes the drift region dominant by positive ion which can be considered as of mobility sufficiently equal and constant.

2.3 Drag

The objective of applying corona discharge inside the boundary layer is to generate an ionic wind which will act in such a way as to reduce the total drag on the body. Drag force created by fluid flowing over a two dimensional solid surface is comprised of form or pressure drag and viscous drag. Pressure or form drag is caused by pressure difference created between upstream and downstream flow over the body due to its geometry. This drag can be reduced by streamlining the body shape. Viscous drag is caused by the shear stress distribution due to the skin friction which is function of fluid viscosity and the velocity gradient on the surface. Thus, the velocity profile inside the boundary layer has a significant impact on the value of the viscous drag.

2.4 Mechanism of Drag Reduction by Corona Discharge on a Flat Plate

When a free stream of fluid flow passes over a flat plate, both the fluid flow and flat plate will react on each other. As shown in Figure 2.1 the flow will drag the plate along its direction while the plate will resist the adjacent fluid particles and create what is called the boundary layer. The velocity of the fluid flow will vary from zero at the surface (no slip condition) to its free stream velocity value in a very thin layer. The variation in the velocity inside the boundary causes the fluid flow to lose some of its momentum which is called the

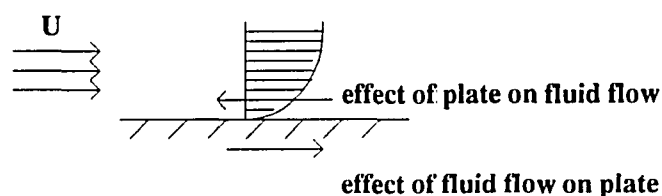


Figure 2.1: Mutual effect between the plate and the fluid flow

momentum deficit.

If a control volume is constructed over the surface of the plate including the boundary layer and a force and momentum analysis is carried out, it will show that the total momentum deficit in the flow inside the boundary layer along the whole plate will be equal the total drag force on the plate.

By applying different boundary layer control techniques, the momentum deficit inside the boundary layer can be reduced. It follows that the corresponding drag force acting on the plate will be reduced by the same amount.

Applying corona discharge inside the boundary layer is a recent technique that has been shown to reduce drag [25]. Depending on the order of polarity of the electrodes it is possible to direct the ionic wind inside the boundary layer along the fluid flow direction or against it.

The model assumed to analyze this effect inside the boundary layer is composed of two parallel wire electrodes immersed flush on the surface of a dielectric plate of finite

surface conductivity (glass). The electrodes are located at a position downstream of the leading edge of the flat plate as shown in Figure 2.2. The voltage difference between the two electrodes is assumed to be raised to a value to initiate and maintain positive corona. The resulting corona is a dc positive corona and the ions traveling from the corona (positive) electrode to the other (negative or grounded) electrode are positive ions. The applied electric field accelerates these ions which have a mass similar to the mass of the neutral molecules; therefore, when the positive ions and neutral molecules collide, momentum is transferred to the neutral gas molecules. After a collision, a positive ion is accelerated again by the electric field before colliding with another neutral molecule. Many such collisions occur before the ion reaches the other electrode and impart momentum to the neutral molecules creating what is known as the ionic wind. The ionic wind is created by energy transfer from ions and is not the movement of the ions themselves [36].

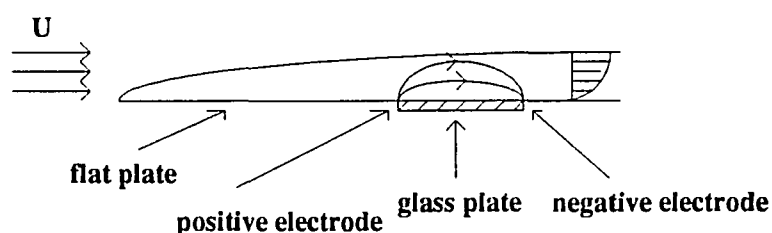


Figure 2.2: Model setup

Based on the above description, applying a corona discharge inside the boundary layer creates an ionic wind. If the ionic wind is traveling along the direction of the fluid flow the velocity deficit inside the boundary layer, and consequently the momentum deficit, will be both reduced. The momentum gained by the flow due to the corona discharge will equal the drag reduction on the body (flat plate). In other words the corona discharge causes a reaction on the electrodes as a force in the opposite direction to the drag force on the plate and the difference between this force and the original drag force (drag without corona effect) will equal the drag reduction on the plate. The electrode force is generated from the repelling action of the positive ions in the space between the two electrodes and the positive electrode and the attraction between these positive ions and the negative electrode. Figures 2.3 and 2.4 demonstrate this mechanism. In conclusion the corona discharge inside the boundary layer generates the ionic wind which will add a thrust force that reduces the total drag on the plate.

2.5 Surface Conductivity of Glass

The surface conductivity of glass is an important variable for this study. The Electrical conductivity of glass depends on its composition, temperature and the surrounding conditions. The surface resistivity is the resistance in ohms of a strip of surface of unit length and width [37]. Glass conductivity increases as the temperature of the glass. Surface conductivity is also a strong function of humidity. Based on the experimental work of Soetomo [25] glass with finite surface conductivity is considered as the flat plate in the present study. Using such kind of material for the plate is adequate to avoid electric shortening between the two electrodes. When applying the corona discharge along the surface of the glass plate, there will be a surface current that becomes an important boundary conditions for the model. Many investigators [38] ascribed the conductivity of glass to a

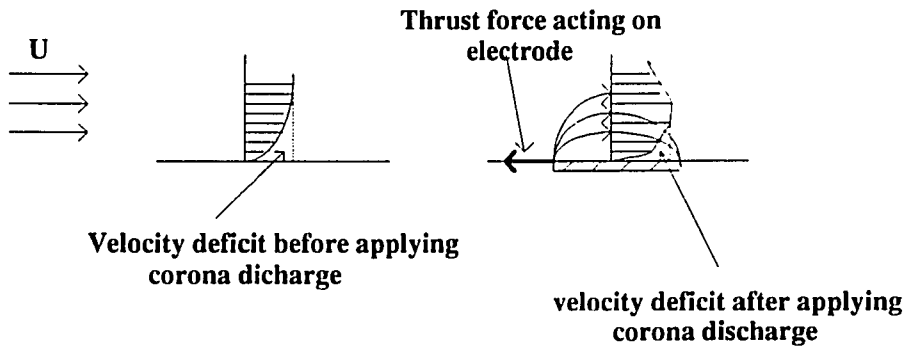


Figure 2.3: Corona discharge effect on velocity profile and resulting thrust force on the plate

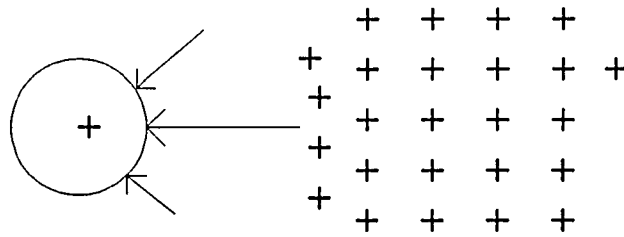


Figure 2.4: Force acting on the positive electrode due to repelling action of the positive ions

film of water condensed on its surface. Cleaning reduces the conductivity of better grades of glass but does not improve those of poorer grades. Surface resistivity of clean glass in dry air has a value typically of about 10^{14} ohm/square [38,39], and consequently a surface conductivity of 10^{-14} (ohm / square)⁻¹.

2.6 Modeling of the Present Study

The corona discharge inside the boundary layer on a flat plate creates an ionic wind which adds a body force resisting the viscous effect in such a way to reduce the total drag acting on that plate. This body force term will be calculated by solving the electrostatic equations governing the corona discharge. In order to precisely describe this body force term before it is used in the equations of motion, two study cases will be proposed to test the numerical simulation of the electrostatic equations. In both cases the leading edge of the flat plate constitutes the origin of the coordinate system used in the mathematical description of the problem.

2.6.1 Study case 1

Symmetry is the main feature of this case. Each of the two electrodes is maintained at the same value of the electric potential but with opposite sign. The two electrodes should be maintained at a potential difference just above the corona onset voltage to initiate positive corona only. The surface between the two electrodes is assumed to be of finite conductivity while it is assumed to be completely insulator outside the electrodes. Although this case is not of practical importance, its symmetry stems a good check for the simulation. This case will be considered only for the electrostatic evaluation of the corona discharge and will not be considered for the drag calculations.

2.6.2 Study case 2

This is the practical case. The two electrodes could be maintained at any potential difference above the corona onset voltage and less than the total breakdown potential of the gap between the two electrodes. The corona wire carries the net potential while the other electrode is grounded. The surrounding surface between and outside the two electrodes is assumed to be of finite conductivity.

3. MATHEMATICAL ANALYSIS

In order to evaluate the corona discharge as a new technique for boundary layer control and drag reduction, a simplified model is chosen to reduce the complexity of the analysis. The flow is assumed to be steady state, two-dimensional, incompressible, viscous flow over a flat plate of zero thickness at zero angle of attack. A body force term due to the corona discharge which models in the continuum framework the collisions of positive ions with the neutral molecules of the fluid is to be added to the equations of motion. A coupling between electrostatics and fluid mechanics must be considered. In the following sections a mathematical description of the key terms in this study will be introduced followed by the governing equations, the boundary conditions, and the initial conditions that will be used in the numerical solution.

3.1 Electric Conductivity and Electric Current

The corona current out of the positive electrode is divided into two currents; the gas phase electric current and the surface current.

We first consider the gas phase current between the two electrodes outside the corona sheath by using Ohm's law [40],

$$\vec{J} = \sigma_c \vec{E} \quad (3.1.1)$$

but

$$\vec{J} = nq\vec{v} \quad (3.1.2)$$

where \vec{v} is the velocity of ions due to conduction which is different from the convection velocity of the moving fluid flow.

By definition,

$$\bar{v} = k\bar{E} \quad (3.1.3)$$

and

$$\rho_c = nq \quad (3.1.4)$$

therefore,

$$\bar{J} = \rho_c k\bar{E} \quad (3.1.5)$$

where k is the ion mobility of the air.

Comparing equations (3.1.1) and (3.1.5) gives

$$\sigma_c = \rho_c k \quad (3.1.6)$$

Equation (3.1.6) shows that the electric conductivity of the medium will vary as the space charge varies with the assumption that the ion mobility is constant.

Combining equations (3.1.1) and (3.1.6) gives,

$$\bar{J} = \rho_c k\bar{E} \quad (3.1.7)$$

Equation (3.1.7) is valid for a stationary medium where the electric current is due to conduction only. If the medium is moving (as the flow inside the boundary layer) the convective speed of the flow will also contribute to the electric current. In this case the electric current density can be described as follows:

$$\bar{J} = nq\bar{v}_{cond} + nq\bar{v}_{conv} \quad (3.1.8)$$

or

$$\bar{J} = \rho_c (k\bar{E} + \bar{v}_{conv}) \quad (3.1.9)$$

Equation (3.1.9) represents the electric current density due to both conduction and convection.

The surface current is defined as

$$J_s = \sigma_{cs} E_x \quad (3.1.10)$$

where σ_{cs} is the surface conductivity of the plate and E_x is the electric field component along the plate surface between the two electrodes.

3.2 Space Charge Density

Using the differential form of Gauss' law for free space [40],

$$\nabla \cdot \vec{E} = \frac{\rho_c}{\epsilon_0} \quad (3.2.1)$$

Since \vec{E} is a conservative vector, it can be represented by the scalar electrical potential ϕ as :

$$\vec{E} = -\nabla \phi \quad (3.2.2)$$

\vec{E} and $\nabla \cdot \vec{E}$ can be written in two-dimensional as:

$$\vec{E} = E_x \vec{i} + E_y \vec{j} \quad (3.2.3)$$

$$\nabla \cdot \vec{E} = \frac{\partial E_i}{\partial x_i} \quad (3.2.4)$$

Combining equations (3.2.1), (3.2.2) and (3.2.4), the space charge density can be written as:

$$\rho_c = \epsilon_0 \frac{\partial E_i}{\partial x_i} \quad (3.2.5)$$

or

$$\rho_c = -\epsilon_0 \frac{\partial^2 \phi}{\partial x_i^2} \quad (3.2.6)$$

Equation (3.2.6) can be rewritten as:

$$\nabla^2 \phi = -\frac{\rho_c}{\epsilon_0} \quad (3.2.7)$$

which is Poisson's equation for electrostatics.

3.3 Body Force due to Corona Discharge

To obtain the body force acting on the fluid particles when applying corona discharge, the total electromagnetic force acting on charged particles under the effect of electric and magnetic fields should be considered [40]. This body force accelerates the charged particles which impact the gas molecules creating the ionic wind [36] which in turn can reduce the total drag on the body.

$$\vec{F} = nq(\vec{E} + \vec{v} \times \vec{B}) \quad (3.3.1)$$

which can be written as:

$$\vec{F} = \rho_c \vec{E} + \vec{J} \times \vec{B} \quad (3.3.2)$$

The first term on the right hand side of equation (3.3.2) is the force due to the electric field while the second term is the force due to the magnetic field. As shown in Figure 3.1

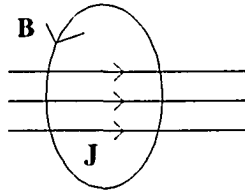


Figure 3.1: Magnetic field due to electric current

the electric current density vector \vec{J} which is along the electric field vector \vec{E} creates a magnetic field \vec{B} . This magnetic field acts along circles perpendicular to the direction of the electric current density \vec{J} .

The force due to the magnetic field is very small in comparison with the force due to the electric field (see appendix A) and consequently the force due to the magnetic field can be neglected. The effective body force is:

$$\vec{F} = \rho_c \vec{E} \quad (3.3.3)$$

Equation (3.3.3) represents the body force term to be added to the boundary layer equations.

3.4 Corona Onset Voltage

The critical value of the electric field strength, E_c , at which the corona onset begins at the positive (injection or corona) electrode depends on the geometry and the size of the electrode. E_c is based on the local breakdown of the air right around the electrode where the corona discharge starts to take place [35]. The voltage drop through the corona sheath is neglected in approximating the radius of the sheath by the wire radius [19]. The potential difference required to initiate corona current between the two electrodes is known as the corona onset voltage V_c . The value of this voltage depends on the size of the electrodes, the gap length, and the medium between the electrodes.

The corona discharge between wire-to-plane electrodes and between wire-to-wire electrodes have been covered extensively in the literature while the only data for a setup similar to the one under investigation is available in the experimental work of Soetomo [25]. Soetomo studied the effect of corona discharge on a flat plate made of glass with finite surface conductivity between two 28-mm-length-one-inch-separated wire electrodes in a low speed wind tunnel. Soetomo's measurements showed a corona current of few micro amperes at a potential difference between the two electrodes above 10.0 *kvolt* although according to his measurements the net drag force was improved at a lower potential difference. This may indicate that the sensitivity of his measurements does not detect lower currents. His results are mainly explaining the relation between the improvement in the drag and the voltage difference between the two electrodes and do not provide the details of the corona onset voltage and the voltage current relation. Based on that it is adequate to relate the data measured by Soetomo and the equations available in literature for the wire-to-wire corona discharge to describe the model under investigation. Peek's semi-empirical formula for corona onset between parallel wires [35,51, 52] is employed to calculate the value of E_c .

$$E_c = 30 m \delta \left(1 + \frac{0.301}{\sqrt{a \delta}}\right) \quad [kV / cm] \quad (3.4.1)$$

where a is the radius of the corona wire in centimeters, m is an irregularity factor which has the value 0.72 for standard wires [35,52], and δ is a factor related to the gas between the electrodes [35, 52]. For air

$$\delta = \frac{3.92 p}{273 + t} \quad (3.4.2)$$

where p is the air pressure in centimeters of mercury, and t is the temperature in degrees centigrade. At $25^\circ C$ and 76 cm Hg. $\delta \approx 1.0$.

The corona onset voltage between two wires can be determined by integrating the electric field from the surface of the corona wire to the other electrode. The value of this voltage depends on the corona electrode diameter and the gap length between the two electrodes. Equation that calculates the value of this voltage between parallel wires is available in literature [35,51, 52].

$$V_c = E_c a \ln\left(\frac{S}{a}\right) \quad [kV] \quad (3.4.3)$$

where S is the distance between the two electrodes.

3.5 Corona Current

Relations describing the corona current for the point-to-plane-electrodes are available in literature [35, 51, 52, 53, 54]. Seaver [54] derived an equation based on a force balance for a steady state corona current in air between wire-to-wire electrodes at a potential difference higher than the corona onset voltage. This equation is written below

$$I_c = \frac{1}{a_o R} [e^{a_o(V - V_o - V_L)} - 1] \quad [Amp] \quad (3.5.1)$$

where V is the voltage at the corona wire, V_L is the voltage at the other electrode, V_o is the corona onset voltage. Since

$$\Delta\phi = V - V_L \quad (3.5.2)$$

and also we can introduce

$$b = a_o R \quad (3.5.3)$$

equation (3.5.1) can be written as :

$$I_c = \frac{1}{b} [e^{a_o(\Delta\phi - V_o)} - 1] \quad [mA] \quad (3.5.4)$$

In that equation R is a constant representing the resistance outside the corona wire with the unit $[M\Omega]$ and a_o is a constant with the unit $[kV]^{-1}$. In his derivation, Seaver defined a_o as follows [53, 54]

$$a_o = \frac{\chi_i q}{k T} \quad (3.5.5)$$

where q is the ion charge, k is the Boltzmann constant, T is the absolute temperature of the medium, and χ_i is a ratio known as the ion-to-neutral excess momentum concentration factor and is defined as

$$\chi_i = \frac{n_i}{n} \quad (3.5.6)$$

where n_i is the ion density at any point and n is that fraction of the neutral density at the same point which has excess momentum due to collisions with the ions. Although n_i and n can vary along the path of the ions their ratio is constant because n_i is responsible for creating the concentration n at that path. It is assumed that both n_i and n are small compared to the total neutral molecules density at the point [25]. The numerical values of R and a_0 in Seaver's equation vary depending on the setup under investigation. Seaver collected data on a two wire corotron (corona charger) and fit these data to his equation which lead to the numerical values of a_0 and R for that setup. These values are introduced here as an example.

$$a_0 = 0.43 \pm 0.02 \quad [kV]^{-1} \quad (3.5.7)$$

and

$$R = 3.4 \quad [M\Omega] \quad (3.5.8)$$

which gives,

$$b = 1.462 \quad [mA]^{-1} \quad (3.5.9)$$

Following a similar approach, we will fit Soetomo's data into Seaver's equation and determine the numerical values of a_0 and b for the model under investigation. The least-squares curve fitting technique will be employed for that purpose. Based on the details of appendix B the optimum values of a_0 and b which makes the best fit of Soetomo's data into Seaver's equation are found to be

$$a_0 = 0.365 \quad [kV]^{-1} \quad (3.5.10)$$

and

$$b = 7615.0 \quad [mA]^{-1} \quad (3.5.11)$$

which gives

$$R = 2.086 \quad [M\Omega] \quad (3.5.12)$$

A graphical representation of Soetomo's measured data and Seaver's equation will be shown in chapter 5 where the results of this study will be discussed.

In conclusion, the predicted corona current for the model under investigation can be obtained for the Soetomo's electrode length according to the following equation:

$$I_c = 1.31319 * 10^{-4} [e^{0.365(\Delta\phi - 0.68027)} - 1] \quad [mA / 28 mm] \quad (3.5.13)$$

and this equation can be changed to the following form:

$$I_c = 4.68999 * 10^{-6} [e^{0.365(\Delta\phi - 0.68027)} - 1] \quad [A / m] \quad (3.5.14)$$

where $\Delta\phi$ is the potential difference between the two electrodes in kilovolts.

3.6 Governing Equations

3.6.1 Boundary layer equations

Boundary layer equations are one of the limiting cases of the Navier-Stokes equations when the Reynolds number is large. The model under investigation is governed by the boundary layer equations for two-dimensional, incompressible fluid flow on a flat plate of zero thickness and zero angle of attack.

Outside the boundary layer the inertia force will be dominant and the friction force is very small and can be neglected, while inside the boundary layer both inertia and friction forces are of comparable order of magnitude.

The simplified form of the mass continuity equation and the Navier-Stokes equations for incompressible flow [41] can be written as:

$$\nabla \cdot \bar{u} = 0 \quad (3.6.1.1)$$

$$\rho \frac{d\bar{u}}{dt} = \bar{F} - \nabla p + \mu \nabla^2 \bar{u} \quad (3.6.1.2)$$

For steady state conditions, two-dimensional, incompressible, viscous fluid flow, and using equation (3.3.3) for the body force, equations (3.6.1.1) and (3.6.1.2) can be written as:

$$\frac{\partial u}{\partial x} + \frac{\partial v}{\partial y} = 0 \quad (3.6.1.3)$$

$$u \frac{\partial u}{\partial x} + v \frac{\partial u}{\partial y} = \frac{\rho_c}{\rho} E_x - \frac{1}{\rho} \frac{\partial p}{\partial x} + \nu \left(\frac{\partial^2 u}{\partial x^2} + \frac{\partial^2 u}{\partial y^2} \right) \quad (3.6.1.4)$$

$$u \frac{\partial v}{\partial x} + v \frac{\partial v}{\partial y} = \frac{\rho_c}{\rho} E_y - \frac{1}{\rho} \frac{\partial p}{\partial y} + \nu \left(\frac{\partial^2 v}{\partial x^2} + \frac{\partial^2 v}{\partial y^2} \right) \quad (3.6.1.5)$$

The Navier-Stokes equations are not easy to solve because of the non-linearity of the convection terms (or inertia). For some flows when these terms can be dropped in a natural way, an exact solution can be obtained. An approximate solution for the Navier-Stokes equations can be obtained by dropping small terms in the equations itself.

Two limiting cases of large and small viscosity are of particular importance. In very slow fluid flow (creeping motion) viscous forces are large compared with inertia forces while in boundary layer fluid flow viscous forces are small compared to inertia forces. In creeping motion inertia forces can be dropped in comparison with viscous forces while in the boundary layer it is not possible to drop the viscous term because the physical condition of no slip at the solid boundary cannot be met [42].

With small viscosity or large Reynolds number, the fluid flow region can be divided into two parts:

1- Inside the boundary layer, which is a thin layer where the fluid flow velocity varies between zero and the free stream value, a large velocity gradient exists which makes $\tau = \mu \frac{\partial u}{\partial y}$ a significant value although the value of μ is small.

2- Outside the boundary layer, in the potential flow region, the value of $\frac{\partial u}{\partial y}$ is also small. Since $\tau = \mu \frac{\partial u}{\partial y}$ is a product of two small quantities, its value is very small and can be neglected.

To simplify the governing equations for the flow inside the boundary layer with corona discharge, an order of magnitude analysis will be followed (see appendix C). Equations (C.14) and (C.15) are the resulting boundary layer equations describing the model under investigation which will be rewritten here as:

$$\frac{\partial u}{\partial x} + \frac{\partial v}{\partial y} = 0 \quad (3.6.1.6)$$

$$u \frac{\partial u}{\partial x} + v \frac{\partial u}{\partial y} = \frac{\rho_c}{\rho} E_x + \nu \frac{\partial^2 u}{\partial y^2} \quad (3.6.1.7)$$

This system of equations describe the fluid flow inside the boundary layer with corona discharge except very close to the leading edge of the flat plate and very close to the location of the positive electrode . Downstream of the leading edge the equations are valid at a Reynolds number value of at least 1000 [3,43] based on the distance measured from the leading edge. Away from the electrodes by about 4% of the gap length between the electrodes the equations are valid as will be shown in chapter 5.

3.6.2 Electrostatic equations

Using the charge conservation equation [40],

$$\nabla \cdot \vec{J} = - \frac{\partial \rho_c}{\partial t} \quad (3.6.2.1)$$

For steady state conditions this equation becomes

$$\nabla \cdot \vec{J} = 0 \quad (3.6.2.2)$$

which can also be written in two-dimensional as:

$$\frac{\partial J_x}{\partial x} + \frac{\partial J_y}{\partial y} = 0 \quad (3.6.2.3)$$

Using equation (3.2.2), equation (3.1.9) can be written as:

$$\begin{aligned} J_x &= \rho_c \left(u - k \frac{\partial \phi}{\partial x} \right) \\ J_y &= \rho_c \left(v - k \frac{\partial \phi}{\partial y} \right) \end{aligned} \quad (3.6.2.4)$$

Differentiating both equations of (3.6.2.4) with respect to x and y respectively and substituting back, equation (3.6.2.3) can be written as:

$$\rho_c \left(\frac{\partial u}{\partial x} + \frac{\partial v}{\partial y} \right) + u \frac{\partial \rho_c}{\partial x} + v \frac{\partial \rho_c}{\partial y} - k \rho_c \left(\frac{\partial^2 \phi}{\partial x^2} + \frac{\partial^2 \phi}{\partial y^2} \right) - k \left(\frac{\partial \rho_c}{\partial x} \frac{\partial \phi}{\partial x} + \frac{\partial \rho_c}{\partial y} \frac{\partial \phi}{\partial y} \right) = 0 \quad (3.6.2.5)$$

Using equations (3.2.7) and (3.6.1.6) and rearranging, equation (3.6.2.5) can be written as:

$$u \frac{\partial \rho_c}{\partial x} + v \frac{\partial \rho_c}{\partial y} + k \left[\frac{\rho_c^2}{\epsilon_0} - \frac{\partial \rho_c}{\partial x} \frac{\partial \phi}{\partial x} - \frac{\partial \rho_c}{\partial y} \frac{\partial \phi}{\partial y} \right] = 0 \quad (3.6.2.6)$$

The first two terms of equation (3.6.2.6) represent the convection part of the electric current density while the third term represents the conduction part.

The voltage drop through the corona sheath is neglected in approximating the radius of the sheath by the wire radius [19]. Based on the above analysis, equations (3.2.7) and (3.6.2.6) are the resulting electrostatic equations describing the corona discharge in the gas phase for the model under investigation which will be rewritten here as:

$$\frac{\partial^2 \phi}{\partial x^2} + \frac{\partial^2 \phi}{\partial y^2} = -\frac{\rho_c}{\epsilon_0} \quad (3.6.2.7)$$

$$u \frac{\partial \rho_c}{\partial x} + v \frac{\partial \rho_c}{\partial y} + k \left[\frac{\rho_c^2}{\epsilon_0} - \frac{\partial \rho_c}{\partial x} \frac{\partial \phi}{\partial x} - \frac{\partial \rho_c}{\partial y} \frac{\partial \phi}{\partial y} \right] = 0 \quad (3.6.2.8)$$

3.7 Boundary Conditions

Considering the following coordinate system:

- The origin is at the leading edge of the flat plate.
- The x-axis is along the plate.
- The y-axis is perpendicular to the plate at the origin.

3.7.1 Fluid flow velocity

The absence of slip between the fluid and the wall surface and the recovery of the outer-flow velocity far from the wall surface are the boundary conditions which accompany the boundary-layer equations. That is, the following boundary conditions must be satisfied [3,41,42,43]:

$$\text{For } y = 0 \quad u = v = 0 \quad (3.7.1.1)$$

$$\text{For } y \rightarrow \infty \quad u \rightarrow U \quad (3.7.1.2)$$

3.7.2 Electric potential and charge density

For modeling, the wire-electrodes are assumed to be immersed, flush with the flat plate and perpendicular to the direction of the fluid flow. The positive electrode is taken to be at a location downstream from the leading edge of the plate (see Figure 2.2). When a potential difference is applied between the electrodes at a value allowing for the initiation of positive corona, only a flow of positive ions will be emitted from the positive electrode.

In this case, the two different media at the interface must be considered to determine the proper boundary conditions necessary to solve numerically the mathematical model. Air (or free space) and a dielectric material (glass) comprise the two media. The interface is taken to be the water monolayer on the glass surface between these two bulk media. As the

voltage difference applied between the two electrodes is set to a value less than the dielectric strength of both glass [44] and air to start the positive corona, an electric field will be created. As a result of this electric field the dielectric material will become polarized. The total bulk polarization charge density will be zero as the dielectric material is neutral by definition. The surface polarization charge is not zero for a finite normal component of electric field; however this charge is stationary and will not contribute to the surface current and a charge of opposite sign will be accumulated on the internal side of the dielectric surface. At the same time, in the free space, the traveling positive ions create an electric current between the two electrodes. It is possible that some of the traveling positive ions can be deposited to the glass surface and contribute to the surface current at the interface. Since the tangential components of the electric field at the interface will be the same for the two bulk media and the water monolayer on the glass surface and since the electric conductivity of the glass surface and the air are different, it can be concluded that the tangential component of the gas phase electric current density and the surface current density for the model under investigation have a discontinuity at the interface. Based on this description, the electrostatic boundary conditions for the two dependent variables (ϕ and ρ_c) will be described in details in the following sections.

3.7.2.1 Interface electric potential without ion deposition to the surface

The current density at the interface (water monolayer on the glass surface) can be evaluated utilizing the setup shown in Figure 3.2.

The surface current along a plate of length L and width W at a potential difference $\Delta\phi$ along its length as shown in Figure 3.2 where L is along the x -axis is given by:

$$I = \frac{\Delta\phi}{R} \quad (3.7.2.1.1)$$

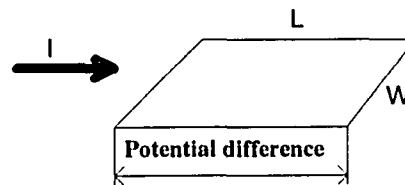


Figure 3.2: Surface current along the surface of a dielectric plate

where R is the total resistance of the plate which can be obtained as:

$$R = R' \frac{L}{W} \quad (3.7.2.1.2)$$

For a square strip of ($L = W$), this resistance is described as the surface resistivity and its unit is known in the literature as Ohms/square [37,39]. The surface resistivity is a property of the material which can be obtained from tables.

Combining equations (3.7.2.1.1) and (3.7.2.1.2) gives,

$$I = \frac{\Delta\phi W}{R' L} \quad (3.7.2.1.3)$$

The surface current density per unit width can be obtained as:

$$\bar{J}_s = \frac{I}{W} \bar{i} \quad (3.7.2.1.4)$$

or

$$\bar{J}_s = \frac{\Delta\phi}{R'L} \bar{i} \quad (3.7.2.1.5)$$

Equation (3.7.2.1.5) represents the surface current density at the interface (glass surface) which can also be rewritten as:

$$\bar{J}_s = \sigma_{cs} E_x \bar{i} \quad (3.7.2.1.6)$$

where σ_{cs} is the surface conductivity of the glass.

The resistivity and conductivity of the glass surface have constant values for constant surrounding conditions (temperature, humidity,...). Using this fact and equations (3.7.2.1.5) and (3.7.2.1.6), the tangential component of the electric field between the two electrodes at the interface can be considered as constant and has the value,

$$E_x = \frac{\Delta\phi}{L} \quad (3.7.2.1.7)$$

This value will be the same for the two bulk media at the interface. Using equation (3.2.2), this tangential component of the electric field can be described as:

$$E_x = -\frac{d\phi}{dx}$$

therefore,

$$\frac{d\phi}{dx} = -\frac{\Delta\phi}{L}$$

Integrating between the two electrodes gives,

$$\phi = \phi_u + \frac{\phi_d - \phi_u}{L} (x - x_0) \quad (3.7.2.1.8)$$

where:

- ϕ_u the electric potential of the upstream electrode
- ϕ_d the electric potential of the downstream electrode
- x the distance measured from the leading edge of the flat plate
- x_0 the location of the upstream electrode measured from the leading edge

The value of the electric potential is the same for the two bulk media at the interface.

3.7.2.2 Interface electric potential with ion deposition to the surface

This is the more general case to evaluate the boundary conditions for the electric potential ϕ and the charge density ρ_c at the interface between the two bulk media in the region between the two electrodes. The analysis described in the previous section can be obtained here as a special case. Consider an imaginary control volume over a strip of glass surface of length Δx and width W and of infinitesimal height. The corona discharge generates a cloud of traveling positive ions over this strip. Some of these ions can be deposited to the surface and contribute to the surface current at the interface as shown in Figure 3.3.

The current density conservation over the control volume can be described as:

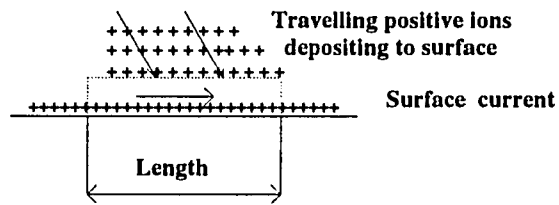


Figure 3.3: Surface current with ion-deposition contribution

$$\left[J_s|_{x+\Delta x} - J_s|_x \right] W = \bar{J}_c \cdot \bar{n} W \Delta x \quad (3.7.2.2.1)$$

or

$$\frac{\partial J_s}{\partial x} = \bar{J}_c \cdot \bar{n} \quad (3.7.2.2.2)$$

where \bar{n} is normal unit vector to the plate surface and

$$\begin{aligned} \bar{J}_s &= \sigma_{cs} \bar{E}_s \\ \bar{J}_c &= \sigma_c \bar{E}_c \end{aligned} \quad (3.7.2.2.3)$$

Using equations (3.2.2) and (3.7.2.2.3) in equation (3.7.2.2.2) and considering σ_s as constant gives

$$\sigma_{cs} \frac{\partial^2 \phi}{\partial x^2} = -\sigma_c \frac{\partial \phi}{\partial y} \quad (3.7.2.2.4)$$

Equation (3.7.2.2.4) represents the general boundary equation for the electric potential at the interface in the region between the two electrodes for both the water monolayer on the glass surface (where the surface current is running) and the gas phase side (where the gas phase current is running). If the y-component of the electric field at the interface is zero the solution of this equation is the same as equation (3.7.2.1.8). If the y-component of the electric field is finite at the interface equation (3.7.2.2.4) will be solved simultaneously with equation (3.6.2.7) using the prescribed electrical potential at the electrodes.

3.7.2.3 Charge density at the positive electrode

The electrodes are assumed to be two long, thin, wires of the same diameter, immersed flush with the surface of the flat plate. The potential difference between the two electrodes is set to a value to initiate positive corona which means that the positive electrode is the only source of positive ions in the domain. The corona sheath around the positive electrode is very thin in thickness and very unstable in nature which makes the analytic calculations of the charge density at this electrode is not easy to be accurately obtained. Instead an approximate value can be calculated and used to start the numerical solution and then an iterative procedure for the current conservation around this electrode reveals the appropriate value of the charge density which will satisfy the corona current in the domain. The approximate value of the charge density at the positive electrode can be calculated as follows:

The emitting surface area of the electrode is:

$$A = \pi d l F \quad (3.7.2.3.1)$$

where d is the electrode diameter, l is its length, and F is a geometric parameter. F is taken as 0.5 since most of the positive ions emitting from the positive electrode are attracted towards the negative electrode [31].

The electric current due to corona discharge at the positive electrode :

$$I = \bar{J}_{c_o} \cdot \bar{A} \quad (3.7.2.3.2)$$

The charge density at the positive electrode is:

$$\rho_{c_o} = \frac{J_{c_o}}{v} \quad (3.7.2.3.3)$$

where v is the drift velocity of the ions at the positive electrode which is defined as:

$$v = k E_c \quad (3.7.2.3.4)$$

where E_c is the electric field strength of the corona onset at the positive (injection) electrode and k is the ion mobility of the air. Using the ion mobility of the air inside the corona sheath is used here as an approximation.

Combining equations (3.7.2.3.2), (3.7.2.3.3), and (3.7.2.3.4) the approximate value of the charge density at the positive electrode can be obtained as :

$$\rho_{c_o} = \frac{I}{\pi d F k E_c} \quad [C / m^3] \quad (3.7.2.3.5)$$

The approximate value of the charge density at the positive electrode will be used to start the numerical solution and it will be modified through an iterative procedure until a value satisfying the corona current in the domain is reached. In order to accomplish the iterative procedure a control volume around this electrode will be considered. The positive electrode represents a source inside the control volume and the current passing across its boundary is due to this source. This current can be calculated as follows:

$$I = \int \vec{J} \cdot d\vec{A} \quad (3.7.2.3.7)$$

where

$$\vec{J} = \rho_c k \vec{E} \quad (3.7.2.3.8)$$

3.7.2.4 Charge density at the interface between the two electrodes

The positive electrode is the only source of positive ions in the domain. All positive ions generated at the positive electrode will travel either as surface current or in the space above the surface between the two electrodes as corona current. The ions arrived at the negative electrode will be neutralized by electrons and continue traveling as neutral particles with the fluid flow.

The charge density at the positive electrode is prescribed in the previous section. The charge density at the rest of the interface (gas phase side) between the two electrodes will be obtained numerically by the simultaneous solution of equation (3.6.2.8) on the surface (gaseous phase side) and in the domain. Outside the range between the two electrodes, at the interface, the charge density is zero.

An analytic solution for the charge density distribution at the interface (gas phase side) between the two electrodes can be obtained in the case of no ion deposition to the surface (see Appendix D). Equation (D.21) represents this analytic solution at the interface (gas phase side) between the two electrodes which can be rewritten here as:

$$\rho_c = \frac{\rho_{c^0}}{1 + \frac{L\rho_{c^0}(x - x_0)}{\epsilon_0 \Delta\phi}} \quad (3.7.2.4.1)$$

Examining both the numerical and the analytic solutions at the interface (gas phase side) between the two electrodes shows good agreement as it will be presented in chapter 5.

In conclusion, equations (3.7.2.2.4) and (3.6.2.8) represent the general boundary conditions of the electric potential and the charge density at the interface (gas phase side) in the region between the two electrodes.

3.7.2.5 Electric potential outside the two electrodes

The material of the flat plate is taken to be the same as that between the two electrodes, which is a glass of finite surface conductivity. The electric potential at the interface ahead of the upstream electrode will be constant and has the same value as that of the upstream electrode, while the electric potential beyond the downstream electrode will be also constant and at the same value as that electrode. Upstream of the leading edge along the extension of the plate the electric potential is described by Laplace equation. Since there is insufficient boundary conditions to solve this equation at this region of the boundary a conformal mapping transformation has been employed to describe this electric potential (see Appendix E for details). Equation (E.17) represents the electric potential distribution

upstream of the leading edge along plane of the flat plate in the negative direction of the x -axis. This equation can be written here as:

$$\phi = \phi_u \left[1 - \left(\frac{-x}{h} \right)^{1/2} \right] \quad (3.7.3.1)$$

where h represents a characteristic length chosen as the height of the computational domain. Upstream of this characteristic length the electric potential is zero.

The computational domain will be chosen large enough so that the electrical potential at the other three sides of the domain vanish. The numerical scheme will determine the appropriate size of the computational domain when solving Poisson's equation.

3.8 Initial Conditions

3.8.1 Fluid flow velocity

The vertical section above the leading edge of the flat plate is considered as the first station of the marching process to calculate the boundary layer profile. At this station the two components of the velocity vector are

$$u = U \quad (3.8.1.1)$$

$$v = 0 \quad (3.8.1.2)$$

The contradiction in describing the x -component of the velocity u between the boundary and initial conditions at the leading edge as described in sections 3.7.1 and 3.8.1 has no serious effect on the numerical solution.

3.8.2 Electric potential and charge density

The calculations of the electric potential can be obtained by solving Poisson's equation simultaneously on all the grid points of the computational domain. In order to obtain a unique solution the boundary conditions should be prescribed.

The positive electrode is the only source of positive ions in the model under investigation and all the positive ions emitted at this electrode will be attracted towards the negative electrode [31]. All the positive ions arrived at the negative electrode will be neutralized by electrons and travel with the neutral particles of the fluid flow. Therefore, only positive ions exist between the two electrodes and consequently the ionic wind which resists the viscous effect also exist mainly between the two electrodes.

Based on this description the calculation of the charge density will be started at a vertical section above the positive electrode and march downstream when the positive electrode is upstream of the negative electrode or march upstream when the positive electrode is downstream the negative electrode. For either marching directions the charge density at the previous section before the positive electrode location will be considered as the initial condition and has the value zero, or

$$\rho_c(i, j \pm 1) = 0$$

where:

- + for upstream marching direction
- for downstream marching direction

3.9 Drag Calculations

Predicting drag is an important objective for this study to evaluate the corona discharge as a means of overcoming the viscous effect and consequently reduce the total drag on the model under investigation. The flat plate and the fluid flow exert reactive forces on

each other. The plate causes a loss in the momentum of the fluid flow while the fluid flow causes a shear force on the plate. The local shear stress at any point on the flat plate is :

$$\tau_w = \mu \left. \frac{\partial u}{\partial y} \right|_{y=0} \quad (3.9.1)$$

where μ is the dynamic viscosity of the air. The total drag on the plate can be obtained by integrating this equation over the total wetted area of the plate.

$$D = b \int_{plate} \tau_w dx \quad (3.9.2)$$

where b is the width of the plate. We will refer during our analysis to this drag force as the shear drag force.

This drag force which is the resultant of the viscous effect and the electrostatic force equals the total loss in the momentum of the fluid flow over the plate according to the momentum balance (see Appendix F). The ionic wind created by the corona discharge reduces the momentum deficit of the flow and consequently reduces the net drag on the plate. Equation (F.5) represents this net drag which will be written below as:

$$D = \rho U^2 b h - \rho b \int_0^h u^2 dy \quad (3.9.3)$$

where h is the height of the computational domain, U is the free stream velocity, and u is the local velocity at the location of the integration. We will refer during our analysis to this drag force as the momentum drag force. Calculating the momentum drag force acting on the flat plate portion included between the two electrodes with and without the corona effect

provides the drag reduction due to the corona over this portion of the plate. Introducing this definition for the percentage drag reduction due to the corona effect helps us in the quantitative analysis under investigation.

$$DR\% = \left(\frac{Drag_{without\ corona} - Drag_{with\ corona}}{Drag_{without\ corona}} \right) 100 \quad (3.9.4)$$

Considering the computational domain height as the upper limit of the integration in equation (3.9.3) removes the numerical inaccuracy in calculating the boundary layer thickness and consequently reducing the corresponding error in the drag calculations. The boundary layer thickness is determined as the vertical height measured from the flat plate thickness where the local velocity equals 99% of the free stream velocity. The error in determining precise boundary layer thickness is interrelated to the step size of the mesh dividing the boundary layer thickness. A graphical representation will explain that in chapter 5 where the results of this study are discussed.

The local skin friction coefficient C_f and the drag coefficient C_D are another two non dimensional parameters that can be used to demonstrate the effect of the corona discharge on the drag.

$$C_f = \frac{\tau_w}{\frac{1}{2}\rho U^2} \quad (3.9.5)$$

$$C_D = \frac{D}{\frac{1}{2}\rho U^2 A} \quad (3.9.6)$$

where A is the total wetted area of the flat plate.

The exact solution of the boundary layer equations on a flat plate developed by Blasius provides an exact expression for the boundary layer thickness, the local skin friction coefficient, and the drag coefficient. These expressions are listed below and will be used as a check for the accuracy of the numerical solution.

$$\delta|_{Blasius} = \frac{5.0 x}{\sqrt{Re_x}} \quad (3.9.7)$$

$$C_f|_{Blasius} = \frac{0.664}{\sqrt{Re_x}} \quad (3.9.8)$$

$$C_D|_{Blasius} = \frac{1.328}{\sqrt{Re_L}} \quad (3.9.9)$$

where x is the length measured from the leading edge of the flat plate, Re_x is the local Reynolds number based on that length, and Re_L is the Reynolds number based on the length of the wetted area of the plate. In our analysis for the drag reduction due to the corona discharge Re_L will be based on the gap length between the two electrodes.

$$\begin{aligned} Re_x &= \frac{\rho U x}{\mu} \\ Re_L &= \frac{\rho U L}{\mu} \end{aligned} \quad (3.9.10)$$

where L is the gap length between the two electrodes.

4. NUMERICAL ANALYSIS

The objective now is to solve numerically the mathematical model describing the effect of corona discharge on boundary layer flow over a flat plate. Since the problem is analyzed on a simple geometry and the variables under investigation do not change rapidly, a finite difference approach can be followed [45]. Based on the mathematical analysis of the previous section, the model under investigation is governed by two systems of partial differential equations; the electrostatic equations and the boundary layer equations. The solution of the boundary layer equations provides the velocity distribution while the solution of the electrostatic equations provides the body force distribution due to the corona effect. The two systems are coupled and their solution must be obtained simultaneously. In the finite-difference approach, the problem domain is discretized so that the dependent variables are considered to exist only at discrete points. Derivatives are approximated by differences resulting in an algebraic representation of the partial differential equations. The nature of the resulting system of algebraic equations depends on the character of the problem posed by the original system of partial differential equations [32, 46, 47].

In order to achieve the numerical solution, these steps will be followed:

- 1- Classify mathematically the governing equations to distinguish the features of the solution in order to choose the proper numerical schemes to be followed.
- 2- Determine the appropriate computational domain.
- 3- Discretize the computational domain with a suitable grid.
- 4- Finite difference the governing partial differential equations on the chosen grid.
- 4- Prepare the prescribed initial and boundary conditions to be able to start the numerical solution.
- 5- Construct the computational plan to carry out the entire numerical solution.
- 6- Write the FORTRAN code.

4.1 Mathematical Classification of Governing Equations

4.1.1 Boundary layer equations

The fluid flow inside the boundary layer is governed by equations (3.6.1.6) and (3.6.1.7), which are repeated below:

$$\frac{\partial u}{\partial x} + \frac{\partial v}{\partial y} = 0 \quad (3.6.1.6)$$

$$u \frac{\partial u}{\partial x} + v \frac{\partial u}{\partial y} = -\frac{\rho_c}{\rho} \frac{\partial \phi}{\partial x} + \nu \frac{\partial^2 u}{\partial y^2} \quad (3.6.1.7)$$

which can be written in a matrix form as:

$$\begin{bmatrix} 1 & 0 \\ u & 0 \end{bmatrix} \begin{Bmatrix} u_x \\ v_x \end{Bmatrix} + \begin{bmatrix} 0 & 1 \\ v & 0 \end{bmatrix} \begin{Bmatrix} u_y \\ v_y \end{Bmatrix} + \begin{bmatrix} 0 & 0 \\ -v & 0 \end{bmatrix} \begin{Bmatrix} u_{yy} \\ v_{yy} \end{Bmatrix} = \begin{bmatrix} 0 & 0 \\ -\frac{\rho_c}{\rho} & 0 \end{bmatrix} \begin{Bmatrix} \phi_x \\ \phi_y \end{Bmatrix} \quad (4.1.1.1)$$

Introducing the vectors,

$$\vec{w} = \begin{Bmatrix} u \\ v \end{Bmatrix}$$

and

$$\vec{e} = \begin{Bmatrix} \phi_x \\ \phi_y \end{Bmatrix}$$

this system can be written as:

$$[A]\vec{w}_x + [B]\vec{w}_y + [C]\vec{w}_{yy} = [D]\vec{e} \quad (4.1.1.2)$$

The eigenvalues of the coefficient matrix of the highest order term determines the mathematical classification of this system [32, 46].

$$\begin{vmatrix} -\lambda & 0 \\ v & -\lambda \end{vmatrix} = 0 \quad (4.1.1.3)$$

which gives,

$$\lambda^2 = 0 \quad (4.1.1.4)$$

or

$$\lambda = 0 \quad (4.1.1.4)$$

Since both eigenvalues are zeros, this system is parabolic and a marching procedure in the downstream direction of the fluid flow motion can be followed.

4.1.2 Electrostatic equations

The corona discharge is governed by equations (3.6.2.7) and (3.6.2.8), which are repeated below:

$$\frac{\partial^2 \phi}{\partial x^2} + \frac{\partial^2 \phi}{\partial y^2} = -\frac{\rho_c}{\epsilon_0} \quad (3.6.2.7)$$

$$u \frac{\partial \rho_c}{\partial x} + v \frac{\partial \rho_c}{\partial y} + k \left[\frac{\rho_c^2}{\epsilon_0} - \frac{\partial \rho_c}{\partial x} \frac{\partial \phi}{\partial x} - \frac{\partial \rho_c}{\partial y} \frac{\partial \phi}{\partial y} \right] = 0 \quad (3.6.2.8)$$

In addition to the above two equations, equation (3.7.2.2.4) describes the electric potential boundary conditions on the surface between the two electrodes.

$$\sigma_s \frac{\partial^2 \phi}{\partial x^2} = -\rho_c k \frac{\partial \phi}{\partial y} \quad (3.5.2.2.4)$$

This system is mixed in classification, exhibiting behavior of more than one type. Equation (3.6.2.7) is elliptic which requires a simultaneous solution over all grid points of the computational domain and the five-point scheme can be used to obtain this solution while equation (3.6.2.8) can be hyperbolic or parabolic depending on the coefficients of all terms of the equation and a marching procedure can be followed in the direction of the traveling positive ions. Equation (3.7.2.2.4) is parabolic and a marching process can be followed on the surface simultaneously with the marching process of equation (3.6.2.8).

4.2 Appropriate Computational Domain

In order to obtain a unique solution for the elliptic equation (3.6.2.7), the numerical solution should be accomplished on a closed domain with prescribed boundary conditions on all boundaries. A rectangular domain is chosen for this purpose and the flat plate represents all or a part of the bottom side of this domain. The boundary conditions of the electric potential are prescribed only on the lower side of the computational domain (the flat plate side) while it is difficult to describe these values on the other three sides for a pre-determined computational domain. To resolve this problem the computational scheme will start with any rectangular domain with the flat plate as a bottom side with its electric potential prescribed on all grid points and consider the other three sides with its electric potential prescribed on all grid points as zero values. After the electrostatic computations converge to the numerical solution a check on all the values of the electric potential on all grid points at one step inside these three sides will be done to make sure that these values are small enough compared to the zero value assumed on the grid points of the boundary. If this test fails at any of these points the computational domain will be enlarged in the appropriate direction.

If the test passes at all these points the present computational domain will be considered as an appropriate one and will be used until the final solution is obtained.

In summary it is clear that the solution of equation (3.6.2.7) controls the size of the final computational domain used for this study.

4.3 Clustered Grid

The accuracy of the numerical solution depends on the spacing between the grid points. When large gradients are present, it is essential that this spacing is kept sufficiently small to ensure a good approximation. However, the total number of grid points are limited by the computational capacity. The use of variable increment grids provides for minimizing the total number of grid points used by locally clustering grid points where large gradients are expected to exist.

Since the boundary layer is a very thin region and the dependent variables have a high gradient in this region, the grid points need to be clustered near the flat plate surface in the direction normal to the plate (y-direction). This clustering provides a better resolution where the velocity gradient is high in this region. The nodes parallel to the direction of the flat plate are uniformly spaced. A suitable transformation of coordinates for a two-dimensional boundary-layer type of problem which clusters more points near $y = 0$ will be used here [32].

$$x = \bar{x} \quad (4.3.1)$$

$$y = h \frac{(\beta + 1) - (\beta - 1)\{[(\beta + 1)/(\beta - 1)]^{1-\bar{y}}\}}{[(\beta + 1)/(\beta - 1)]^{1-\bar{y}} + 1} \quad (4.3.2)$$

with

$$1 < \beta < \infty$$

where β is the stretching parameter for this transformation. As β approaches 1 more points will be clustered near $y = 0$. h is the height of the computational domain to be clustered. In this transformation x and y represent the y and x coordinates in a physical plane with non-uniform spacing while \bar{x} and \bar{y} represent the x and y coordinates in a computational plane with uniform spacing. The inverse of this transformation can be written as follows:

$$\bar{x} = x \quad (4.3.3)$$

$$\bar{y} = 1 - \frac{\ln\{[\beta + 1 - (y/h)]/[\beta - 1 + (y/h)]\}}{\ln[(\beta + 1)/(\beta - 1)]} \quad (4.3.4)$$

Usually after clustering the grid points it is more convenient to transfer the governing equations from the non-uniform physical plane to the uniform computational plane or in other words transferring the independent variables of the governing equations from the physical coordinates to the computational coordinates but because of the simple geometry of the flat plate in the model under investigation it will be easier to finite-difference the governing equations directly on the physical plane after clustering the grid in the y -direction.

The order of magnitude of the boundary layer thickness and the minimum value of the step size in the y -direction necessary to satisfy the stability conditions of the five-point scheme (used to approximate the Poisson's equation) restrict the number of the grid points inside the boundary layer. This restriction may affect the accuracy of the numerically-obtained velocity profiles and consequently the drag calculations. In order to overcome this restriction, two separate grids will be used; one grid for the electrostatic calculations which satisfies the stability conditions of the five-point scheme, and the other grid for the boundary layer calculations which provides an accurate velocity profile as possible. Because of the coupling between the electrostatic and the boundary layer equations and to transfer the

variables between the electrostatic and the boundary layer grids during the numerical solution, an interpolation scheme must be added to recalculate the body force term from the electrostatic grid to the boundary layer grid and to recalculate the velocity components of the flow from the boundary layer grid to the electrostatic grid. This means that two stretching parameter values will be used; a stretching parameter with relatively high value to satisfy the stability conditions of the five-point scheme and the other stretching parameter with a lower value to provide a reasonable number of grid points inside the boundary layer.

For the electrostatic grid, the height of the computational domain h in equation (4.3.2) has an impact on the step size of the clustered grid in the y -direction. Since the domain height will be relatively large to satisfy the boundary conditions of Poisson's equation it might be necessary to put a limit on the maximum value of the step size in the y -direction to satisfy the stability conditions of this scheme. It will be considered that any domain height will be originally divided into 200 nodes in the vertical direction. If the height is large enough to make the step size exceeds certain value which causes the numerical model to be unstable, a limit will be assigned on the maximum step size in this direction. If this case happened the number of the nodes will exceed the value of 200.

In order to demonstrate the grid spacing using this transformation, an example of a domain of height ($h=0.3$ m) is assumed and it will be divided into 200 nodes by using different values of the stretching parameter " β ". The maximum and the minimum values of the increments dividing the domain height for some selected stretching parameters are listed in Table 4.1. For $\beta > 4.0$, the grid spacing is almost uniform while the ratio of the maximum to the minimum increment increases as β decreases.

Figure 4.1 shows the non uniform grid spacing for some values of the stretching parameter β .

Table 4.1: Non uniform grid analysis

β	drmax [m]	drmin [m]	drmax/drmin	ng
1.001	0.0057	0.000012	491.22	40
1.002	0.0052	0.000021	246.43	30
1.005	0.0045	0.000046	99.25	19
1.008	0.0042	0.000067	62.38	14
1.01	0.004	0.00008	50.09	12
1.02	0.0035	0.00014	25.46	8
1.05	0.0029	0.00027	10.66	5
1.100	0.0025	0.00044	5.72	4
2.000	0.0016	0.0012	1.33	2
4.000	0.0015	0.0014	1.07	2

where:

drmax maximum step size in y-direction

drmin minimum step size in y-direction

ng number of grid points in the first mm above the plate surface

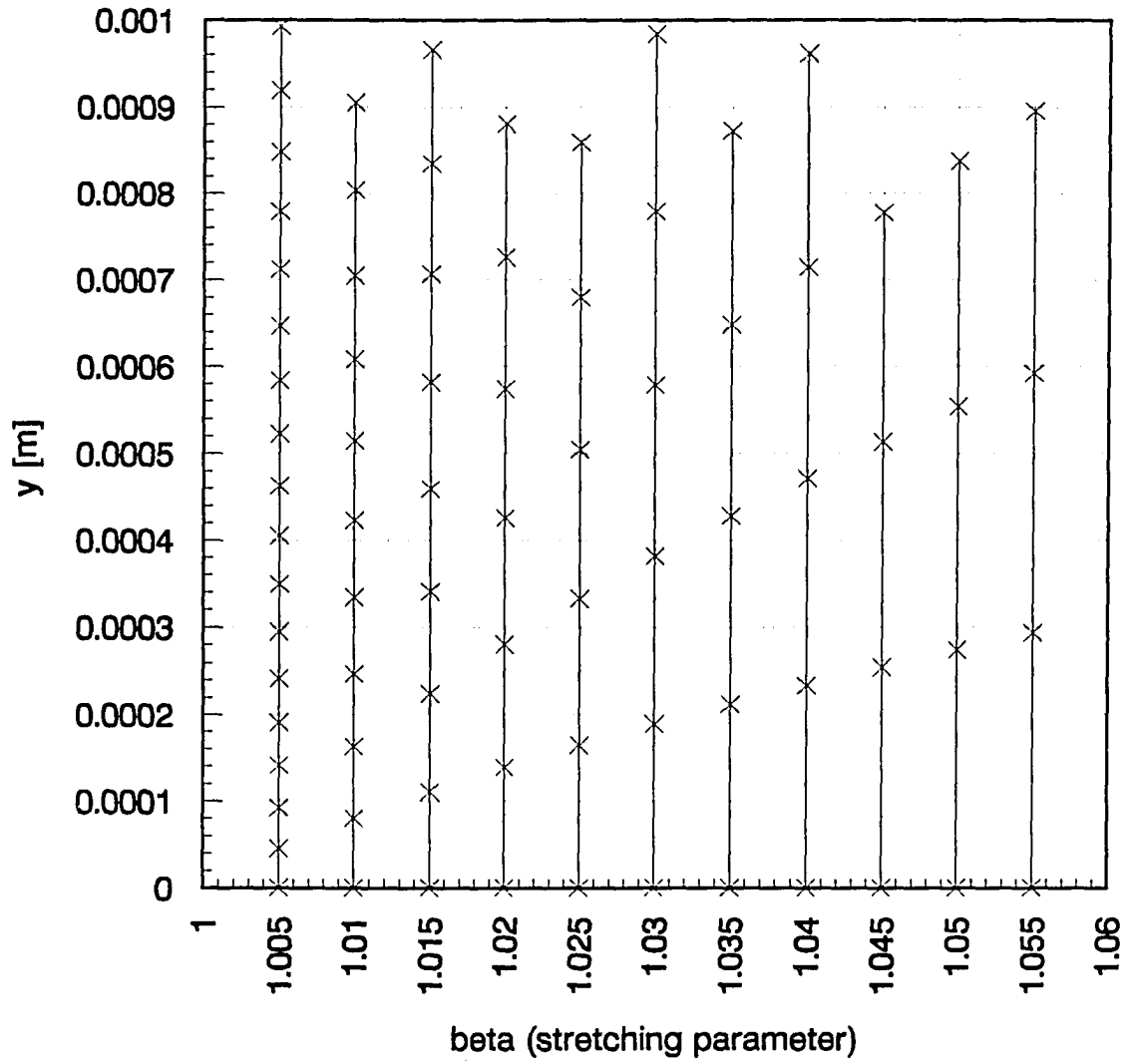


Figure 4.1: Grid spacing vs stretching parameter

4.3.1 Interpolation scheme

The cubic spline functions interpolation scheme has been employed to recalculate the variables between the electrostatic and the boundary layer grids. Interpolation using the cubic spline is very popular particularly for interpolation in relatively noise-free tables of physical properties [55]. A series of points, y_i , which are generally not evenly spaced and its corresponding $f(y_i)$ are given, ($i = 1, 2, \dots, n$). The cubic spline interpolating functions are generally constructed by fitting a cubic between each two points and use these cubics as the interpolating functions between these points. The interpolating function at any point, y , between the two points, y_i and y_{i+1} can be obtained in the form [55]

$$\begin{aligned}
 g(y) = F_i(y) = & \frac{g''(y_i)}{6} \left[\frac{(y_{i+1} - y)^3}{\Delta y_i} - \Delta y_i (y_{i+1} - y) \right] \\
 & + \frac{g''(y_{i+1})}{6} \left[\frac{(y - y_i)^3}{\Delta y_i} - \Delta y_i (y - y_i) \right] \\
 & + f(y_i) \left[\frac{(y_{i+1} - y)}{\Delta y_i} \right] + f(y_{i+1}) \left[\frac{(y - y_i)}{\Delta y_i} \right] \quad (4.3.1.1)
 \end{aligned}$$

where $\Delta y_i = y_{i+1} - y_i$, and $g(y)$ is called the natural cubic spline. The second derivatives of the cubic splines can be found by using the derivative matching conditions:

$$F'_i(y_i) = F'_{i-1}(y_i) \quad (4.3.1.2)$$

and

$$F''_i(y_i) = F''_{i-1}(y_i) \quad (4.3.1.3)$$

Applying these conditions to equation (3.4.1.1) for $i = 2, 3, \dots, n - 1$ and collecting terms yields a set of linear simultaneous equations of the form

$$\begin{aligned} & \left[\frac{\Delta x_{i-1}}{\Delta x_i} \right] g''(x_{i-1}) + \left[\frac{2(x_{i+1} - x_{i-1})}{\Delta x_i} \right] g''(x_i) + [1] g''(x_{i+1}) \\ & = 6 \left[\frac{f(y_{i+1}) - f(y_i)}{(\Delta y_i)^2} - \frac{f(y_i) - f(y_{i-1}))}{(\Delta y_i)(\Delta y_{i-1})} \right] \end{aligned} \quad (4.3.1.4)$$

where $\Delta y_{i-1} = y_i - y_{i-1}$

There are $n - 2$ equations in the n unknowns $g''(y_2), g''(y_3), \dots, g''(y_{n-1})$. The two necessary additional equations are obtained by specifying conditions on $g''(y_1)$ and $g''(y_n)$.

It is usually simply specified that

$$g''(y_1) = 0 \quad (4.3.1.5)$$

and

$$g''(y_n) = 0 \quad (4.3.1.6)$$

The set of equations (4.3.1.4) is now complete and can be solved simultaneously for $g''(y_2), g''(y_3), \dots, g''(y_{n-1})$.

After obtaining the second derivatives of the cubic splines at all the given points equation (4.3.1.1) can be used to determine the value of $f(y)$ at any other point.

4.4 Finite Differencing

Suitable finite difference schemes are chosen to each of the governing partial differential equations according to its mathematical nature. The derivatives in these equations will be approximated on the physical clustered grid. Figure 4.2 shows a general view of the non uniform grid on which the governing partial differential equations will be approximated.

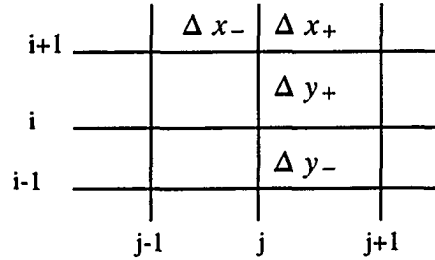


Figure 4.2 : Non uniform grid general view

where i and j are indices for the y and x coordinates respectively.

According to Figure 4.2 the non uniform grid step sizes in both x and y directions are defined as follows:

$$\begin{aligned}
 \Delta x_+ &= x(i, j+1) - x(i, j) \\
 \Delta x_- &= x(i, j) - x(i, j-1) \\
 \Delta y_+ &= y(i+1, j) - y(i, j) \\
 \Delta y_- &= y(i, j) - y(i-1, j)
 \end{aligned} \tag{4.4.1}$$

In order to approximate each of the derivatives in the governing partial differential equations on the non uniform grid the following finite approximations for a general variable u will be used [32]:

1- Central difference of first derivative with respect to x :

$$\frac{\partial u}{\partial x} = \frac{1}{2} \left[\frac{u(i, j+1) - u(i, j)}{\Delta x_+} + \frac{u(i, j) - u(i, j-1)}{\Delta x_-} \right] + O[\Delta x] \tag{4.4.2}$$

2- Central difference of first derivative with respect to y:

$$\frac{\partial u}{\partial y} = \frac{1}{2} \left[\frac{u(i+1, j) - u(i, j)}{\Delta y_+} + \frac{u(i, j) - u(i-1, j)}{\Delta y_-} \right] + O[\Delta y] \quad (4.4.3)$$

3- Forward difference of first derivative with respect to x:

$$\frac{\partial u}{\partial x} = \frac{u(i, j+1) - u(i, j)}{\Delta x_+} + O[\Delta x] \quad (4.4.4)$$

4- Forward difference of first derivative with respect to y:

$$\frac{\partial u}{\partial y} = \frac{u(i+1, j) - u(i, j)}{\Delta y_+} + O[\Delta y] \quad (4.4.5)$$

5- Backward difference of first derivative with respect to y:

$$\frac{\partial u}{\partial y} = \frac{u(i, j) - u(i-1, j)}{\Delta y_-} + O[\Delta y] \quad (4.4.6)$$

6- Central difference of second derivative with respect to x:

$$\frac{\partial^2 u}{\partial x^2} = \frac{2}{\Delta x_+ + \Delta x_-} \left[\frac{u(i, j+1) - u(i, j)}{\Delta x_+} - \frac{u(i, j) - u(i, j-1)}{\Delta x_-} \right] + O[(\Delta x)^2] \quad (4.4.7)$$

7- Central difference of second derivative with respect to y:

$$\frac{\partial^2 u}{\partial y^2} = \frac{2}{\Delta y_+ + \Delta y_-} \left[\frac{u(i+1, j) - u(i, j)}{\Delta y_+} - \frac{u(i, j) - u(i-1, j)}{\Delta y_-} \right] + O[(\Delta y)^2] \quad (4.4.8)$$

Using the above derivative approximations and choosing the suitable numerical scheme to approximate each of the governing partial differential equations, a system of algebraic equations will be obtained.

The five-point scheme is used to approximate Poisson's equation (equation 3.6.2.7). This is a second-order explicit scheme which has a truncation error of order $O[(\Delta x)^2, (\Delta y)^2]$ and is conditionally stable. The following finite difference equation can be obtained for this scheme at any general grid point inside the computational domain:

$$\phi(i, j) = b_1 \frac{\rho_c(i, j)}{\epsilon_0} + b_2 (\Delta x_- \phi(i, j+1) + \Delta x_+ \phi(i, j-1)) + b_3 (\Delta y_- \phi(i+1, j) + \Delta y_+ \phi(i-1, j)) \quad (4.4.9)$$

where

$$b_1 = \frac{\Delta x_+ \Delta x_- \Delta y_+ \Delta y_-}{2(\Delta x_+ \Delta x_- + \Delta y_+ \Delta y_-)}$$

$$b_2 = \frac{\Delta y_+ \Delta y_-}{(\Delta x_+ + \Delta x_-)(\Delta x_+ \Delta x_- + \Delta y_+ \Delta y_-)}$$

$$b_3 = \frac{\Delta x_+ \Delta x_-}{(\Delta y_+ + \Delta y_-)(\Delta x_+ \Delta x_- + \Delta y_+ \Delta y_-)}$$

Rewriting the charge conservation equation (equation 3.6.2.8) in the following form:

$$A \frac{\partial \rho_c}{\partial x} + B \frac{\partial \rho_c}{\partial y} + \frac{k}{\epsilon_0} \rho_c^2 = 0 \quad (4.4.10)$$

where

$$A = u - k \frac{\partial \phi}{\partial x} \quad (4.4.11)$$

and

$$B = v - k \frac{\partial \phi}{\partial y} \quad (4.4.12)$$

A first-order accurate upwind difference scheme or donor cell differencing [47] will be used to approximate the convective terms in equation (4.4.10). It has the stability of the upwind difference method. A similar technique but second-order has been used successfully by Prusa [48] and others [49,50].

Using equations (4.4.2, 4.4.3, 4.4.5) to approximate equations (4.4.11 and 4.4.12), the convective terms of equation (4.4.10) can be approximated on a general grid point inside the computational domain as follows:

$$A \frac{\partial \rho_c}{\partial x} = \frac{A - |A|}{2} \frac{\rho_c(i, j+1) - \rho_c(i, j)}{\Delta x_+} + \frac{A + |A|}{2} \frac{\rho_c(i, j) - \rho_c(i, j-1)}{\Delta x_-} \quad (4.4.13)$$

$$B \frac{\partial \rho_c}{\partial y} = \frac{B - |B|}{2} \frac{\rho_c(i+1, j) - \rho_c(i, j)}{\Delta y_+} + \frac{B + |B|}{2} \frac{\rho_c(i, j) - \rho_c(i-1, j)}{\Delta y_-} \quad (4.4.14)$$

On a general grid point on the lower side of the computational domain (flat plate surface) the first convective term of equation (4.4.10) is also approximated by equation (4.4.13) while the second convective term is approximated as follows:

$$B \frac{\partial \rho_c}{\partial y} = B \frac{\rho_c(i+1, j) - \rho_c(i, j)}{\Delta y_+} \quad (4.4.15)$$

Substituting back in equation (4.4.10) using equations (4.4.13, 4.4.14 and 4.4.15), the following equation is obtained inside the computational domain.

$$b\rho_c(i-1, j) + d\rho_c(i, j) + a\rho_c(i+1, j) = 0 \quad (4.4.16)$$

where

$$b = -\frac{|B| + B}{2\Delta y_-}$$

$$d = \frac{|A| - A}{2\Delta x_+} + \frac{|A| + A}{2\Delta x_-} + \frac{|B| - B}{2\Delta y_+} + \frac{|B| + B}{2\Delta y_-} + \frac{k}{\epsilon_0} \rho_c(i, j)$$

$$a = \frac{B - |B|}{2\Delta y_+}$$

$$c = \frac{|A| - A}{2\Delta x_+} \rho_c(i, j+1) + \frac{|A| + A}{2\Delta x_-} \rho_c(i, j-1)$$

and the following equation is obtained on the lower surface of the computational domain between the two electrodes

$$\rho_c(i, j) = [e\rho_c(i, j+1) + f\rho_c(i, j-1) + g\rho_c(i+1, j) + h\rho_c(i, j)]/i \quad (4.4.17)$$

where

$$e = \frac{|A| - A}{2\Delta x_+}$$

$$f = \frac{|A| + A}{2\Delta x_-}$$

$$g = -\frac{B}{\Delta y_+}$$

$$h = \frac{|B|+B}{\Delta y_+} + \frac{A}{2\Delta x_+} - \frac{A}{2\Delta x_-}$$

$$i = \frac{|A|}{2\Delta x_+} + \frac{|A|}{2\Delta x_-} + \frac{|B|}{\Delta y_+} + \frac{k}{\epsilon_0} \rho_c(i, j)$$

Equation (4.4.17) represents the boundary conditions of the charge density on the surface between the two electrodes which will be solved simultaneously with equation (4.4.16) during the marching process for the solution of the charge density in the domain between the two electrodes.

Rewriting the general boundary condition equation of the electric potential on the surface between the two electrodes (equation 3.7.2.2.4) as follows:

$$\sigma_s \frac{\partial^2 \phi}{\partial x^2} = -\rho_c k \frac{\partial \phi}{\partial y} \quad (4.4.18)$$

Using equations (4.4.5 and 4.4.7) to approximate equation (4.4.18), the following equation is obtained on the surface between the two electrodes when ion deposition from the gaseous phase to the surface current is considered.

$$\phi(i, j) = s(i, j) t(i, j) \phi(i+1, j) + t(i, j) \left[\frac{\phi(i, j-1)}{\Delta x_-} + \frac{\phi(i, j+1)}{\Delta x_+} \right] \quad (4.4.19)$$

where

$$s(i, j) = \frac{k(\Delta x_+ + \Delta x_-)}{2\sigma_s \Delta y_+} \rho_c(i, j)$$

$$t(i, j) = \frac{1}{s(i, j) + 1/\Delta x_+ + 1/\Delta x_-}$$

Rewriting the x-momentum equation which describes the fluid flow motion in the x-direction (equation 3.6.1.7) as follows:

$$u \frac{\partial u}{\partial x} + v \frac{\partial u}{\partial y} = \frac{1}{\rho} F_x + \nu \frac{\partial^2 u}{\partial y^2} \quad (4.4.20)$$

A fully implicit scheme with lagging the coefficients of the convective terms to linearize equation (4.4.20) will be used. This scheme has a truncation error of order $O[\Delta x, (\Delta y)^2]$ and is unconditionally stable. Using equations (4.4.4, 4.4.3) to approximate the convective terms and equation (4.4.8) to approximate the viscous term of equation (4.4.20) respectively, the following equation is obtained for the x-component of the fluid velocity at each computational station during the marching process.

$$bu(i-1, j) + du(i, j) + au(i+1, j) = 0 \quad (4.4.21)$$

where

$$b = - \left[\frac{v(i, j)}{2\Delta y_-} + \frac{2\nu}{\Delta y_-(\Delta y_+ + \Delta y_-)} \right]$$

$$d = \frac{u(i, j)}{\Delta x_+} - \frac{v(i, j)}{2\Delta y_+} + \frac{v(i, j)}{2\Delta y_-} + \frac{2\nu}{\Delta y_+\Delta y_-}$$

$$a = \frac{v(i, j)}{2\Delta y_+} - \frac{2\nu}{\Delta y_+(\Delta y_+ + \Delta y_-)}$$

$$c = \frac{u(i, j)u(i, j)}{\Delta x_+} + \frac{1}{\rho} F_x(i, j+1)$$

A marching process starting from the flat plate surface and proceeding normally to it will be used on the continuity equation (equation 3.6.1.6) to obtain the y-component of the fluid flow velocity. Using equations (4.4.4 and 4.4.6) to approximate equation (3.6.1.6), the following equation will be obtained.

$$v(i, j + 1) = \frac{\Delta y_-}{\Delta y_+} [u(i, j) - u(i, j + 1)] + v(i - 1, j) \quad (4.4.22)$$

In summary equations (4.4.9, 4.4.16, 4.4.17, 4.4.19, 4.4.21 and 4.4.22) represent the system of the governing algebraic equations which will be used in the FORTRAN code.

4.4.1 Integration scheme

To verify the current conservation statement around the positive electrode, equations (3.7.2.3.7 and 3.7.2.3.8) are combined into one equation which can be written here as:

$$I = k \int \rho_c \vec{E} \cdot d\vec{A} \quad (4.4.1.1)$$

If the positive electrode is upstream and the positive ions are traveling along the positive direction of the x-axis, equation (4.4.1.1) can be written as follows:

$$I = kb \left[\int_{y_1}^{y_2} \rho_c E_x dy + \int_{x_1}^{x_2} \rho_c E_y dx \right] \quad (4.4.1.2)$$

where x_1, x_2, y_1 and y_2 are the limits of the integrals on each side of the control surface around the positive electrode. In equation (4.4.1.2), b is the width of the plate and to

calculate the current per unit length b will be considered as a unity, ρ_c is the local charge density, and E_x and E_y are the local electric field strength in the x and y directions.

$$E_x(i, j) = 0.5 \left[\frac{\phi(i, j) - \phi(i, j + 1)}{\Delta x_+} + \frac{\phi(i, j - 1) - \phi(i, j)}{\Delta x_-} \right] \quad (4.4.1.3)$$

$$E_y(i, j) = 0.5 \left[\frac{\phi(i, j) - \phi(i + 1, j)}{\Delta y_+} + \frac{\phi(i - 1, j) - \phi(i, j)}{\Delta y_-} \right] \quad (4.4.1.4)$$

where $\Delta x_+, \Delta x_-, \Delta y_+, \Delta y_-$ are defined as in equation (4.4.1)

In order to numerically evaluate the integration in equation (4.4.1.2), Gauss quadrature scheme [55] has been employed.

$$I = \frac{b-a}{2} \sum_{k=1}^m w_k f(x_k) \quad (4.4.1.5)$$

where a and b are the limits of the integral, x_k are the m unequally spaced points determined by the type and degree of the orthogonal polynomial used, and w_k are the weight factors. x_k are determined according to the following formula:

$$x_k = \frac{b+a}{2} + \frac{b-a}{2} \xi_k \quad (4.4.1.6)$$

where ξ_k are the m zeros of the m^{th} degree Legendre polynomials.

Using Gauss quadrature with $m = 4$ and obtaining the zeros and the weights from tables [55]. These values are presented in Table 4.2. The values of ρ_c , E_x , and E_y are obtained at the Gauss points from its corresponding values on the electrostatic grid through the interpolation scheme.

Table 4.2: Zeros and weights for Gauss quadrature

ξ_k	w_k
± 0.3399810436	0.652145154
± 0.8611363116	0.3478548451

4.4.2 Thomas algorithm

A fully implicit scheme will be used during the marching process when solving the x-momentum equation and the conservation of charge equation. At every computational station a tridiagonal system of equations will be constructed in a matrix form. The dependent variable is known only at the two boundary points of the station (the point on the flat plate surface and the far away point from the flat plate) and is unknown at the rest of the grid points of the station. A simultaneous solution will be carried out on these equations to solve for the dependent variable at all grid points of the station. To solve for the vector of the unknowns, Thomas algorithm [32] will be applied to the matrix of coefficients. The tridiagonal matrix will be put into an upper triangular form by replacing the different elements of this matrix by,

$$d_j = d_j - \frac{b_j}{d_{j-1}} a_{j-1} \quad (4.4.2.1)$$

$$c_j = c_j - \frac{b_j}{d_{j-1}} c_{j-1} \quad (4.4.2.2)$$

where:

- b_j Coefficient behind (to the left of) the main diagonal
- d_j Coefficient of the main diagonal

- a_j Coefficient ahead (to the right of) the main diagonal
 c_j Element in the constant vector

then the vector of the unknowns will be computed from back substitution according to

$$u_n = \frac{c_n}{d_n} \quad (4.4.2.3)$$

for the last element in the vector of the unknowns and then for the rest of the elements according to

$$u_k = \frac{c_k - a_k u_{k+1}}{d_k} \quad (4.4.2.4)$$

where:

- n rank of the last element in the vector
 $k = n - 1, n - 2, \dots, 1$

4.4.3 Convergence criteria

During the electrostatic solution the equations are numerically iterated between Poisson's equation and the conservation of charge equation until the iterations converge to within a prescribed tolerance. Iterations are considered to be converged to the numerical solution if the following conditions are satisfied on the electric potential and the electric charge density throughout the computational domain.

$$|\phi^{k+1} - \phi^k| < \tau_\phi$$

$$|\rho_c^{k+1} - \rho_c^k| < \tau_{\rho_c}$$

In a similar way, during the transition between the electrostatic solution and the boundary layer solution the iterations are considered to be converged to the numerical solution if the following condition is satisfied on the velocity components throughout the computational domain.

$$|u^{k+1} - u^k| < \tau_u$$

where k refers to the iteration number during one domain scan and τ is the prescribed tolerance.

4.4.4 Stability condition of five-point scheme

During the simultaneous solution of Poisson's equation over the computational domain with the five-point scheme the stability conditions should be considered to stop the error growth while the computations are being performed between iterations. Since the grid spacing is non uniform and the equation contains a source term which varies from point to point it will be appropriate to determine the stability condition computationally. The result of this stability analysis is presented in chapter 5.

4.4.5 Relaxation scheme

This technique is applied in an attempt to accelerate the iterative procedure during the solution of the Poisson's equation. The basic idea is to correct the dependent variable between iterations towards the anticipated direction of the solution. The following equation is used for a general variable u to handle this correction between iterations [32].

$$u_{i,j}^{k+1} = u_{i,j}^k + w(u_{i,j}^{k+1} - u_{i,j}^k) \quad (4.4.5.1)$$

where:

- k refers to the iteration number
 $u_{i,j}^{k+1}$ most recent value of the variable
 $u_{i,j}^k$ value from the last iteration as adjusted previously by equation (4.4.5.1)
 $u_{i,j}^{k+1}$ newly adjusted variable
 w relaxation parameter

The formula is applied immediately at each point to the most recent value of the variable and replaces it with the newly adjusted variable in all subsequent calculations.

When w has a value between 1 and 2 over-relaxation is being employed. The optimum value of w and the limitation of its application is presented in chapter 5 when discussing the results of this study.

4.5 Drag Calculations

The last step in the numerical solution after developing the velocity profiles along the flat plate with and without the corona discharge effect is to carry out the drag calculations to demonstrate the changes in the total drag force due to the effect of the corona which is the primary objective of this study.

The local shear stress is approximated by applying equation (4.4.6) to equation (3.9.1) and the following finite-difference equation is obtained on the surface of the plate.

$$\tau_w(j) = \mu \frac{u(2,j) - u(1,j)}{\Delta y_+} + O[\Delta y] \quad (4.5.1)$$

The grid size step in the y-direction near the flat plate surface is very small inside the boundary layer when the velocity gradient is large while it becomes large outside the boundary layer when the velocity gradient is negligible. Under these conditions it is appropriate to apply the trapezoidal rule to carry out the necessary integration to calculate the

drag force per unit width according to equation (3.9.3). The following quadrature formula is applied to the integral on the right hand side of that equation.

$$I = \sum_{i=2}^m \frac{u(i, j) * u(i, j) + u(i - 1, j) * u(i - 1, j)}{2} \Delta y_- \quad (4.5.2)$$

where m is the total number of the grid points in the y-direction and j is computational station number.

It is also appropriate to apply the same rule to calculate the drag force per unit width by integrating the shear stress along the flat plate since the grid step size in the x-direction between the two electrodes is generally small. The following quadrature formula can be obtained for equation (3.9.2) to calculate this drag per unit width.

$$D(j) = \sum_{j=2}^{j=n} \frac{\tau_w(i, j) + \tau_w(i, j - 1)}{2} \Delta x_+ \quad (4.5.3)$$

where n is the total number of the grid points in the x-direction.

4.6 Computational Procedure

The zone which affects the variable at a point is called the zone of dependence. The zone which can be reached by signals sent from a particular point is called the zone of influence. The zones of dependence and influence for an elliptic type of differential equation are the whole computational domain. The dependence zone for a parabolic type of differential equation is the part of the computational domain upstream of the computational station while the influence zone is the part downstream of the computational station. Since equations (3.6.2.7) and (3.6.2.8) are coupled and the whole system is coupled with the boundary layer equations (3.6.1.6) and (3.6.1.7), a transition between an equilibrium problem solution and a marching problem solution will be followed.

The setup of the two electrodes shown in Figure 2.2 will be assumed to be located at a position downstream of the leading edge of the flat plate. The computational domain will be chosen to be of rectangular shape bounded at the bottom by the flat plate. The closed domain will be used to solve the elliptic equation. The vertical section at the leading edge of the flat plate will be considered as the left side of the computational domain. The next vertical section is the first computational station for the marching process during the boundary layer solution. The vertical section above the positive electrode will be considered as the first computational station for the marching process for the solution of the conservation of charge equation.

The numerical solution starts by preparing the boundary and the initial conditions prescribed earlier, reading all the computational parameters, and covering the computational domain with the appropriate electrostatic grid. The finite difference equations obtained in the previous section then will be solved simultaneously.

During the numerical solution the two electrodes are considered as point electrodes and the values of the electric potential at these two electrodes are prescribed while the values of the electric potential at all other grid points will be obtained numerically. The numerical solution for the electric charge density will start with an approximate value at the positive electrode and the electric charge density at all other grid points will be obtained numerically. An iterative procedure will be carried out on the value of the charge density at the positive electrode until its value satisfies the value of the predicted corona current in the domain under investigation.

When the numerical solution of the electrostatic equations converges the body force term will be calculated at all grid points and then the scheme will switch to the boundary layer solution. The boundary layer grid is generated and the body force term is interpolated from the electrostatic grid to the boundary layer grid. The numerical solution of the

boundary layer equations provides the values of the flow velocity components at all grid points. The scheme will switch back with these velocity components after interpolating it to the electrostatic grid at all grid points to the electrostatic equations to account for the convective effect on the electric current. This back and forth procedure between the electrostatic equations and boundary layer equations will continue until both converge.

The last step of the numerical solution is the calculations of the drag force acting on the flat plate with and without the corona effect for different values of flow velocities to evaluate the corona discharge as a new technique of drag reduction and boundary layer control. Figure 4.2 represents the general algorithm of the numerical solution. The details of the numerical solution will be clarified below in the description of Figure 4.2.

In Figure 4.2, "KL" is a flag used to obtain both the velocity profiles with and without the effect of the corona discharge and "kbl" is a flag used to check the convergence of the final solution. Also in this figure each block represents a subroutine which is doing a specific task in the process of the numerical solution. The different tasks of each subroutine is prescribed as follows:

INPUT: This subroutine receives all input parameters and prepares necessary information for the entire program.

ELECTRO: It is the main subroutine which handles the electrostatic solution. At the beginning it calls GRID to generate the optimum grid required for the numerical solution. Then ELECTRO calls BC to get the boundary conditions and the initial guess for the electric potential and the charge density. It starts the electrostatic solution by solving Laplace equation over the entire computational domain and uses this solution as initial guess before it starts the iteration procedure between Poisson's equation and the conservation of charge equation by calling back and forth POISSON and CCE. This continues the iteration procedure until the solution converges. It determines the appropriate computational domain

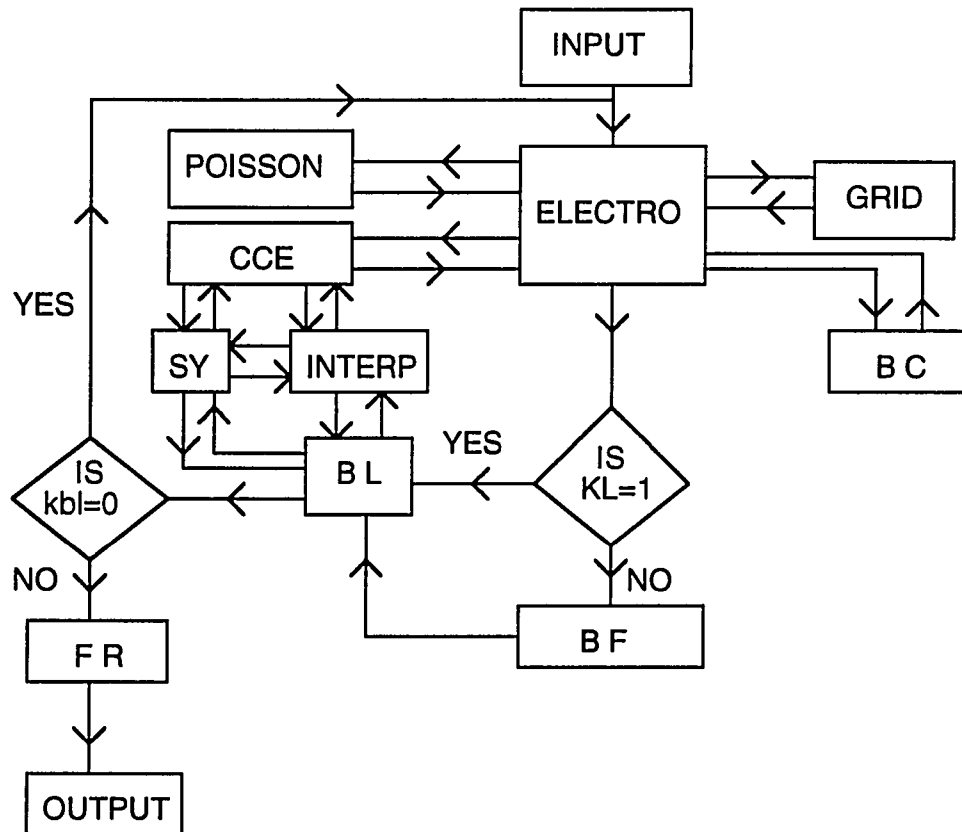


Figure 4.3: General algorithm of the numerical solution

size. It carries out the iteration procedure around the positive electrode until the appropriate value of the charge density which satisfies the corona current in the domain is reached. The output of this subroutine is the final distribution of the electric potential and the electric charge density over the whole computational domain which will be used to calculate the body force term due to the corona discharge in BF.

GRID: This subroutine generates the optimum two-dimensional grid with uniform spacing in the x-direction and non uniform spacing in the y-direction. It considers the maximum step size in the y-direction which is necessary for the stability condition of the five-point scheme which solves Poisson's equation in POISSON. It is called from ELECTRO.

BC: This subroutine provides the boundary conditions on the bottom side of the computational domain and the initial guess of the electrostatic dependent variables over the entire domain. There are two study cases. BC1 considers the flat plate as the entire bottom side of the computational domain for the preliminary calculations. BC2 handles the actual model under investigation which considers the flat plate as part of the bottom side of the computational domain while the other part is the free space in the upstream direction of the leading edge of the flat plate.

POISSON: This subroutine solves simultaneously Poisson's equation by using the five-point scheme over the entire computational domain. It also solves simultaneously the general boundary condition equation with Poisson's equation when ion deposition from the gaseous phase to the surface current is considered. It applies the successive over relaxation technique to accelerate the convergence of the solution when solving Laplace equation. The output of this subroutine is the electric potential distribution over the interior grid points of the computational domain.

CCE: This subroutine solves the conservation of charge equation simultaneously on the surface between the two electrodes and the interior of the computational domain by using the upwind fully implicit scheme. CCE is using a marching process in the direction of the traveling positive ions. The direction of the marching process depends on the order of polarity of the two electrodes. CCE marches in the positive direction of the x-axis in the case of downstream directed corona force and marches in the negative direction of the x-axis in the case of upstream directed corona force. At each computational station during the marching process it constructs a tridiagonal system of equations in a matrix form and calls SY which solves for the vector of the unknowns. The output of this subroutine is the electric charge density distribution over the grid points in the range between the two electrodes.

INTERP: This subroutine interpolates the dependent variables between the electrostatic grid and the boundary layer grid. The cubic spline functions are used for this purpose.

SY: This subroutine solves a tridiagonal system of equations by applying the Thomas algorithm.

BF: This subroutine calculates the body force term due to the corona discharge over the range between the two electrodes in the computational domain by using the output of ELECTRO.

BL: This subroutine solves the boundary layer equations. It uses the free stream flow velocity as initial condition at the first computational station located perpendicular to the flat plate at its leading edge. It uses the no slip condition on the flat plate surface and the free stream velocity far away from the flat plate as boundary conditions. It uses a marching process in the direction of the positive direction of the x-axis. BL does not consider the body force term at the beginning to solve and save the velocity profiles before applying the corona discharge and then considers the body force term when the corona discharge is in effect and

solve for the velocity profiles again. BL uses a fully implicit scheme with lagging coefficients to linearize the x-momentum equation to solve for the x-component of the flow velocity inside the boundary layer. At each computational station during the marching process it constructs a tridiagonal system of equations in a matrix form and calls SY which solves for the vector of the unknowns. It solves the continuity equation for the y-component of the flow velocity at each computational station by marching from and perpendicular to the flat plate surface to the free stream flow outside the boundary layer. The output of this subroutine is the boundary layer velocity profiles at each computational station with and without the effect of the corona discharge.

FR: This subroutine calculates the final results using the output of ELECTRO and BL to show the effect of the corona discharge on the boundary layer control and drag reduction of the model under investigation.

OUTPUT: This subroutine prepares a set of data files which will be used to demonstrate graphically the output of this study.

4.7 Computational Parameters

The dimensionless parameters that characterize the numerical solution of the present study can be separated into two different categories. The first category is the physical parameters which are part of the problem: Re_L , Re_x , C_D and C_f . The second category is the computational parameters which are associated with the numerical formulation and the solution of the problem: the percentage drag reduction $DR\%$, stretching parameter β , size of the step in vertical direction, number of nodes in horizontal direction, number of nodes in vertical direction, the convergence tolerance τ , and the relaxation parameter w .

The stretching parameter is a critical one for this study. The smaller its value, the smaller the step size near the plate surface, the higher the accuracy of the velocity profile and

the drag calculations. Its minimum value is restricted by the stability conditions of the five-point scheme approximating Poisson's equation. An optimum value for this parameter has to be determined for each case.

The convergence tolerance τ will be assigned a value depending on the quantity under the iterative procedure. There are three convergence tolerance parameters for this study. The tolerance in the electric potential τ_ϕ has been assigned a value of "5.0" since we are dealing with a potential value in the order of thousands. The tolerance in the electric charge density τ_ρ has been assigned a value of "1.0e-06" since we are dealing with a charge density in the order of "1.0e-03". The tolerance in the fluid velocity τ_u has been assigned a value of "1.0e-05" since we are dealing with a velocity in the order of meters per second and inside the boundary layer it may have a value of millimeters/second. The tolerance in the calculated corona current τ_i has been assigned a value of $\pm 2\%$ of the predicted corona current.

5. RESULTS AND DISCUSSIONS

Results obtained using the numerical model developed in this study are presented and discussed in this chapter. The study on the effect of corona discharge as a means of drag reduction and boundary layer control is interested in two major results: understanding the phenomena of corona discharge near surface of finite conductivity and its ability to create an ionic wind, and the effect of this ionic wind in reducing the momentum deficit of the fluid flow around a body in such a way to reduce its total drag. Therefore, this study considered the analysis and the evaluation of the corona discharge as an electrostatic phenomena followed by the evaluation of its effect on the boundary layer fluid flow by increasing its momentum which reduces the total drag on the body and delays the flow separation on the suction side of the body in such a way to improve its flight characteristics.

5.1 Corona Discharge

The model under investigation considers dc positive corona between wire-to-wire electrodes. This means that the charge carriers are only positive ions and the positive electrode (corona wire) is the only source of ions in the domain. It is assumed that the two electrodes are thin wires of circular cross section immersed flush on a dielectric material surface of finite surface conductivity (glass).

5.1.1 Corona onset voltage

Corona onset voltage is the minimum required electric potential difference between the two electrodes to initiate corona current between these electrodes. It has been found that the value of that voltage is increasing as the diameter of the corona wire increases and also as the gap length between the two electrodes increases. Figure 5.1 demonstrates this result for a corona wire diameter ranging from 1.0 up to 500.0 micrometers and a gap length ranging from

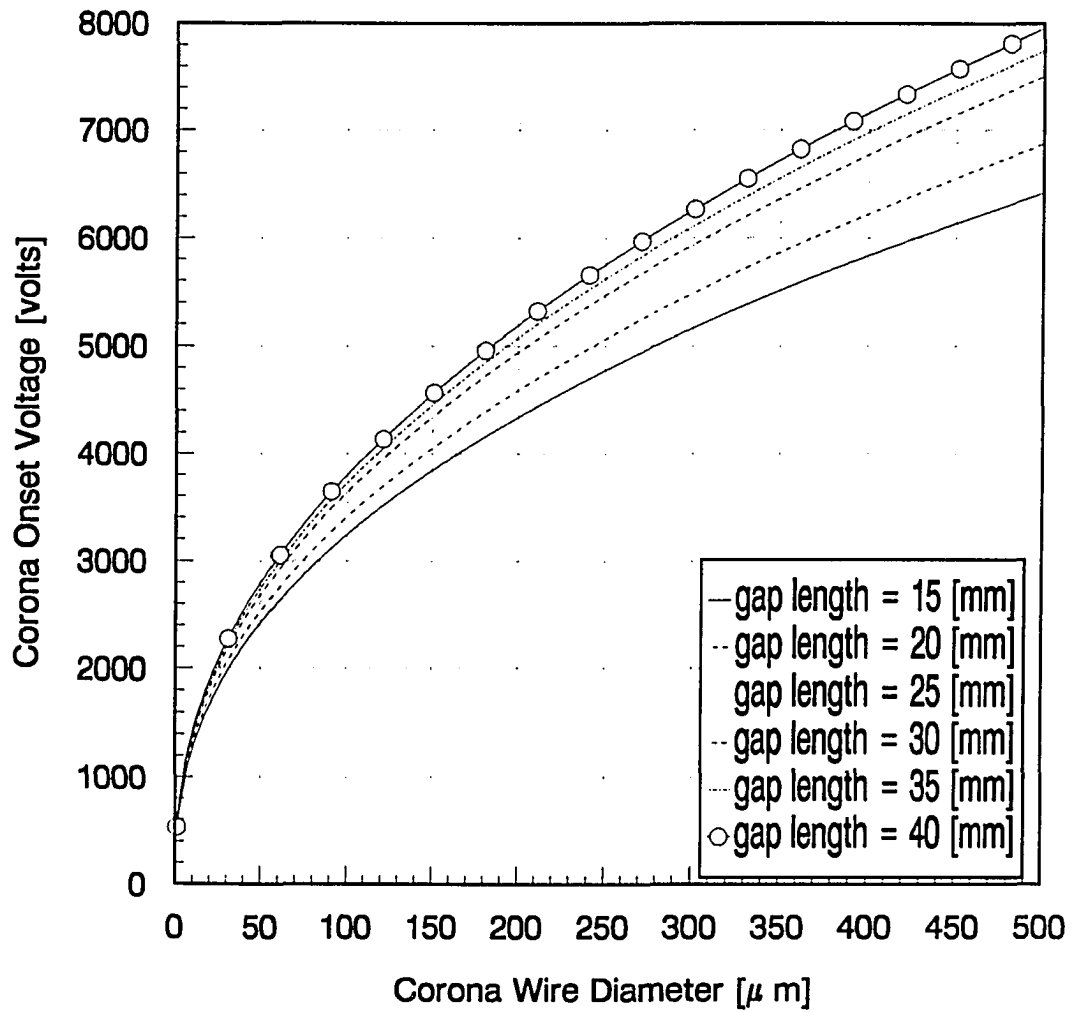


Figure 5.1: Corona onset voltage for various corona wire sizes at different gap lengths between electrodes

15.0 mm up to 40.0 mm.

5.1.2 Corona current

5.1.2.1 Seaver's equation and Soetomo's data

The corona current is an important parameter for this study. Soetomo's data has been fit into Seaver's equation by using the least-square curve fit technique (see appendix B). Figure 5.2 shows the corona current for a corona wire of 28.0 mm length and 2.0 micrometers diameter of both Soetomo's data and Seaver's equation. It is concluded that the corona current is very low in the order of few micro amperes for a potential difference between the electrodes of 10.0 kilovolts or less and the change in the corona current in this range is very small versus the variation of the potential difference between the two electrodes. At a potential differences higher than 10.0 kilovolts the corona current increases at a higher rates with increasing the potential difference between the two electrodes.

The corona current varies versus both the corona wire diameter and the gap length between electrodes but this variation also varies from negligible to significant. The corona current has been analyzed for a 1.0-m-length corona wire for a range of corona wire diameters and a range of gap lengths between electrodes. The corona current decreases at the same potential difference between electrodes as the diameter of the corona wire increases as shown in Figures 5.3, 5.4, 5.5, 5.6, and 5.7. For small corona wire diameters the change in the corona current at same potential difference between the electrodes is negligible versus the change in gap length between electrodes as it is clear in Figures 5.3 and 5.4. For larger corona wire diameters (order of 100.0 μm) the corona current slightly decreases as the gap length between electrodes increases as shown in Figures 5.5 and 5.6. Figure 5.7 shows that for larger diameters (order of 500.0 μm) the decrease in corona current versus gap length increase is significant.

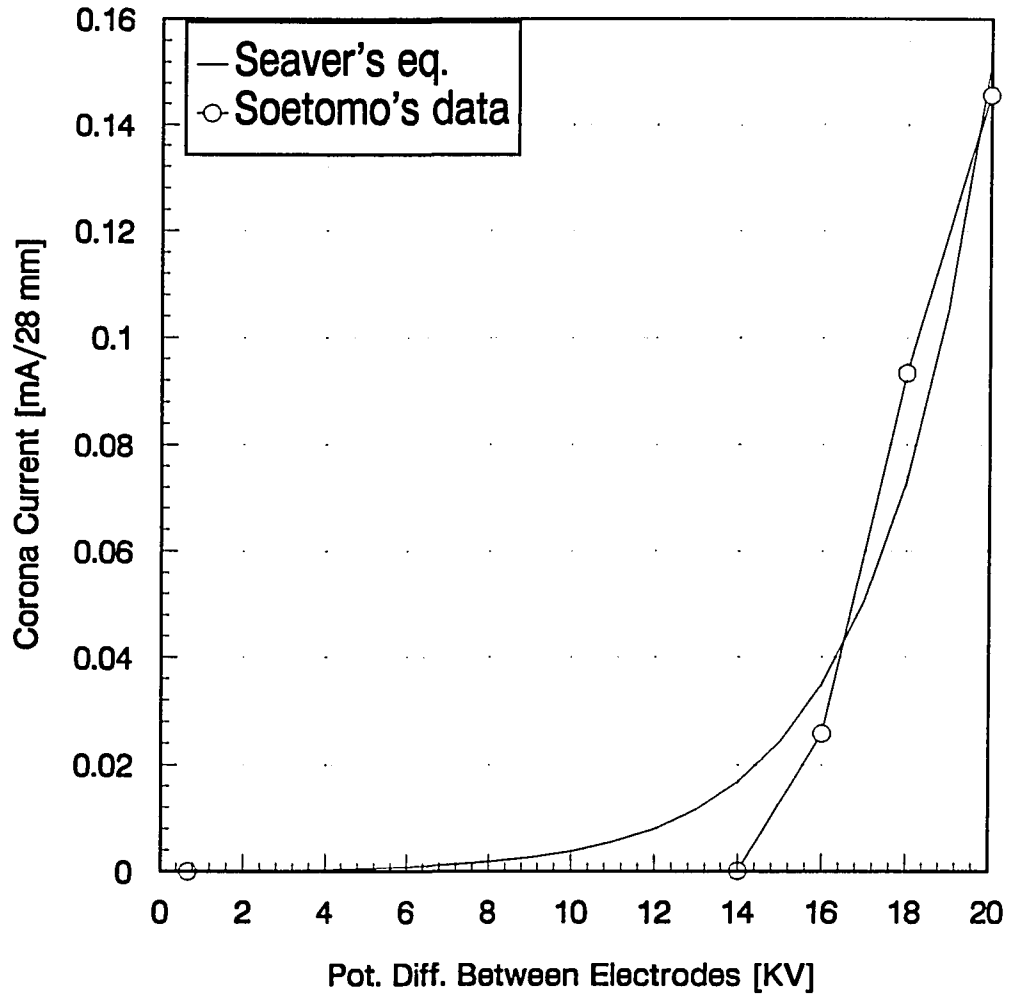


Figure 5.2: Fitting of Soetomo's data into Seaver's equation
 for $d_s=2.0 \mu m$, $L=25.0 mm$, $L_2=28.0 mm$, $V_0=680.27 volts$
 (Seaver's equation coefficients; $a_0=0.365 [kV]^{-1}$, $b=7615 [mA]^{-1}$)

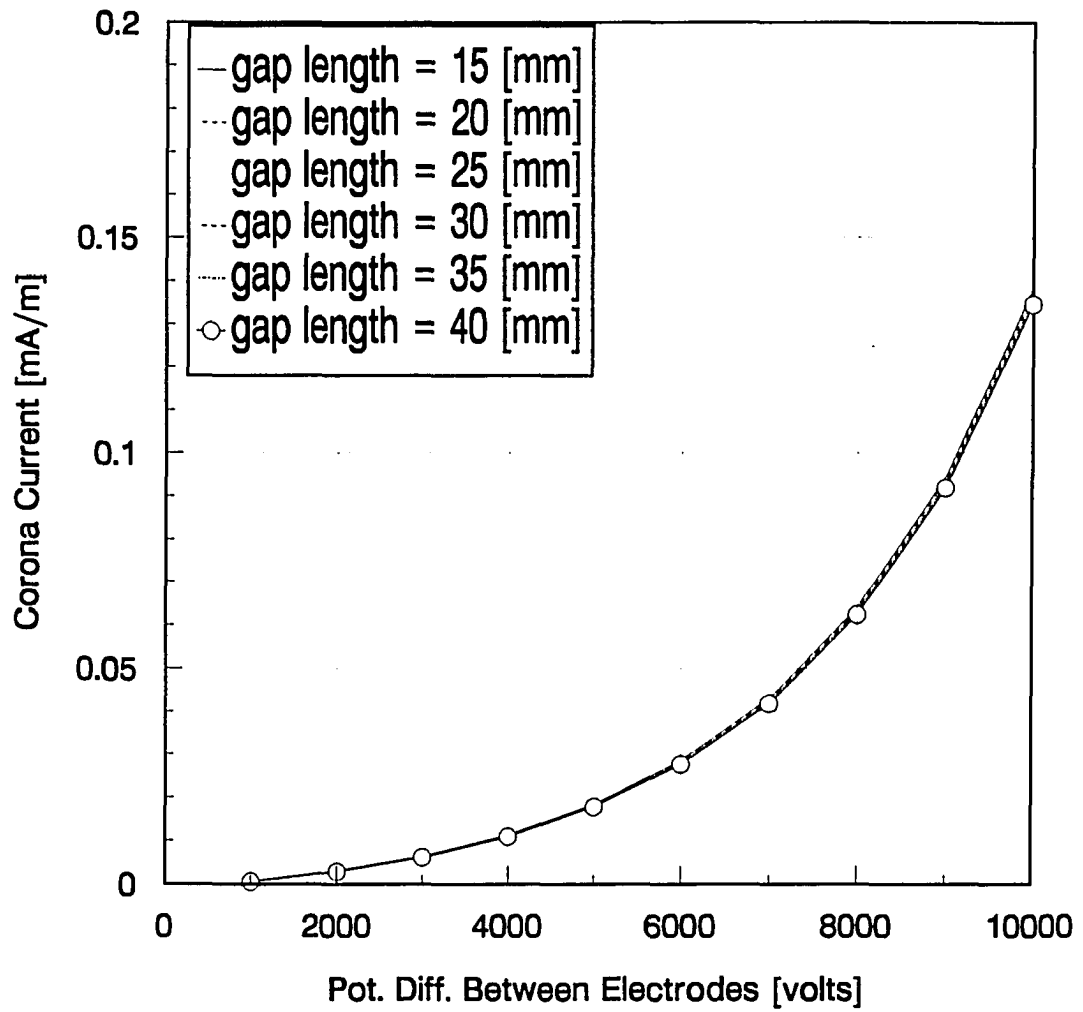


Figure 5.3: Corona current due to $2\text{-}\mu\text{m}$ -diameter corona wire for various potential differences and gap lengths between electrodes

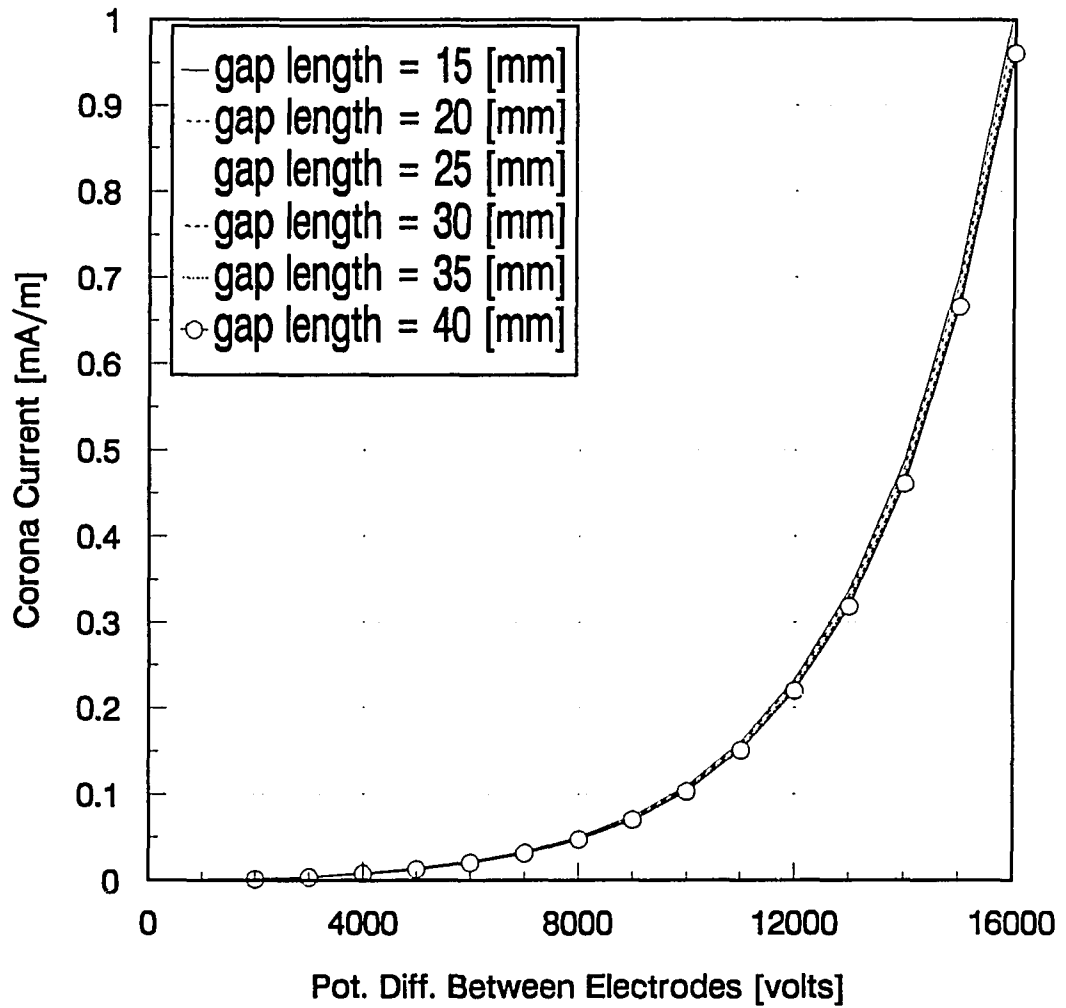


Figure 5.4: Corona current due to $10\text{-}\mu\text{m}$ -diameter corona wire for various potential differences and gap lengths between electrodes

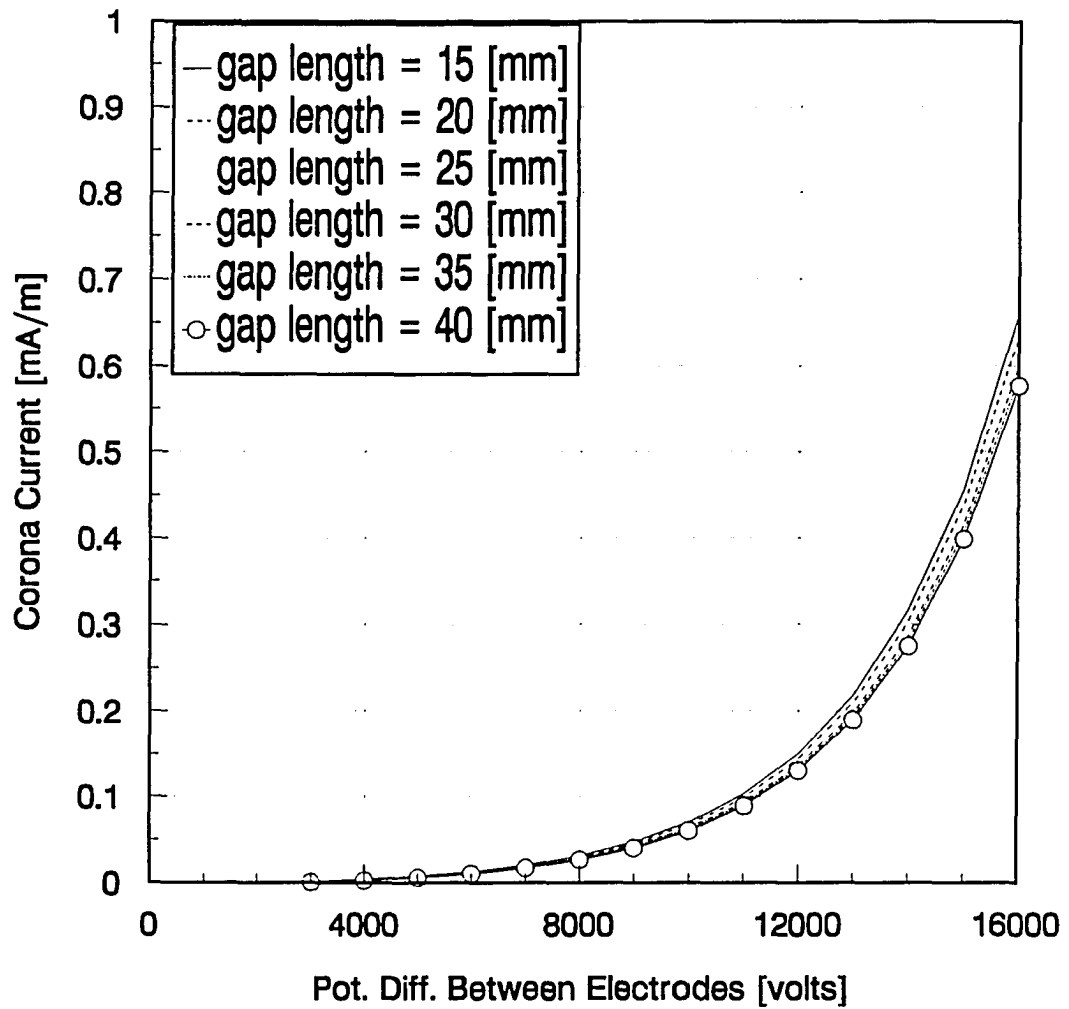


Figure 5.5: Corona current due to $50\text{-}\mu\text{m}$ -diameter corona wire for various potential differences and gap lengths between electrodes

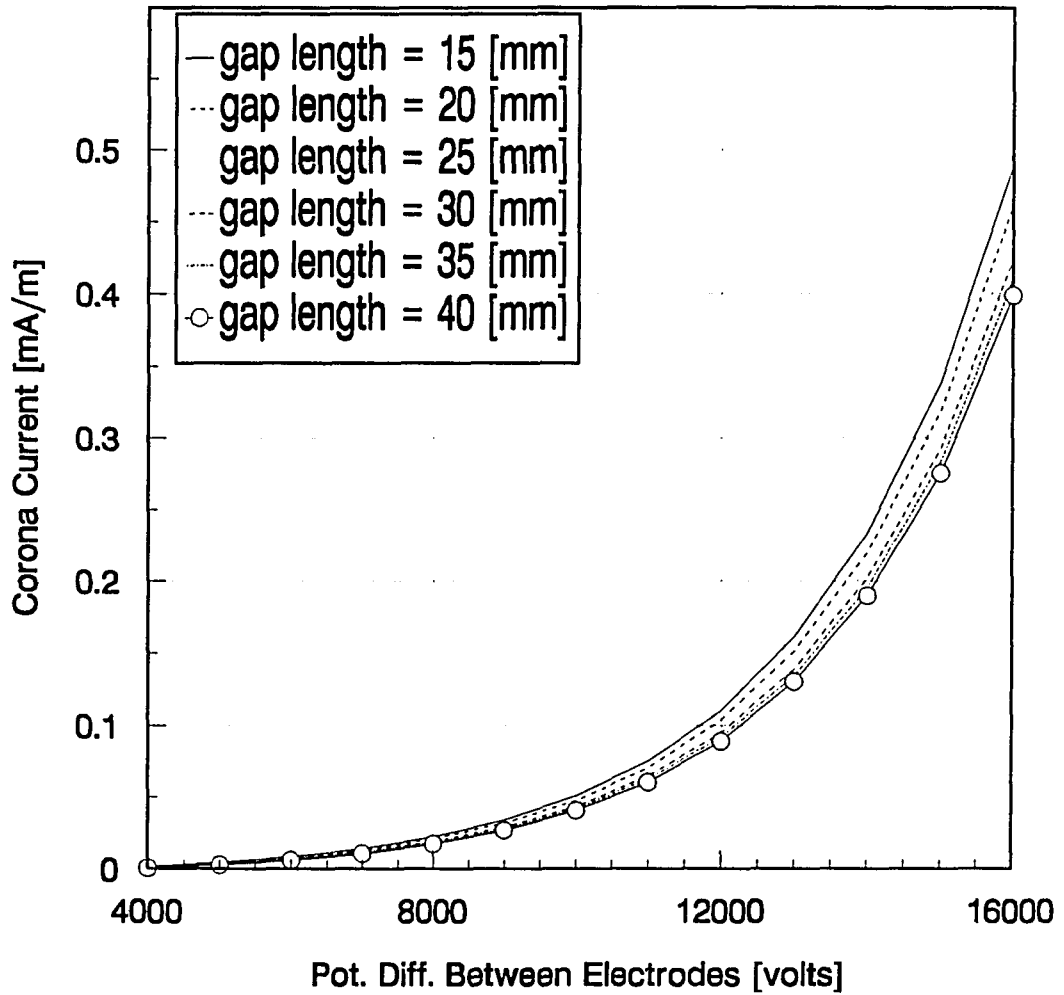


Figure 5.6: Corona current due to $100\text{-}\mu\text{m}$ -diameter corona wire for various potential differences and gap lengths between electrodes

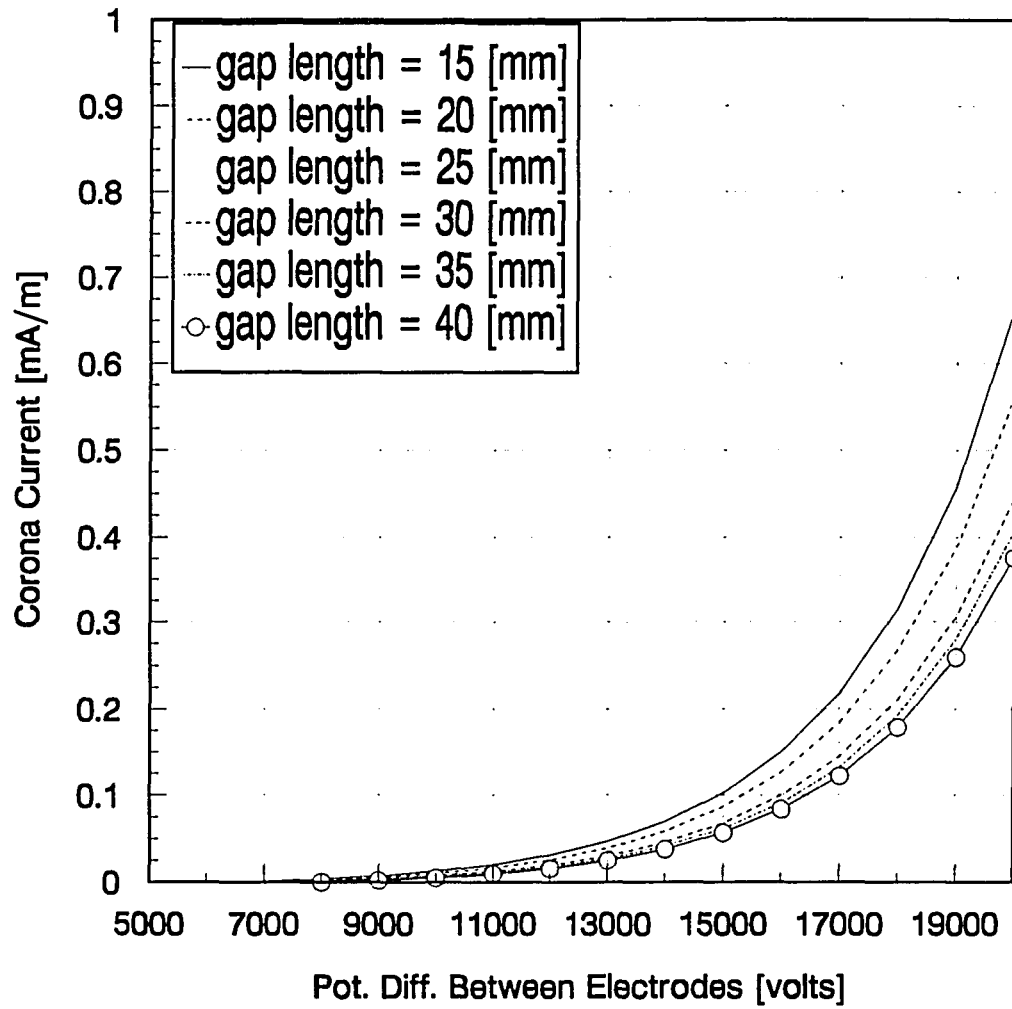


Figure 5.7: Corona current due to 500- μ m-diameter corona wire for various potential differences and gap lengths between electrodes

5.1.3 Boundary condition of the charge density at the interface

Examining both the numerical and the analytic solutions of the charge density at the interface between the two electrodes for the condition of non-ion deposition to the surface has shown good agreement. As it is clear in Figure 5.8 as the step size of the grid becomes smaller the numerical solution becomes closer to the analytic solution. This agreement between the two solutions adds confidence in the numerical solution at the interface and generally in the whole computational domain.

5.1.4 Electrostatic study cases

Examining both study cases for the numerical simulation of the electrostatic equations before it is used to calculate the body force term in the boundary layer equations provides additional confidence in the numerical modeling of the present study and the anticipated results of using the corona discharge as a means of drag reduction and boundary layer control. In both cases the ion deposition to the surface and its contribution to the surface current between the two electrodes will and will not be considered. The condition of non-ion deposition to the surface is an artificial one in which we force the vertical component of the electric field on the surface to be zero.

5.1.4.1 Study case 1

Although this case is not of practical importance, its symmetry stems a good check for the numerical simulation. The plate surface between the two electrodes is assumed to be of finite conductivity while it is assumed to be completely insulator outside the electrodes. The two electrodes are assumed to be of circular cross section of $2\text{-}\mu\text{m}$ -diameter. The corona wire is maintained at 2000 volts and the other electrode is maintained at -2000.0 volts . The gap length between the two electrodes is 25 mm . The computational domain has a 12-gap-lengths height and a 9-gap-lengths width. The bottom side of the computational

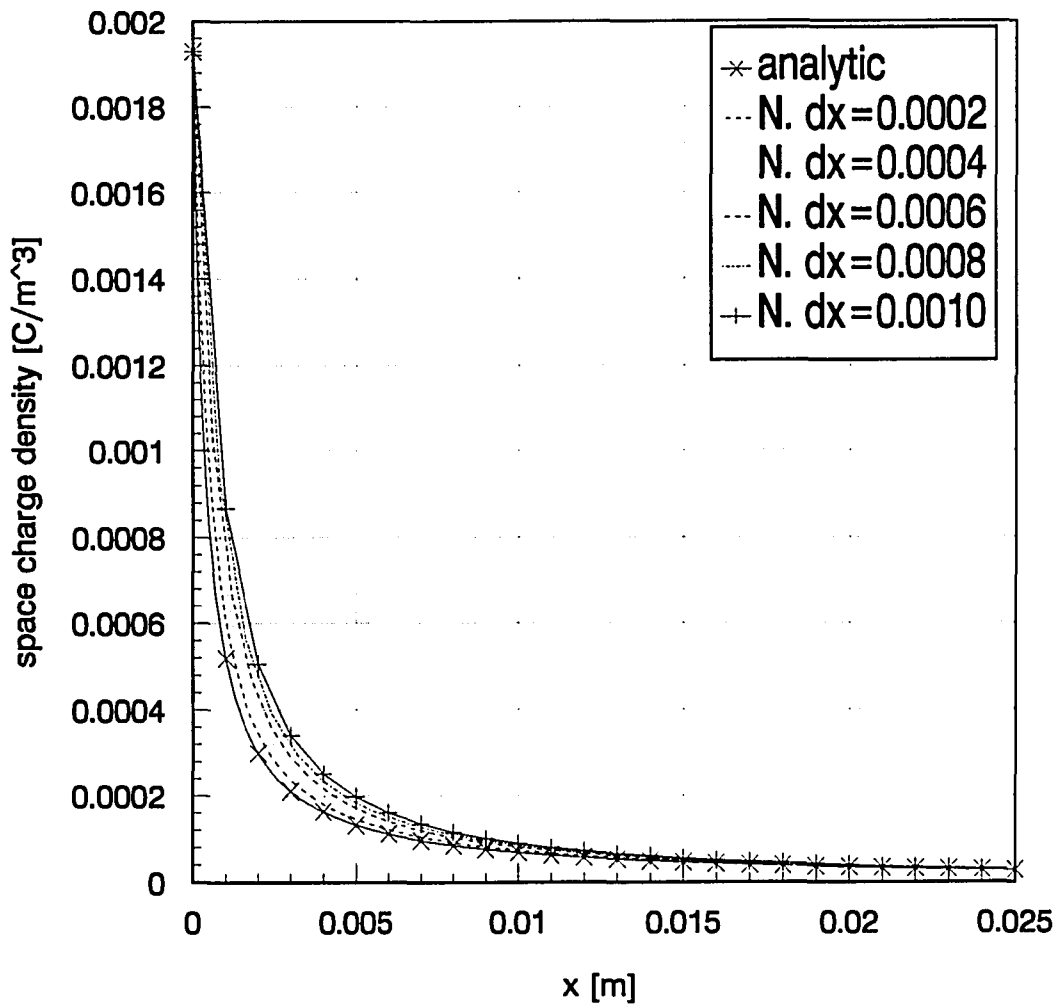


Figure 5.8: Numerical solution versus analytic solution of the charge density distribution at the interface between the two electrodes

domain is bounded by the flat plate surface. The corona wire is located at four gap lengths downstream of the leading edge of the flat plate. The stretching parameter used to cluster the grid in the vertical direction equals 1.055.

Figures 5.9 and 5.10 show the electric potential distributions at parallel levels located at different distances from the flat plate level. Comparing these two Figures shows the effect of the ion deposition to the surface between the two electrodes in creating a non-linear potential distribution while the distribution is linear for the non-ion deposition case. The ion deposition to the surface affects the electric potential distribution on the surface and inside the domain as it is clear in these two figures. This change in the electric potential consequently affects the directions of the electric field lines and the electric charge density distribution. The non-ion deposition case is an artificial one while the ion deposition case is the natural one and will be considered during the evaluation of the corona effect on the drag reduction. Figures 5.11 and 5.12 show the vector plots of the electric field lines created due to the surface electric potential distribution. The vector plots describe the directions only and do not describe the electric field quantitatively because the vectors are normalized to its length. It is clear in these two figures that the electric field lines are symmetric in distribution as expected. The electric field lines are more parallel to the surface for the case of the ion deposition to the surface than those for the non-ion deposition condition.

Figures 5.13 and 5.14 show the electric charge density distribution in the region above the surface between the two electrodes at parallel levels located at different distances from the flat plate level. It is clear that the ion deposition to the surface has an impact on the distribution inside the domain. The corona wire is the only source of ions in the domain and consequently the electric current is a flow of positive ions traveling out of the positive electrode. Looking horizontally, at $y=0.0$ in the gas phase side, the charge density has its maximum value at the location of the corona wire and it decreases as the distance increases

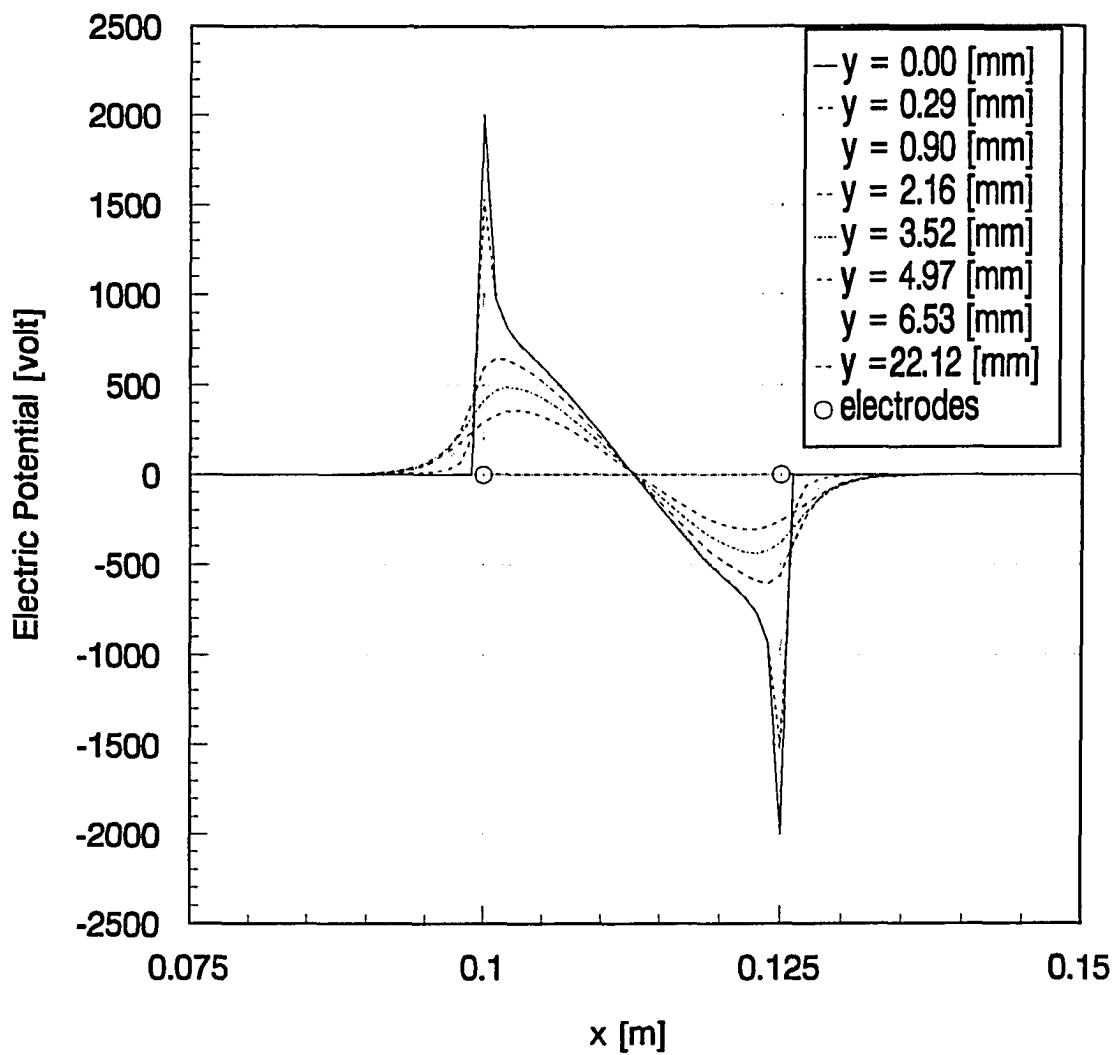


Figure 5.9: Electric potential distribution at different levels above the surface with ion deposition to surface ($U = 0.0$ m/sec, corona wire is upstream)

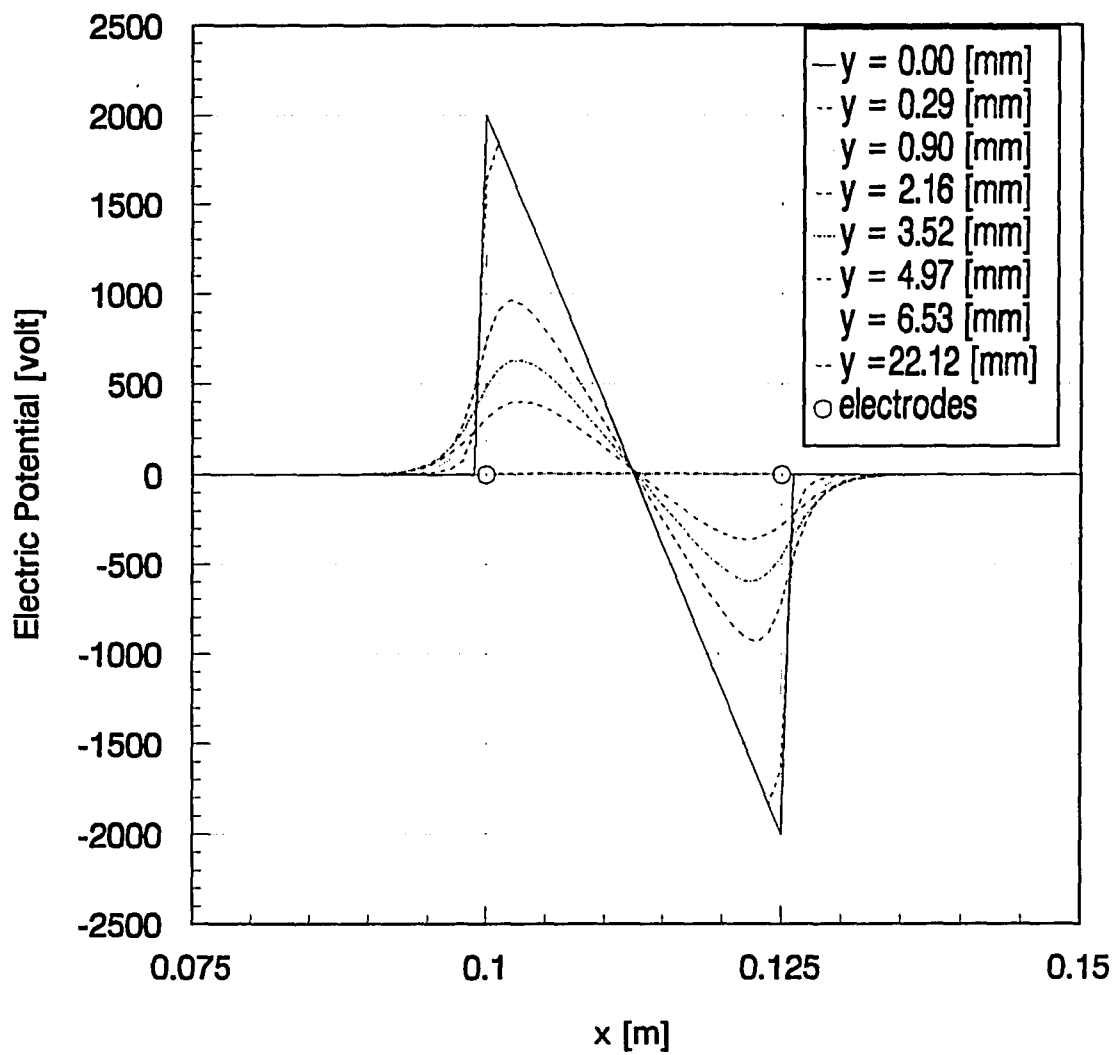


Figure 5.10: Electric potential distribution at different levels above the surface with no ion deposition to surface ($U = 0.0$ m/sec, corona wire is upstream)

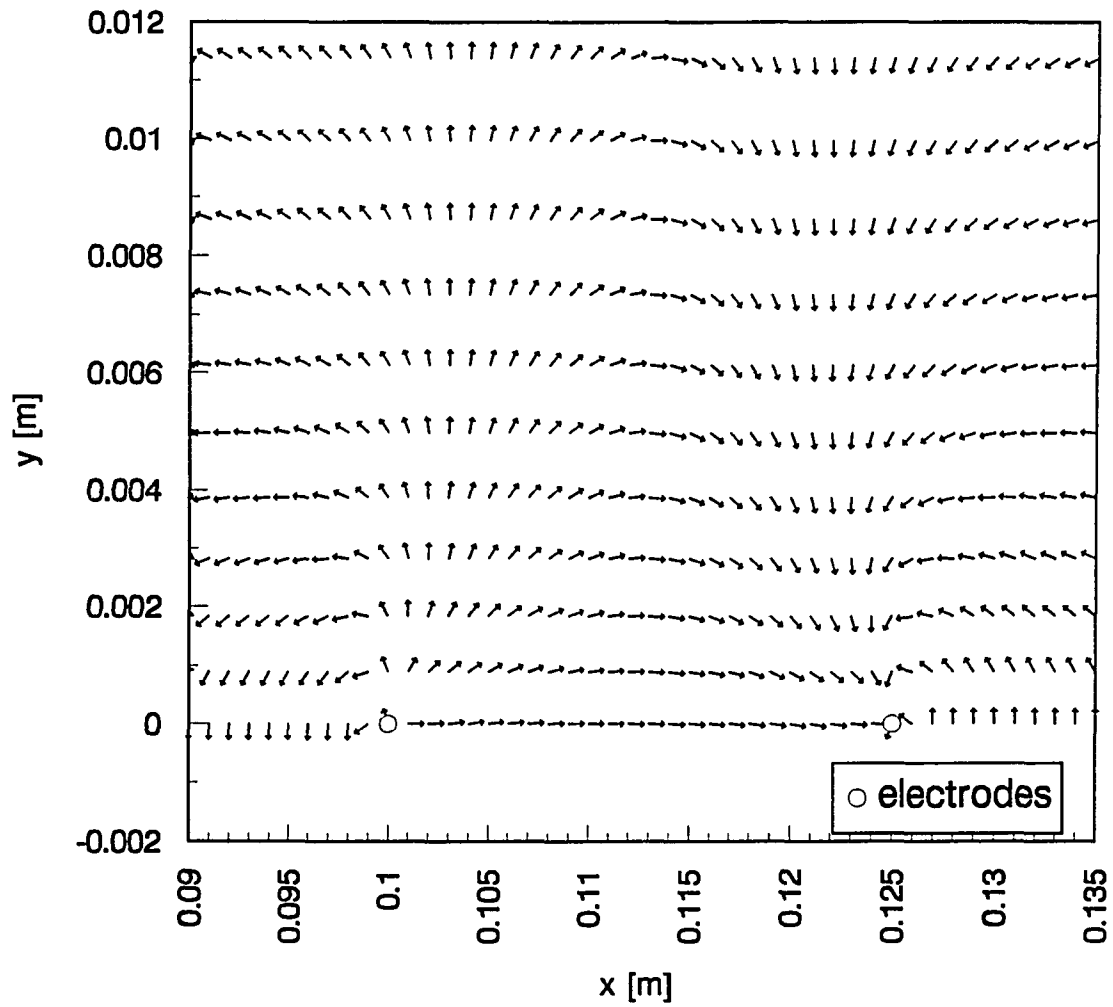


Figure 5.11: Vector plot of electric field strength at different levels above the surface with gas phase current and ion deposition to surface ($U = 0.0$ m/sec, corona wire is upstream)

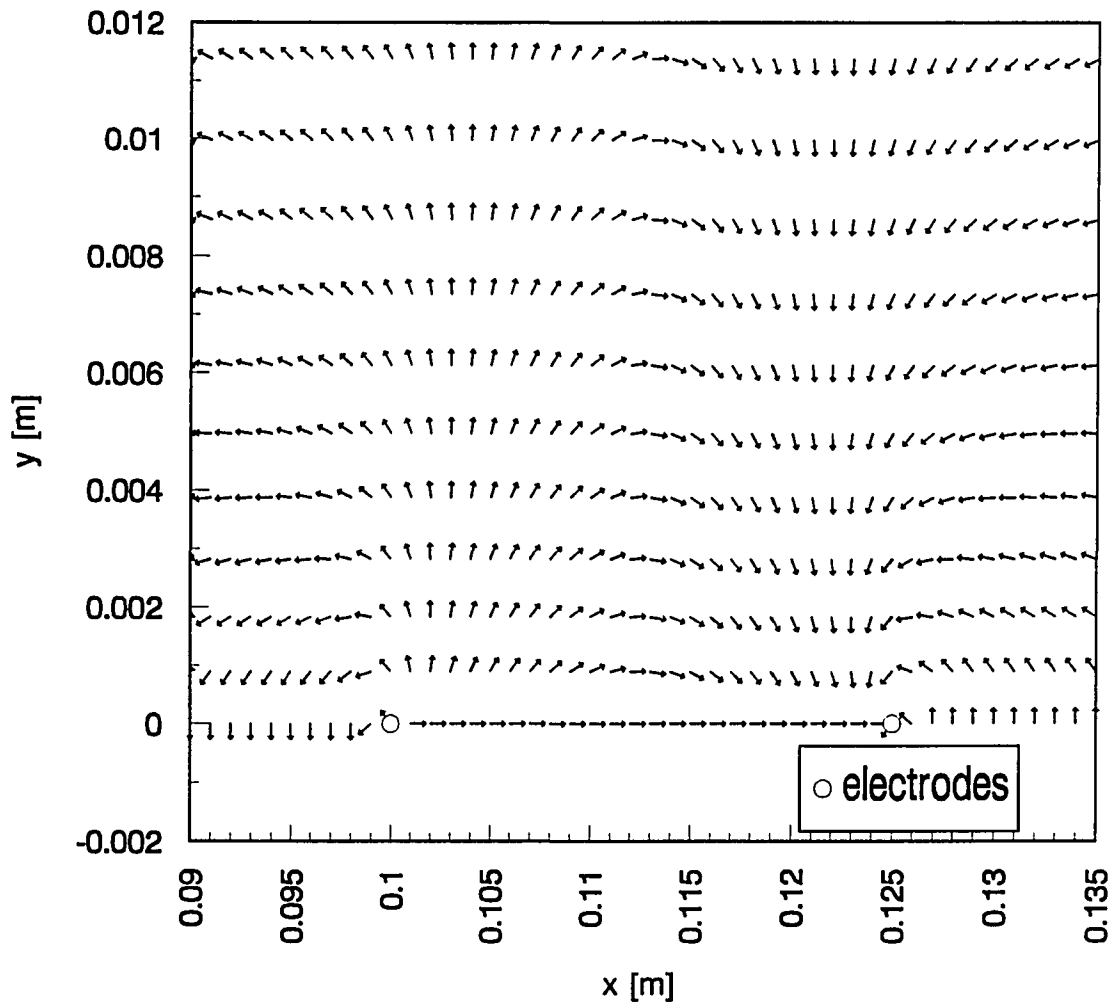


Figure 5.12: Vector plot of electric field strength at different levels above the surface with gas phase current and no ion deposition to surface ($U = 0.0$ m/sec, corona wire is upstream)

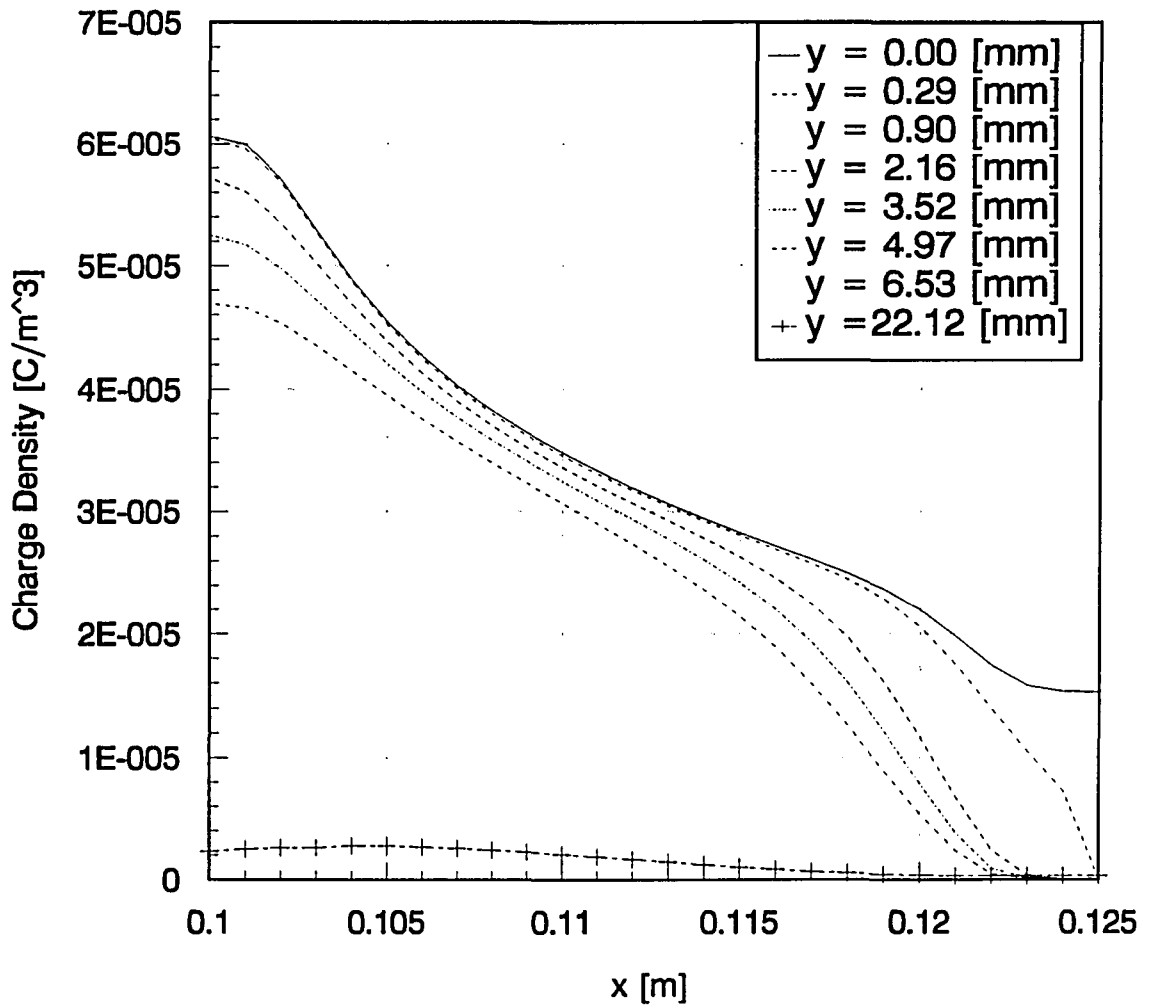


Figure 5.13: Charge density distribution at different levels above the surface between the two electrodes with ion deposition to surface ($U = 0.0$ m/sec, corona wire is upstream)

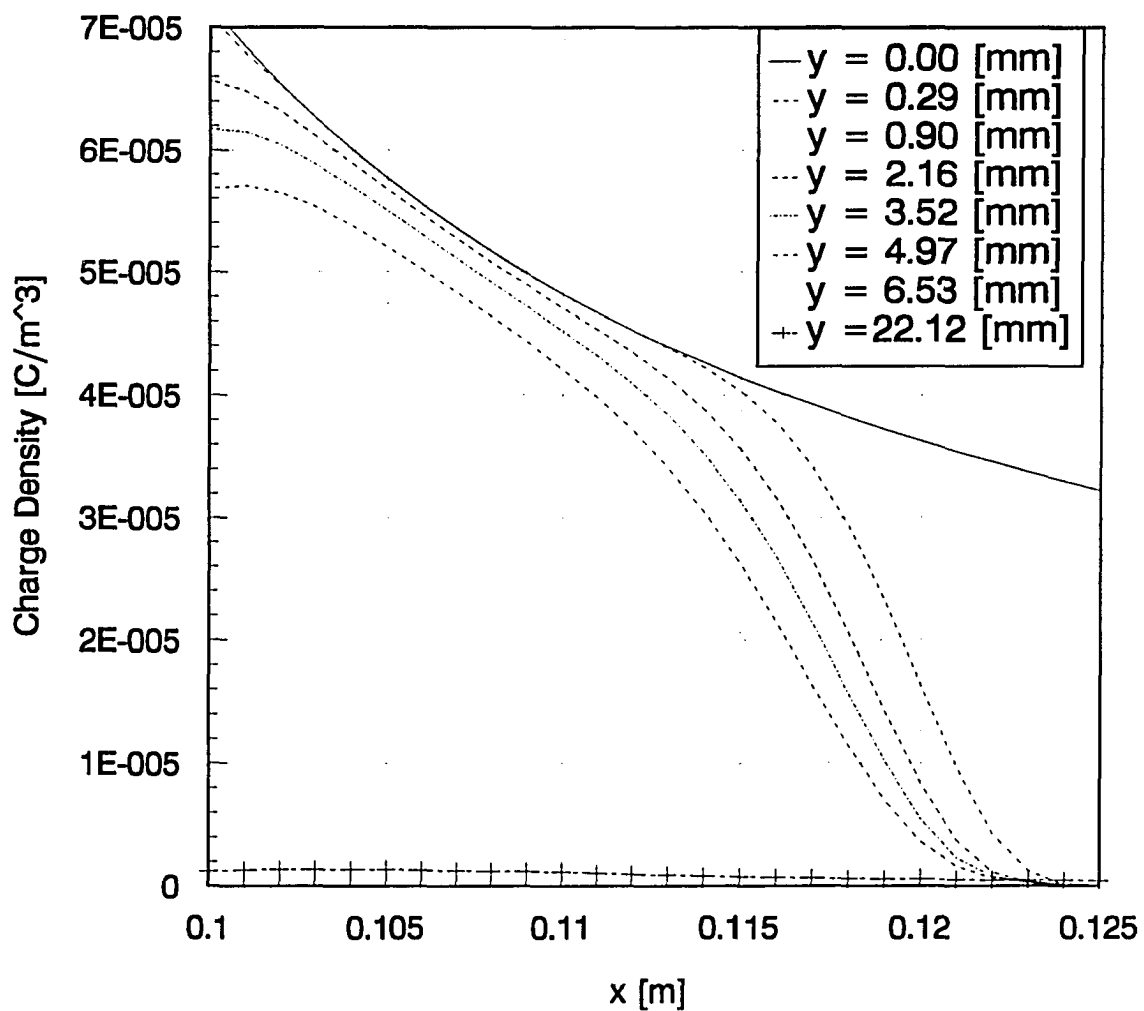


Figure 5.14: Charge density distribution at different levels above the surface between the two electrodes with no ion deposition to surface ($U = 0.0$ m/sec, corona wire is upstream)

from the corona wire towards the other electrode and this explains the spread out of the ions along the surface and vertically above the surface and some of these ions will go to infinity which makes the concentration of the ions decreases in that direction. Looking vertically, the charge density has its maximum value at $y=0.0$ in the gas phase side and as the height above the surface increases the charge density decreases and the decrease in the region near the electrodes is bigger than that in the middle between the two electrodes. Checking the current conservation around the corona wire shows that the current is conserved. The current crossing several control surfaces (5 grid points in y -direction and a number of grid points in x -direction) around that electrode is counted and compared to the predicted corona current. Figure 5.15 shows that within acceptable limits. There are two sources for the tolerance; the first is that the counted current will pass if its value is within $\pm 2\%$ of the predicted corona current and the second is the machine round off error specially that we are dealing with small numbers. Finally Figures 5.16 and 5.17 show the normalized vector plots of the of the current density in the region between the two electrodes. The vector plots of the current density are similar to the vector plots of the electric field lines because actually the current is following the electric field direction.

5.1.4.2 Study case 2

This is the practical case which will be used during the evaluation of the corona discharge on the drag reduction. The corona wire is maintained at 4000 *volts* and the other electrode is grounded. The whole surface between and outside the two electrodes is assumed to be of finite conductivity. The two electrodes are assumed to have a circular cross section of 2 μm diameter. The gap between the two electrodes is 25 *mm*. The computational domain has a height of 12 gap lengths and a width of 20 gap lengths. The bottom side of the computational domain is bounded by the flat plate surface and its extension in the air

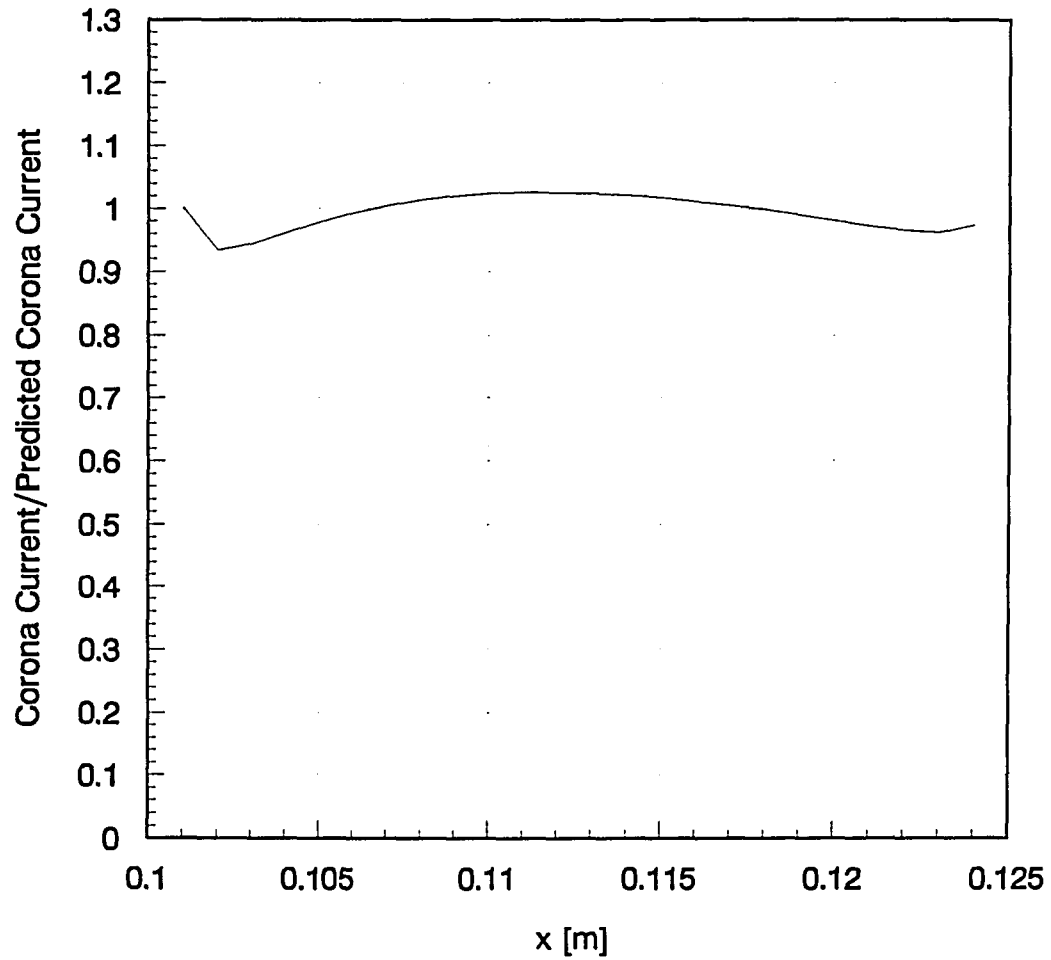


Figure 5.15: Corona current to predicted corona current ratio across control surfaces around the corona wire between the two electrodes with ion deposition to surface ($U = 0.0$ m/sec, corona wire is upstream)

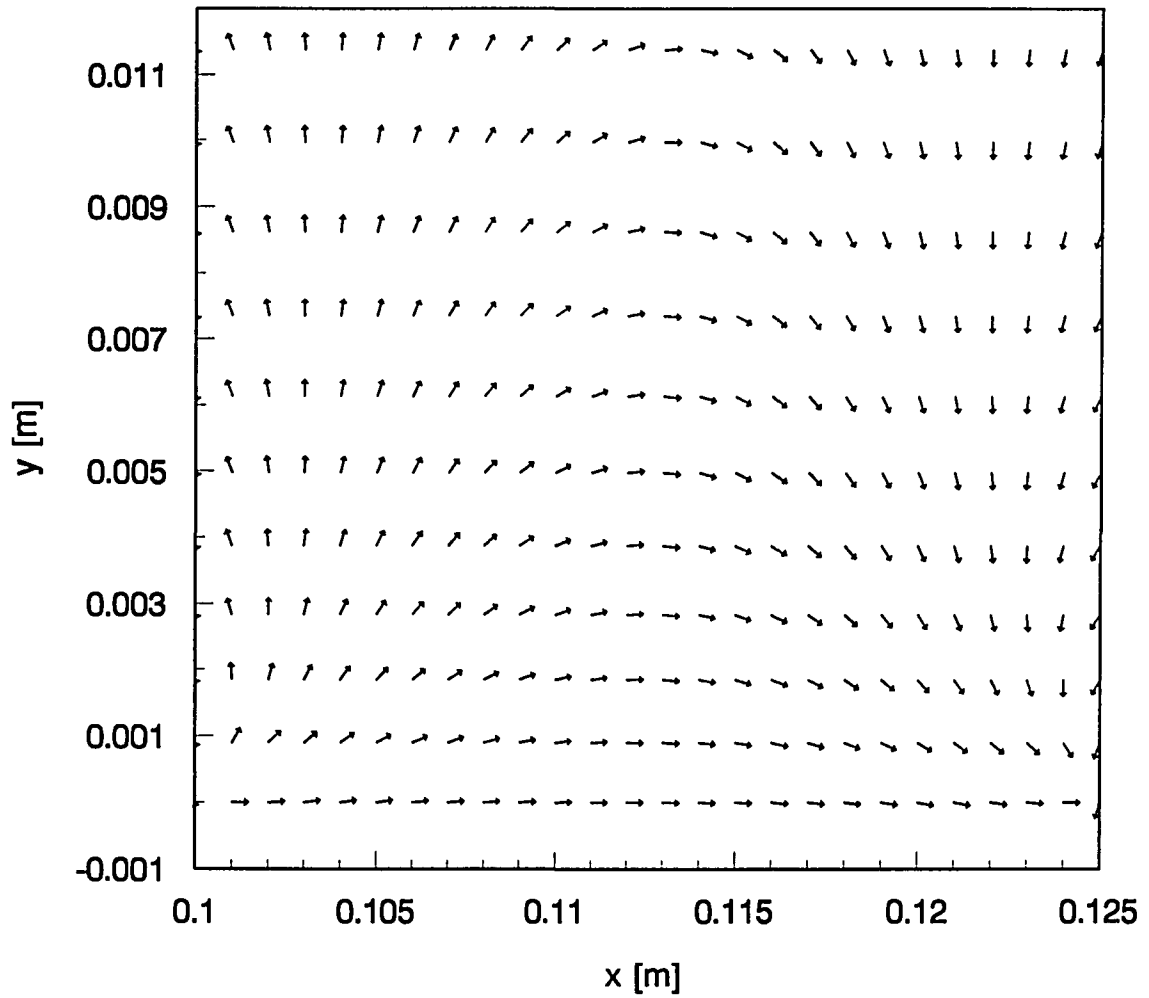


Figure 5.16: Vector plot of current density at different levels above the surface between electrodes with ion deposition to surface ($U = 0.0$ m/sec, corona wire is upstream)

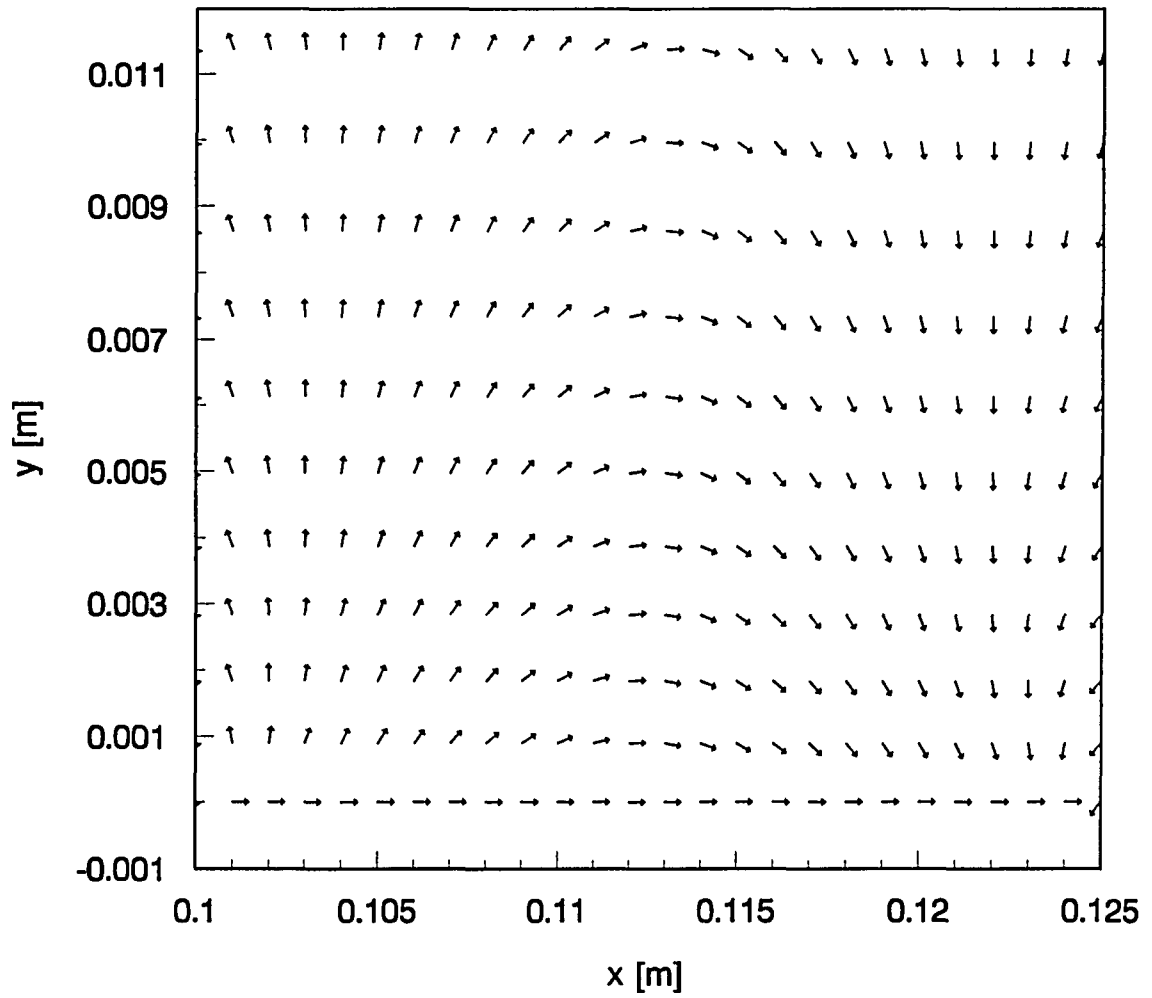


Figure 5.17: Vector plot of current density at different levels above the surface between electrodes with no ion deposition to surface ($U = 0.0$ m/sec, corona wire is upstream)

along the negative direction of the x-axis. The corona wire is located at one gap length downstream the leading edge of the flat plate.

Figures 5.18 and 5.20 show the electric potential distributions at parallel levels located at different distances from the flat plate level for the whole width of the computational domain while Figures 5.19 and 5.21 show the potential at the same levels in the region between the two electrodes. Again the comparison between these figures shows the effect of the ion deposition to the surface in the region between the two electrodes in creating a non-linear potential distribution in this region specially near the electrodes while the distribution is linear for the non-ion deposition case. Because of the finite conductivity of the plate surface outside the two electrodes the electric potential in these two regions will be of constant value which equal the value of the electric potential of the closest electrode. The consideration of the unchanging potential in these two regions is based on the negligibility of the effect of the very little number of ions that may reach and deposit to the surface in these two regions. The electric potential distribution in the upstream of the plate leading edge along the negative direction of the x-axis is governed by equation (3.7.3.1) where the potential is proportional to the square root of the distance from the plate leading edge. As in study case 1 the ion deposition to the surface affects the electric potential distribution on the surface and inside the domain and consequently the directions of the electric field lines and the electric charge density distribution. Figures 5.22 and 5.23 show the vector plots of the electric field lines created due to the surface electric potential distribution. As mentioned in study case 1 the vector plots are normalized and describe only the directions and not the magnitudes of the electric field vectors. It is clear in these two figures that the electric field lines are more parallel to the surface for the case of the ion deposition than those for the non-ion deposition condition and this will help in adding the momentum in the horizontal direction very close to the surface inside the boundary layer

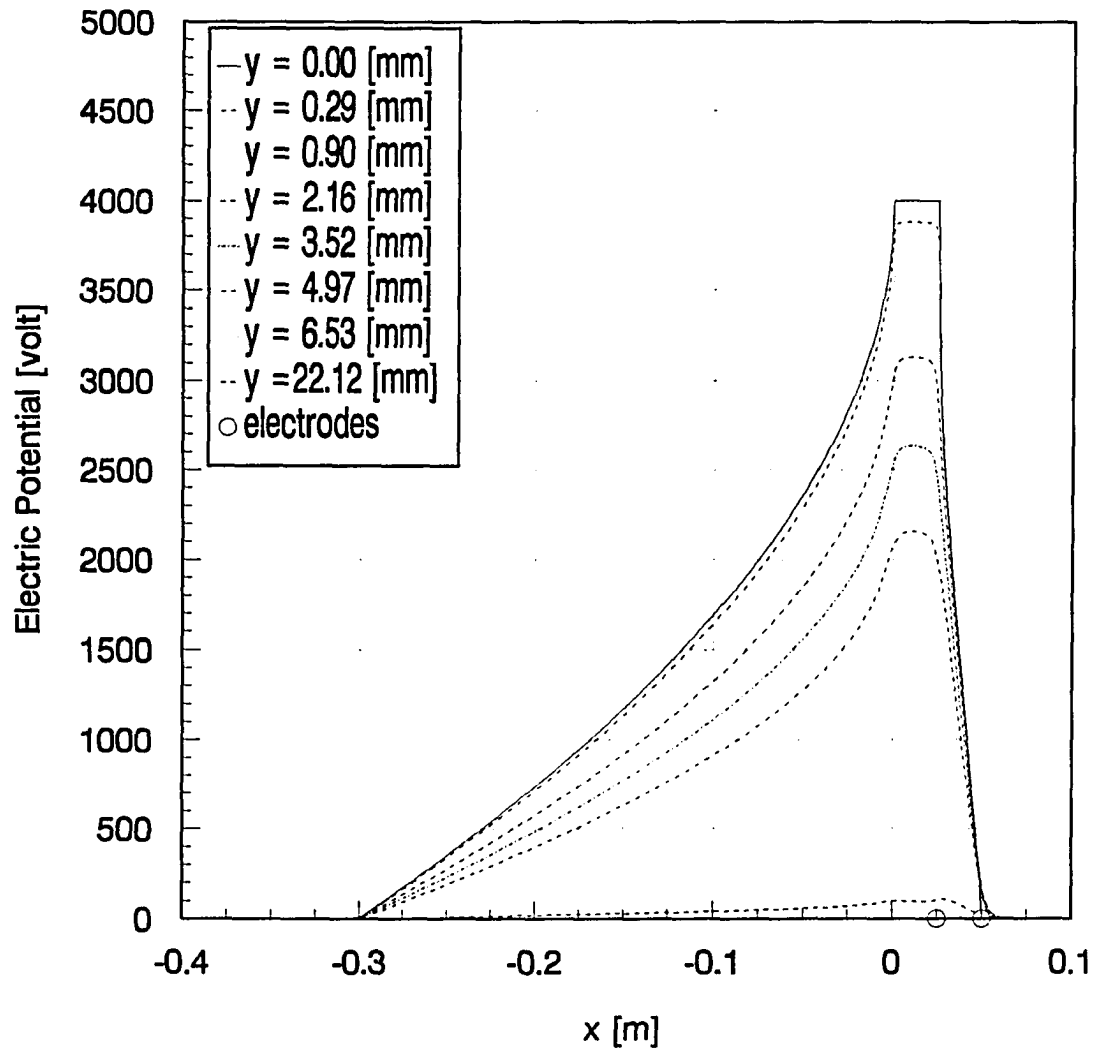


Figure 5.18: Electric potential distribution at different levels above the surface with ion deposition to surface ($U = 0.0$ m/sec, corona wire is upstream)

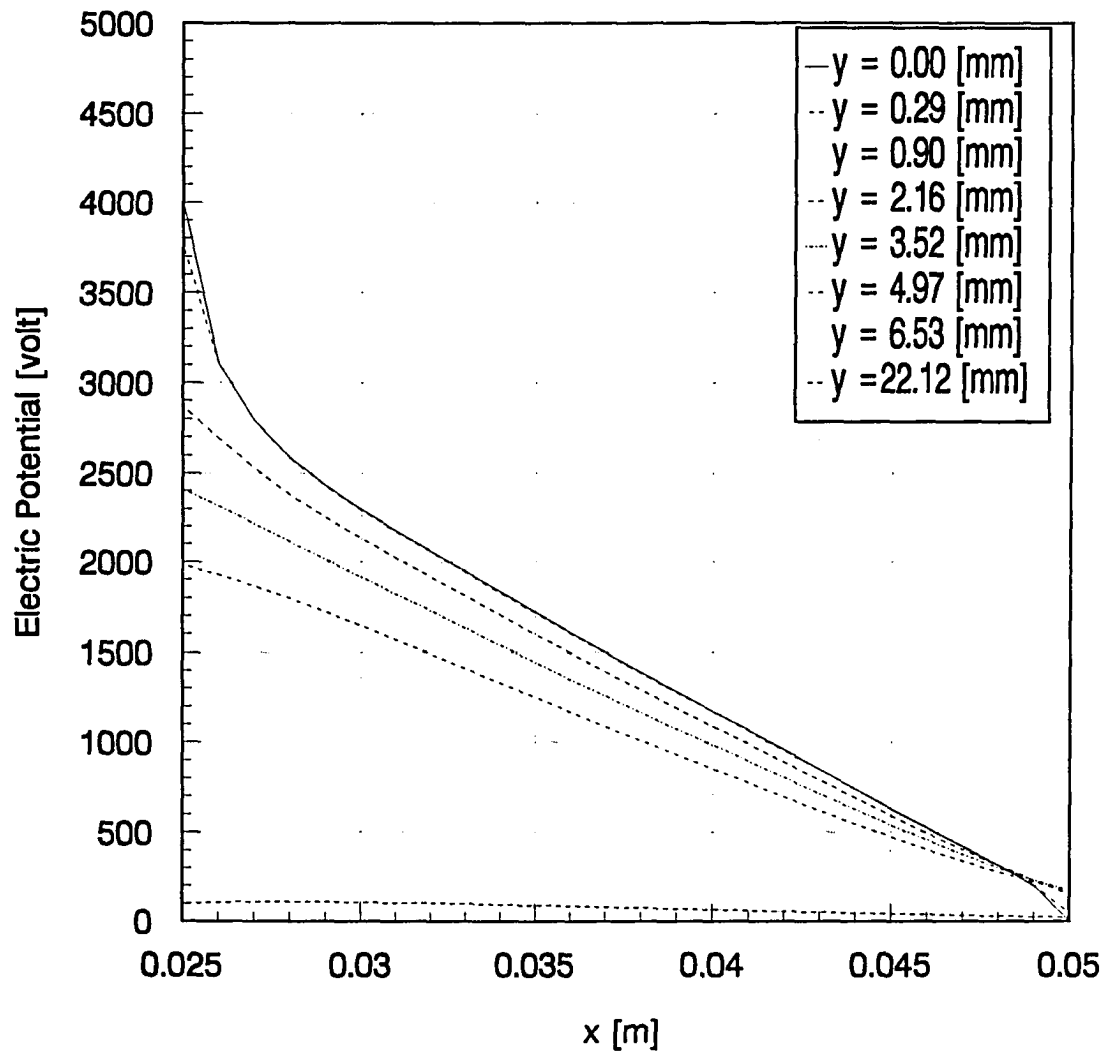


Figure 5.19: Electric potential distribution at different levels above the surface between electrodes with ion deposition to surface ($U = 0.0$ m/sec, corona wire is upstream)

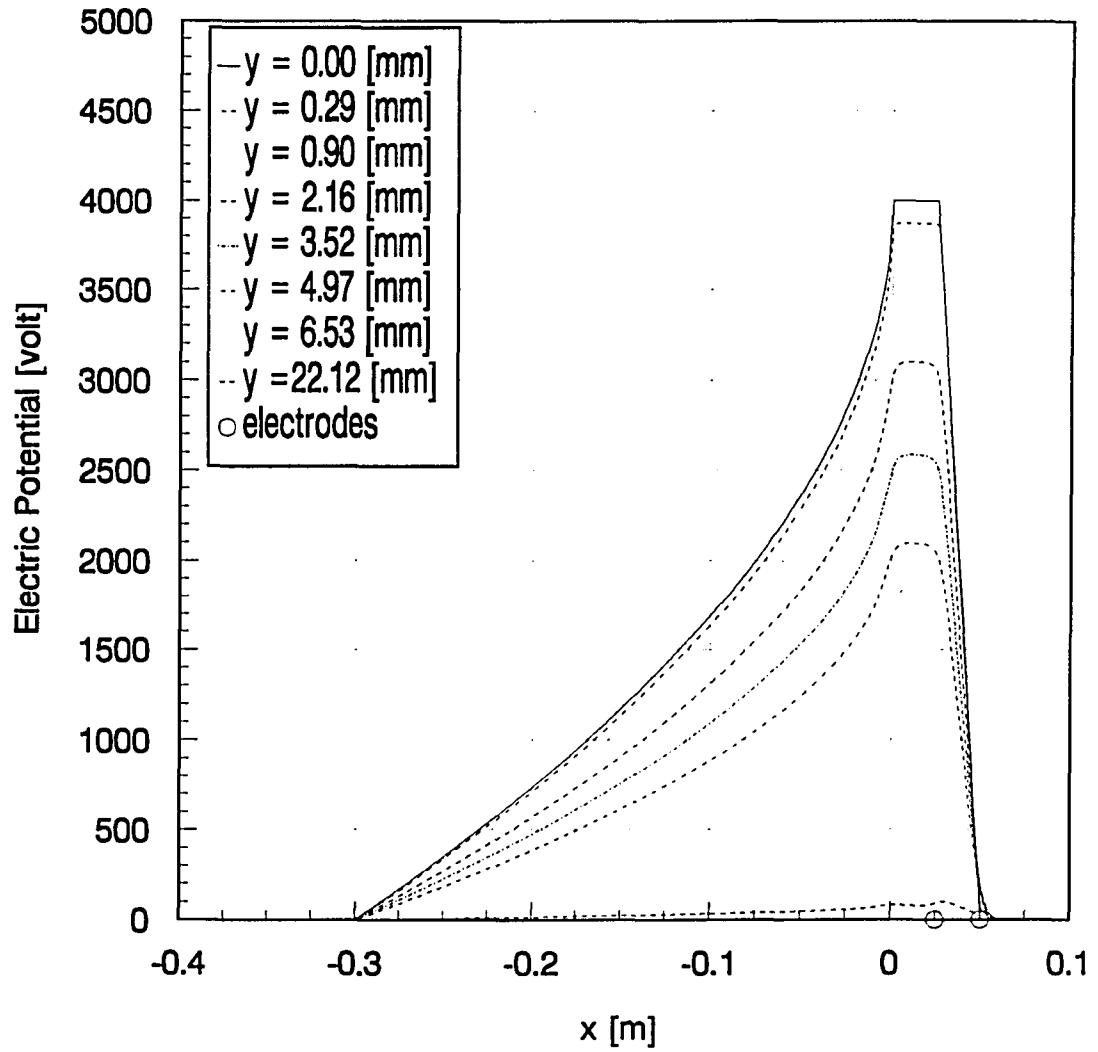


Figure 5.20: Electric potential distribution at different levels above the surface with no ion deposition to surface ($U = 0.0$ m/sec, corona wire is upstream)

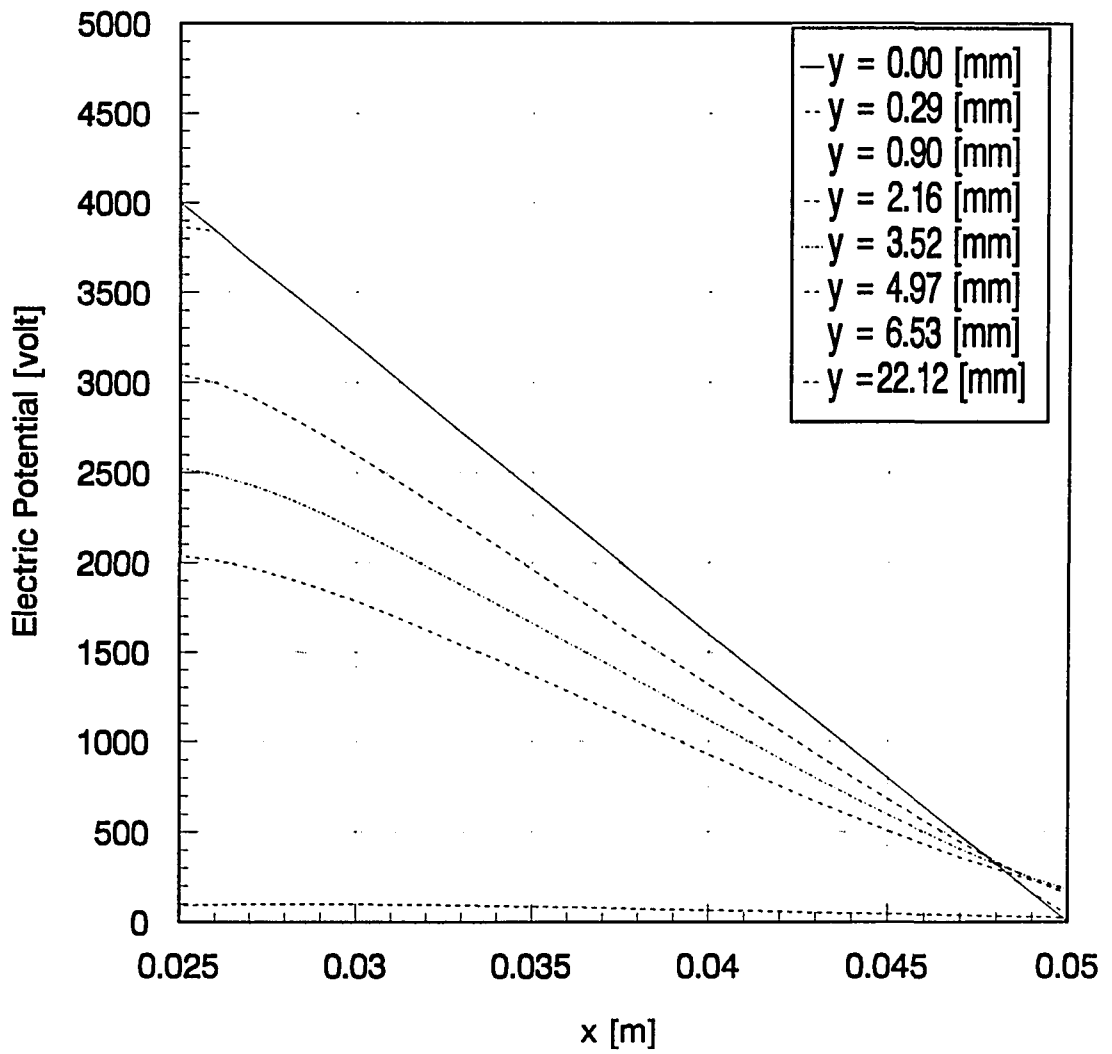


Figure 5.21: Electric potential distribution at different levels above the surface between electrodes with no ion deposition to surface ($U = 0.0$ m/sec, corona wire is upstream)

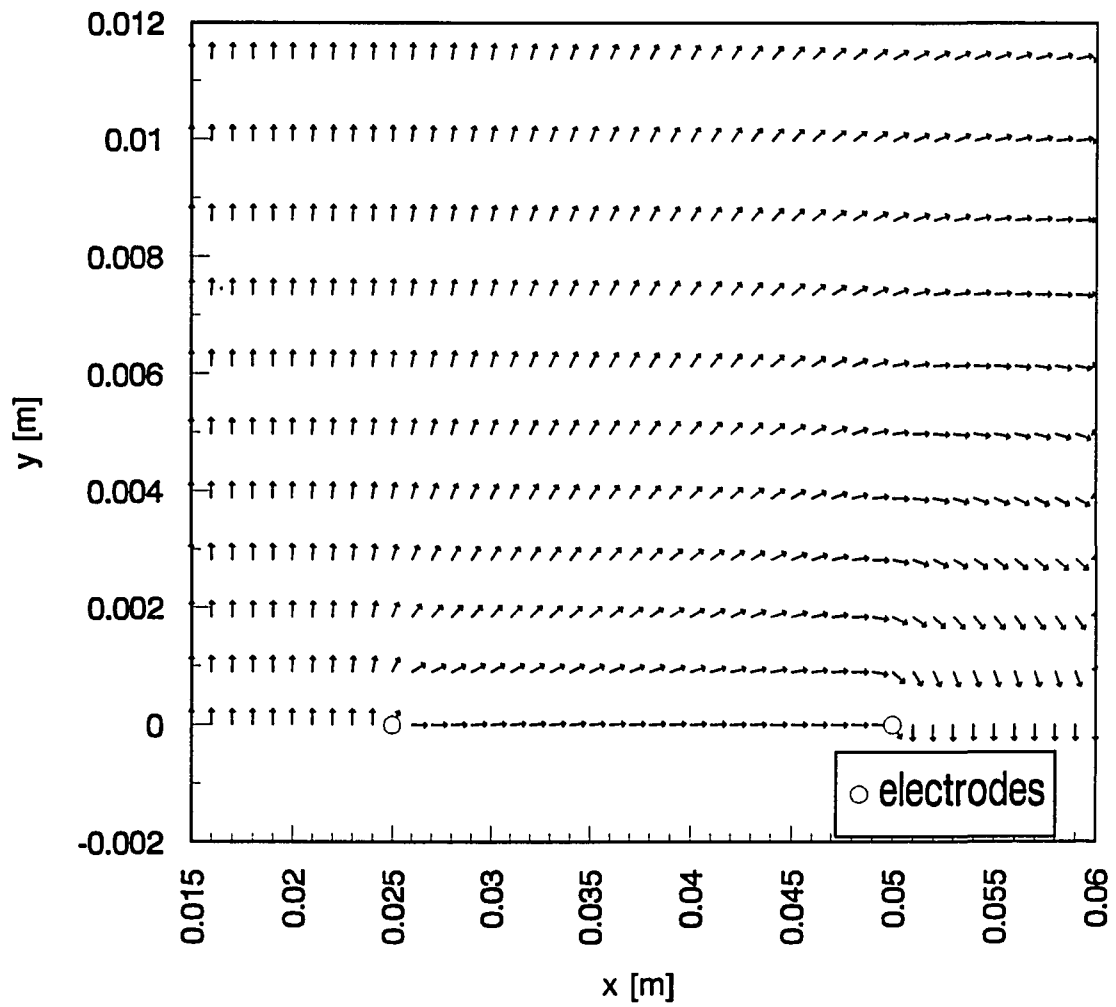


Figure 5.22: Vector plot of electric field strength at different levels above the surface with gas phase current and ion deposition to surface ($U = 0.0$ m/sec, corona wire is upstream)

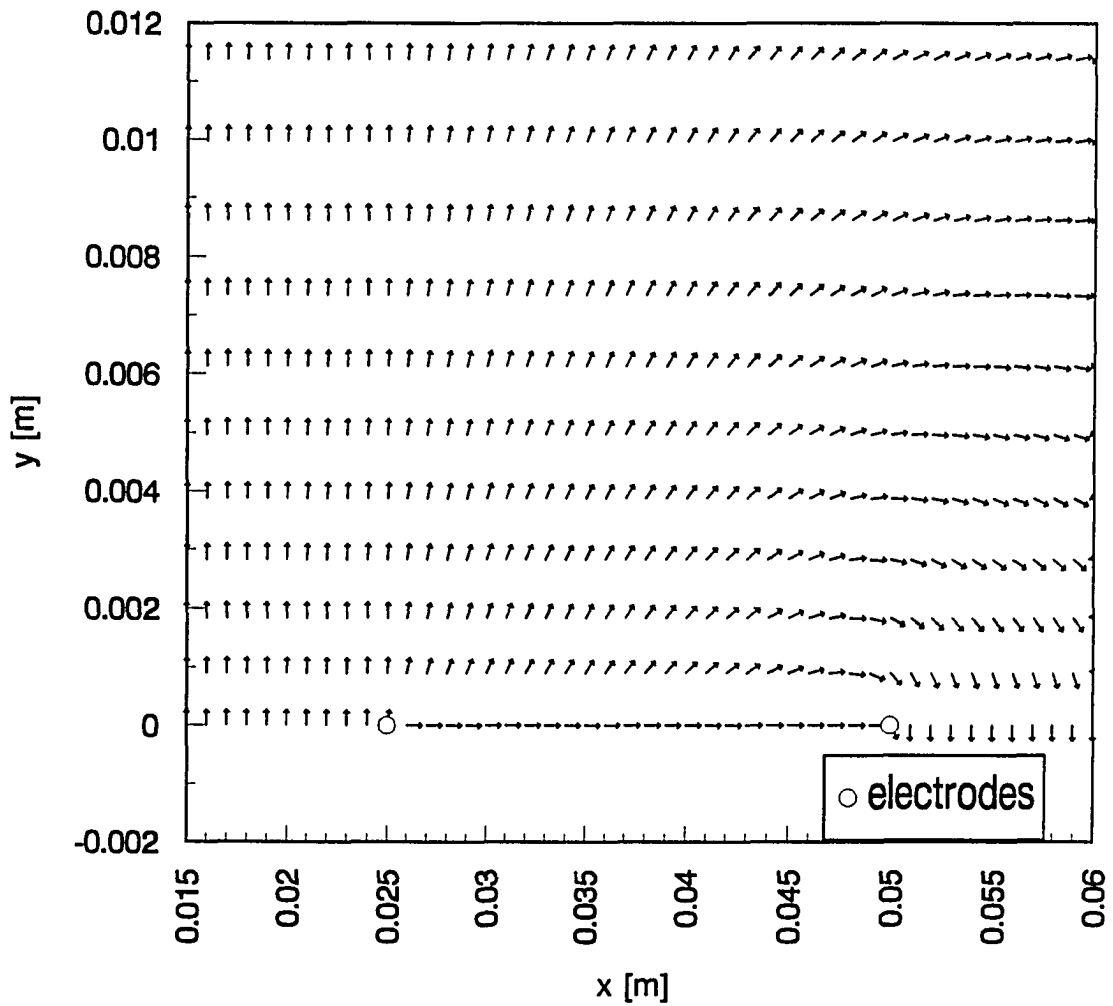


Figure 5.23: Vector plot of electric field strength at different levels above the surface with gas phase current and no ion deposition to surface ($U = 0.0$ m/sec, corona wire is upstream)

where the viscous effect is strong. The comparison of the electric field vector plots of both study cases shows a big difference in their distributions and consequently in the directions of the body force. In other words the electric field distribution is a matter of the shape of the boundary conditions and not only the potential difference between the two electrodes.

Figures 5.24 and 5.25 show the electric charge density distribution in the region above the surface between the two electrodes at parallel different levels above the flat plate surface. It is clear that the ion deposition to the surface has an impact on the distribution inside the domain. As described in study case 1 the charge density distribution follow the same trend here except that the general shape of the distribution in both cases is not exactly the same. The current is conserved within acceptable limits as shown in Figure 5.26 and explained in study case 1. Finally figures 5.27 and 5.28 show the normalized vector plots of the of the current density in the region between the two electrodes.

5.2 Corona Effect on Boundary-Layer

In order to show the details of the corona effect on boundary-layer the model described in study case 2 is used with free stream velocity of 3.0 m/sec and the electrodes are assumed to be set in such a way to create an ionic wind along the direction of the fluid flow. The running conditions and the output results of this run are shown in Table 5.1. The drag force per unit width acting on the plate portion between the two electrodes is calculated twice with and without the corona effect; first based on the momentum deficit at the locations of the electrodes and second based on the shear stress on the plate surface between the electrodes. Although the corona effect increases the velocity gradient on the surface as shown in Figures 5.29 and 5.30 that leads to an increase in the surface shear stress and consequently the drag force based on that shear, it adds momentum to the fluid flow which resists the viscous effect and reduces the momentum deficit and consequently reduces the

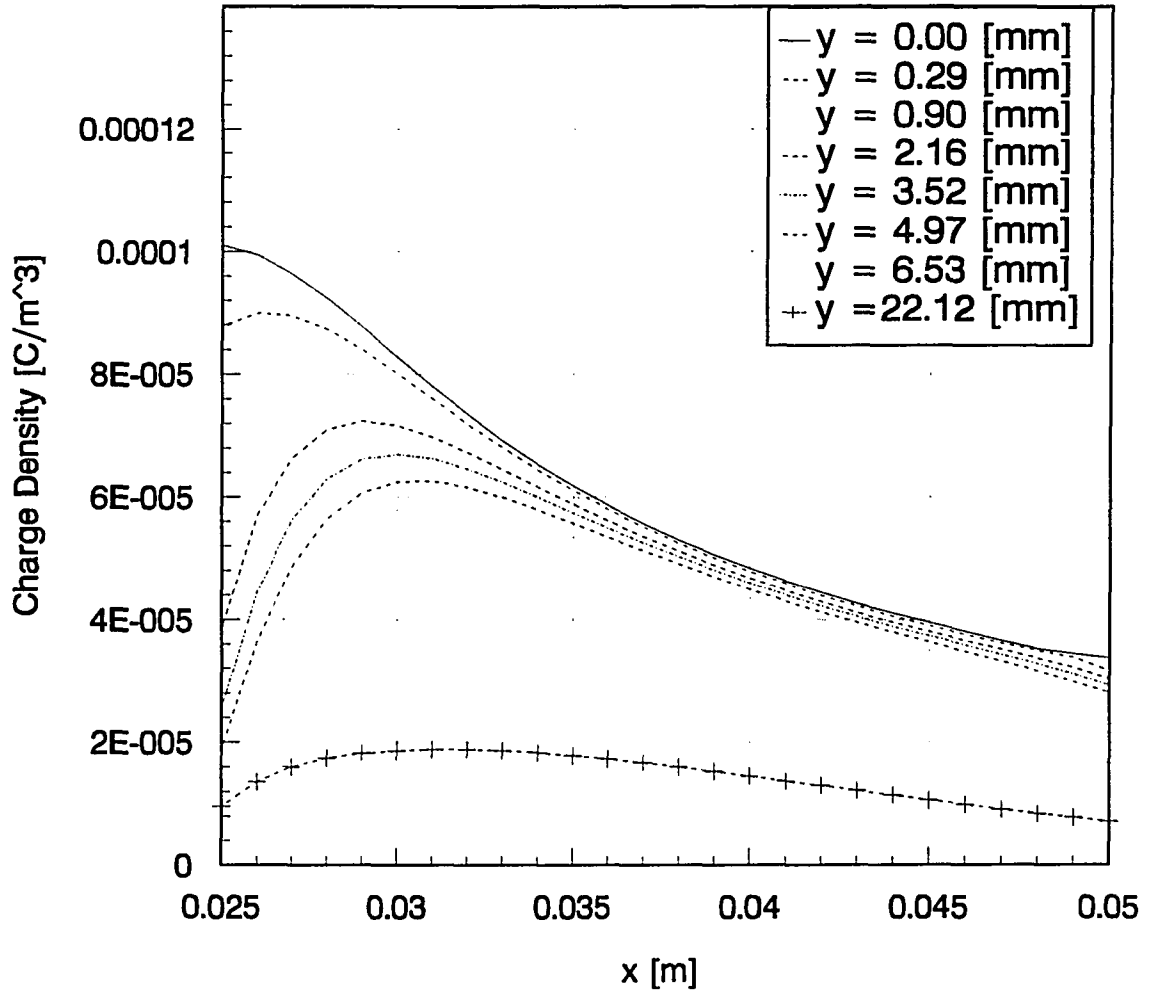


Figure 5.24: Charge density distribution at different levels above the surface between the two electrodes with ion deposition to surface ($U = 0.0$ m/sec, corona wire is upstream)

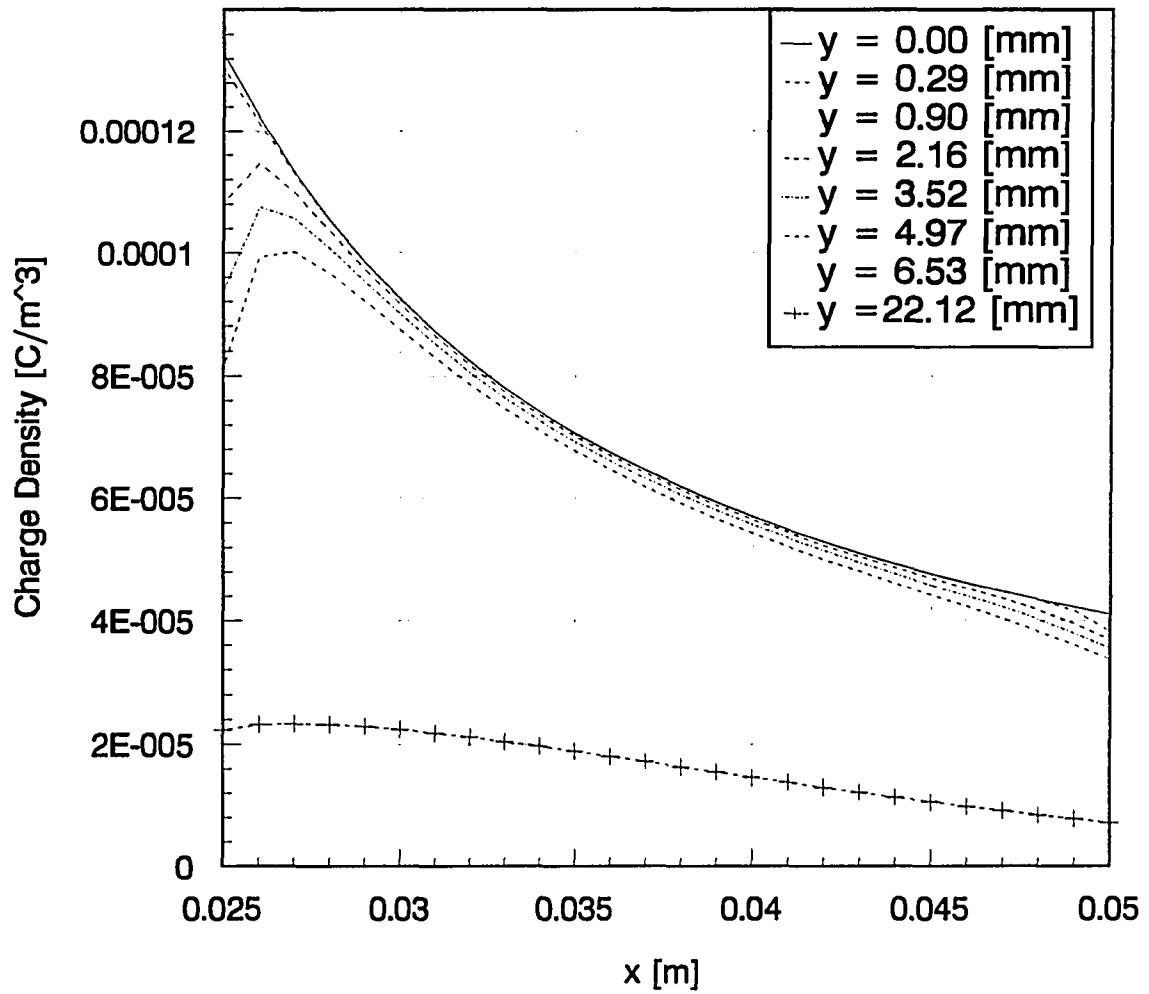


Figure 5.25: Charge density distribution at different levels above the surface between the two electrodes with no ion deposition to surface ($U = 0.0$ m/sec, corona wire is upstream)

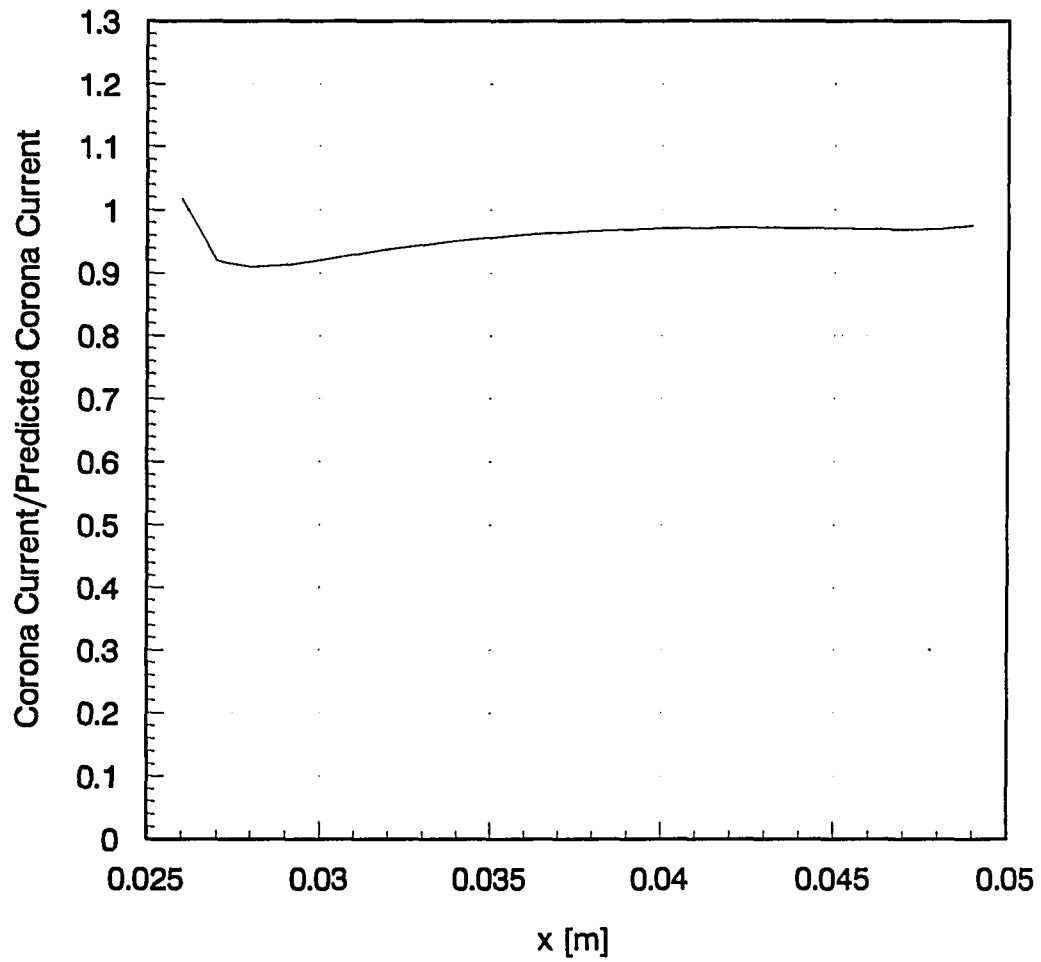


Figure 5.26: Corona current to predicted corona current ratio across control surfaces around the corona wire between the two electrodes with ion deposition to surface ($U = 0.0$ m/sec, corona wire is upstream)

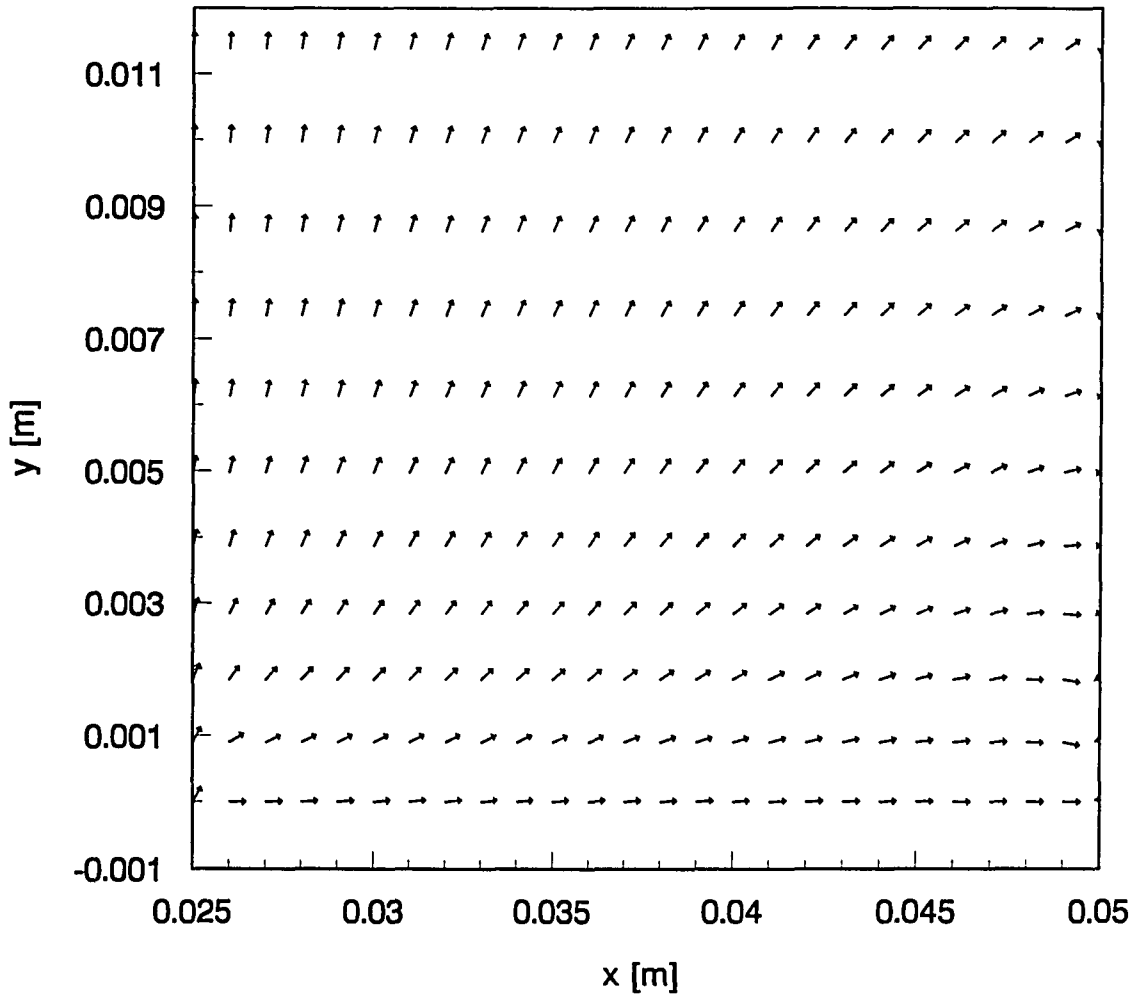


Figure 5.27: Vector plot of current density at different levels above the surface between electrodes with ion deposition to surface ($U = 0.0$ m/sec, corona wire is upstream)

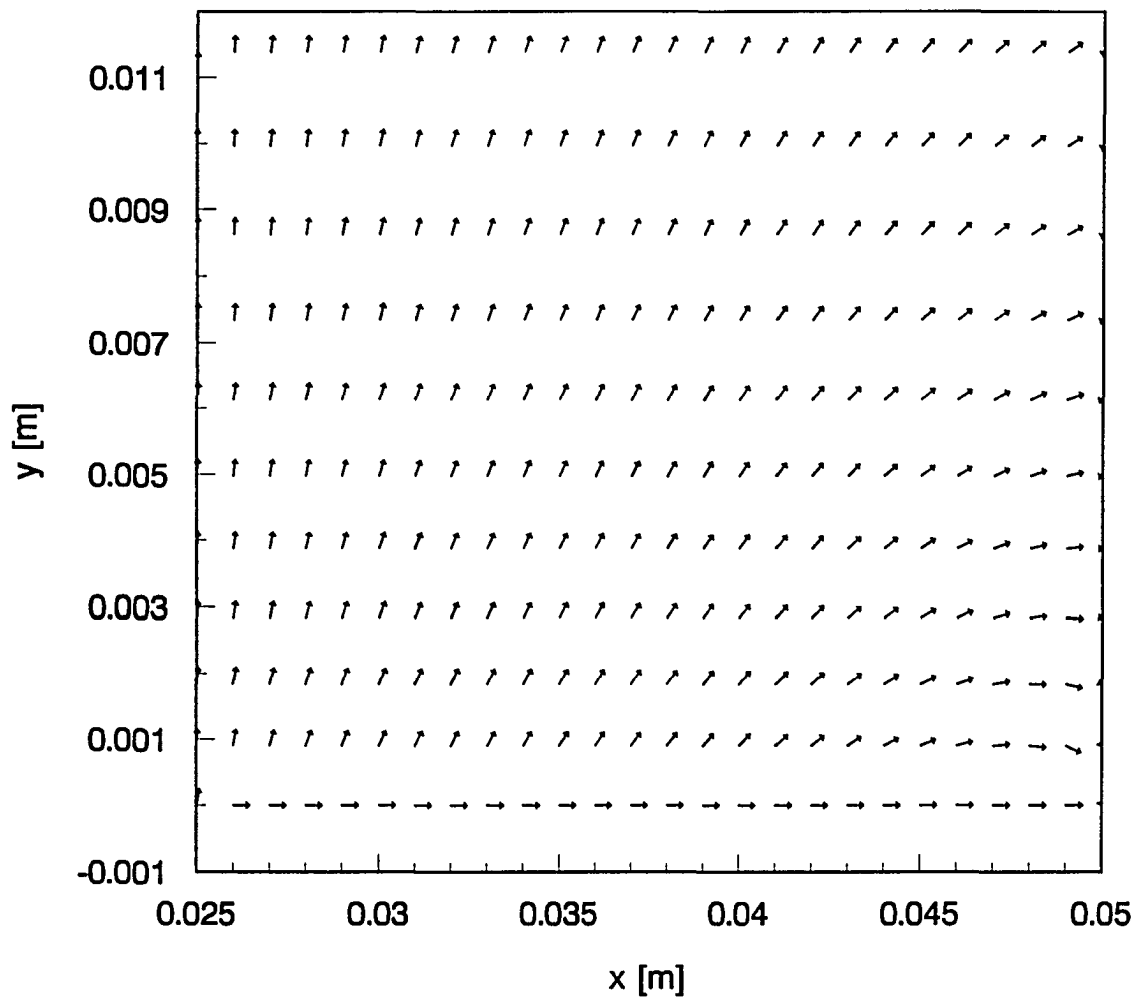


Figure 5.28: Vector plot of current density at different levels above the surface between electrodes with no ion deposition to surface ($U = 0.0$ m/sec, corona wire is upstream)

Table 5.1: Output results for study case 2 with $U = 3.0$ m/sec

free stream velocity	3.00 m/sec
gap length between electrodes	25.00 mm
Reynolds number based on gap length	5068
distance between plate leading edge and upstream electrode	25.00 mm
downstream distance from leading edge where B. L. eqs. are valid	4.93 mm
total length of computation domain	500.00 mm
number of grid points in x-direction	501
computational domain height	300.00 mm
boundary layer stretching parameter	1.005
number of grid points in y-direction (boundary layer grid)	200
electrostatic stretching parameter	1.055
number of grid points in y-direction (electrostatic grid)	200
corona wire diameter	2.00 micrometers
corona onset voltage	680.27 volts
polarity order of electrodes	positive electrode upstream
electric potential between electrodes	4000.00 volts
predicted corona current	1.106e-05 Amp/m
initial guess of charge density at corona wire	2.383e-04 C/m ³
final value of charge density at corona wire	1.010e-04 C/m ³
boundary layer thickness at location of upstream electrode	2.1 mm
no. of grid points dividing B. L. at location of upstream electrode	30
boundary layer thickness at location of downstream electrode	2.8 mm
no. of grid points dividing B. L. at location of upstream electrode	36
drag force (mom.) acting on plate between electrodes without corona	0.0037 N
drag force (mom.) acting on plate between electrodes with corona	0.0012 N
percentage drag reduction	68.59%
drag force (shear) acting on plate between electrodes without corona	0.0010 N
drag force (shear) acting on plate between electrodes with corona	0.0011 N

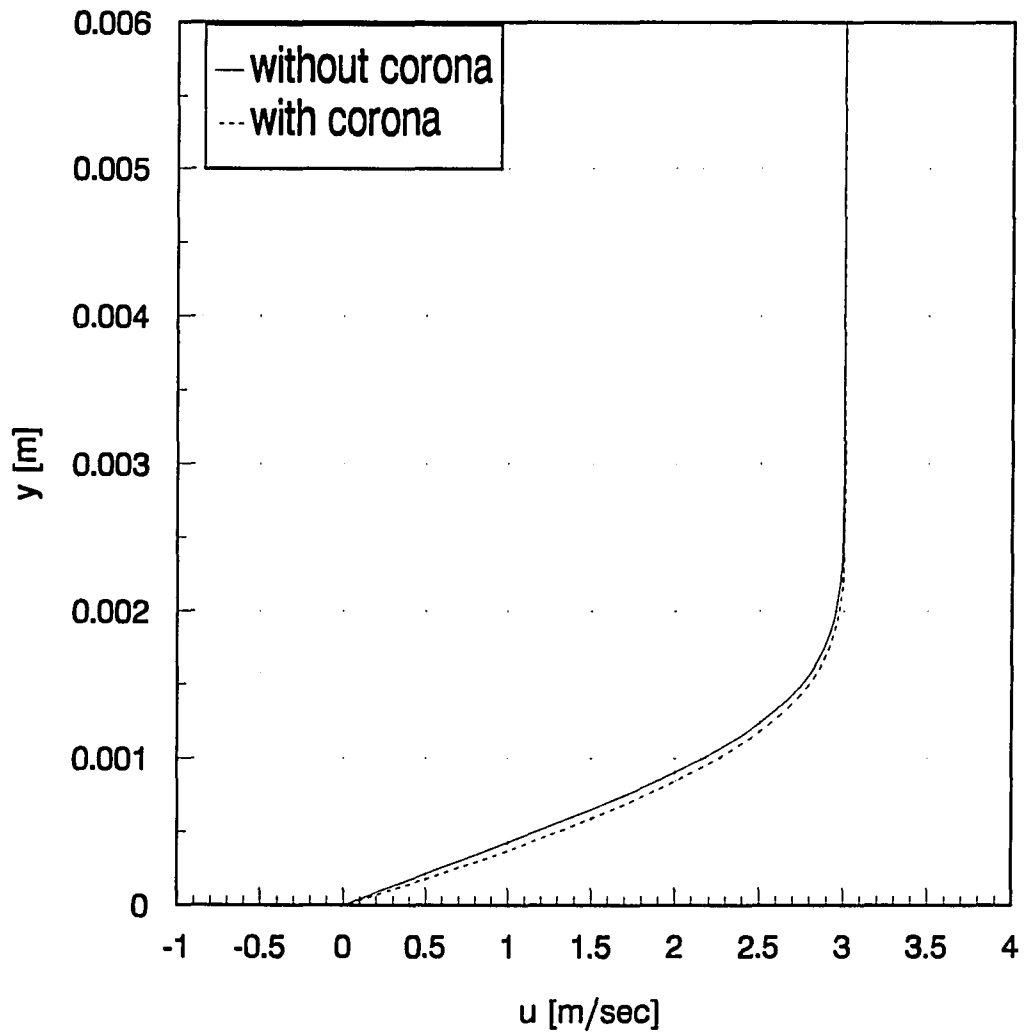


Figure 5.29: Velocity profiles without and with corona effect with ion deposition to surface at 3.0 mm downstream of the corona wire (U=3 m/sec, corona wire is upstream)

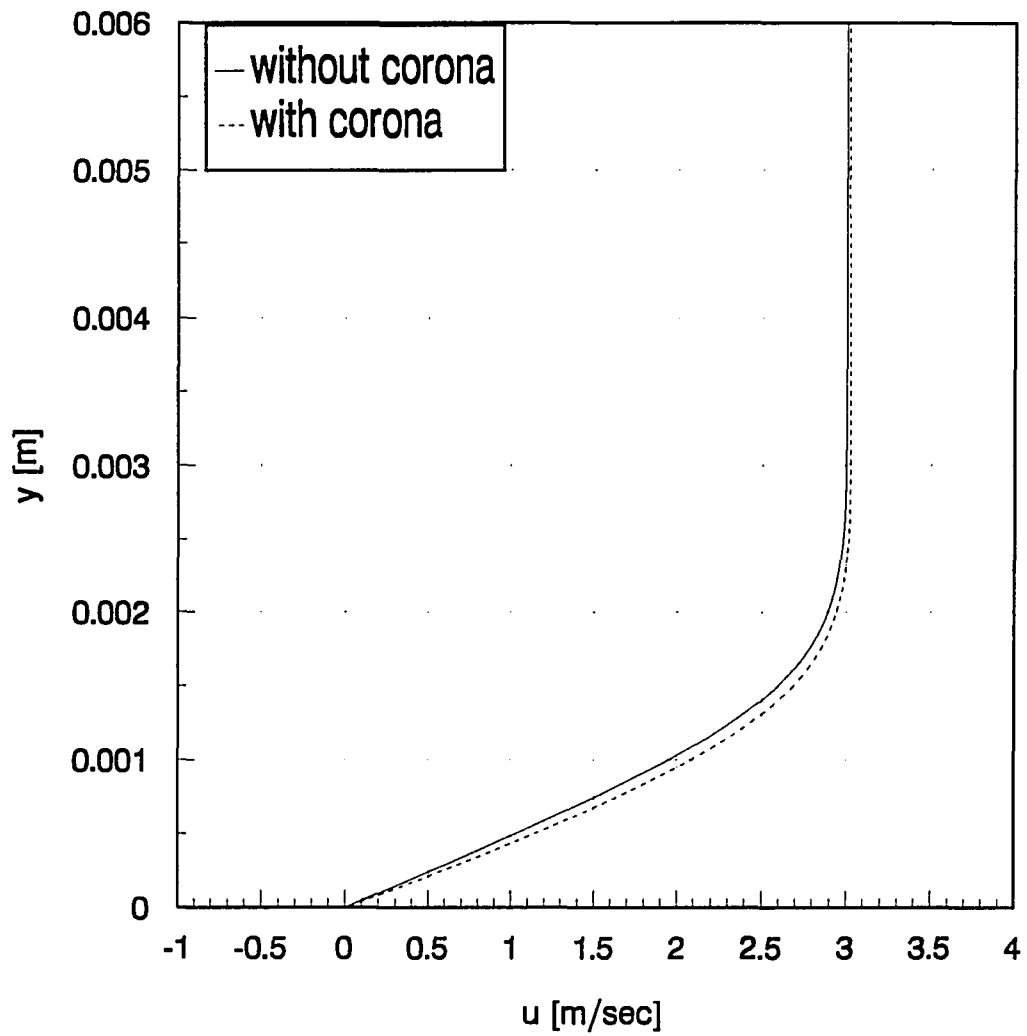


Figure 5.30: Velocity profiles without and with corona effect with ion deposition to surface at 13.0 mm downstream of the corona wire (U=3 m/sec, corona wire is upstream)

drag force on that region by an equivalent amount to the momentum increase. Figure 5.31 clarifies the momentum increase due to the corona effect by showing the velocity profiles at the location of the two electrodes with and without this effect while Figure 5.32 shows the increase in the local shear stress due to corona effect. Also Figure 5.33 shows the variation in the local skin friction coefficient with and without the corona effect which supports the same interpretation. The traveling positive ions between the electrodes transfer its momentum to the neutral particles of the fluid and at the same time act on the corona wire by a force against the drag direction due to the repelling action between these positive ions and this positive electrode. The momentum gained by the fluid equals the acting force on the electrode and the drag will be reduced by a similar amount.

If the polarity of the two electrodes is reversed in such a way that the ionic wind moves against the flow direction, the corona effect will reduce the velocity gradient on the surface, increase the fluid momentum deficit, and the force due to the repelling action will act along the drag direction. This analysis tells us that the corona discharge is more beneficial if it is applied in such a way that the ionic wind and the fluid flow are moving in the same direction because it reduces the drag acting on the plate while it increases the velocity gradient on the surface which is the required control to delay the flow separation on the plate.

Figure 5.34 shows the progress of the boundary-layer thickness with and without the corona effect. At the location of the corona wire where the corona effect starts the boundary-layer is thinned due to the added momentum which increases the fluid velocity inside the boundary-layer. This increase in velocity is accompanied by reduction in boundary-layer thickness to keep the same mass flow rate inside the boundary-layer. Table 5.2 presents the details of the boundary-layer thickness for one stretching parameter ($\beta = 1.005$) and various free stream velocities. The steps shown in the boundary-layer thickness profiles are due to the

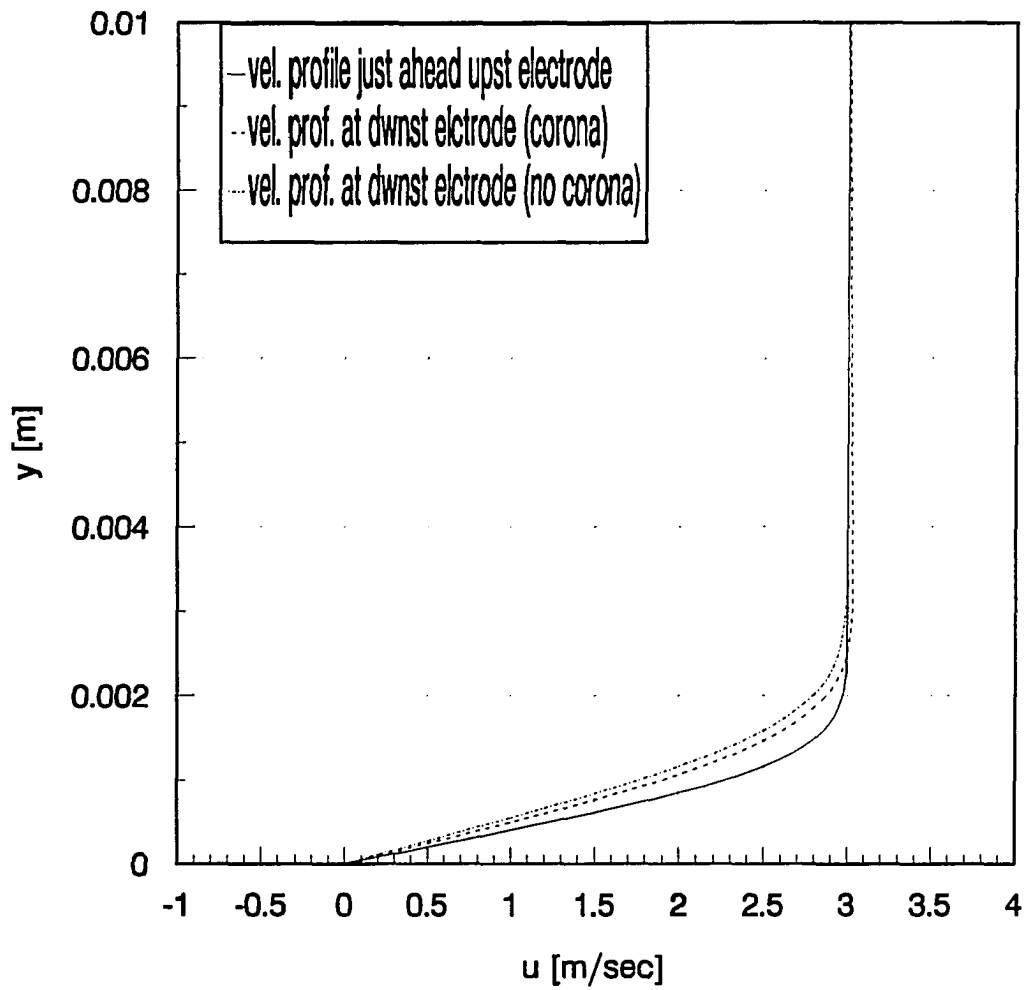


Figure 5.31: Velocity profiles without and with corona effect with ion deposition to surface at the edges of the corona strip ($U=3$ m/sec, corona wire is upstream)

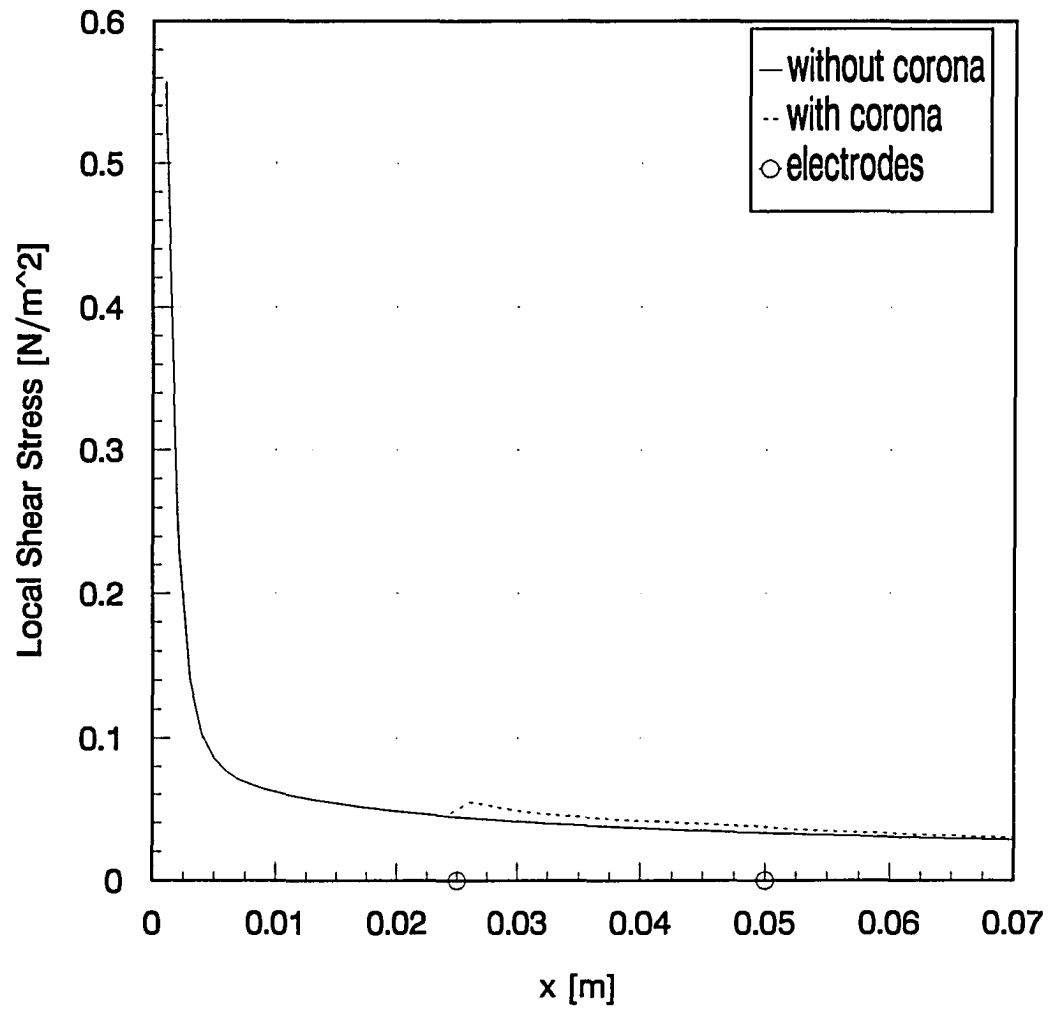


Figure 5.32: Local shear stress without and with corona effect with ion deposition to surface ($U=3$ m/sec, corona wire is upstream)

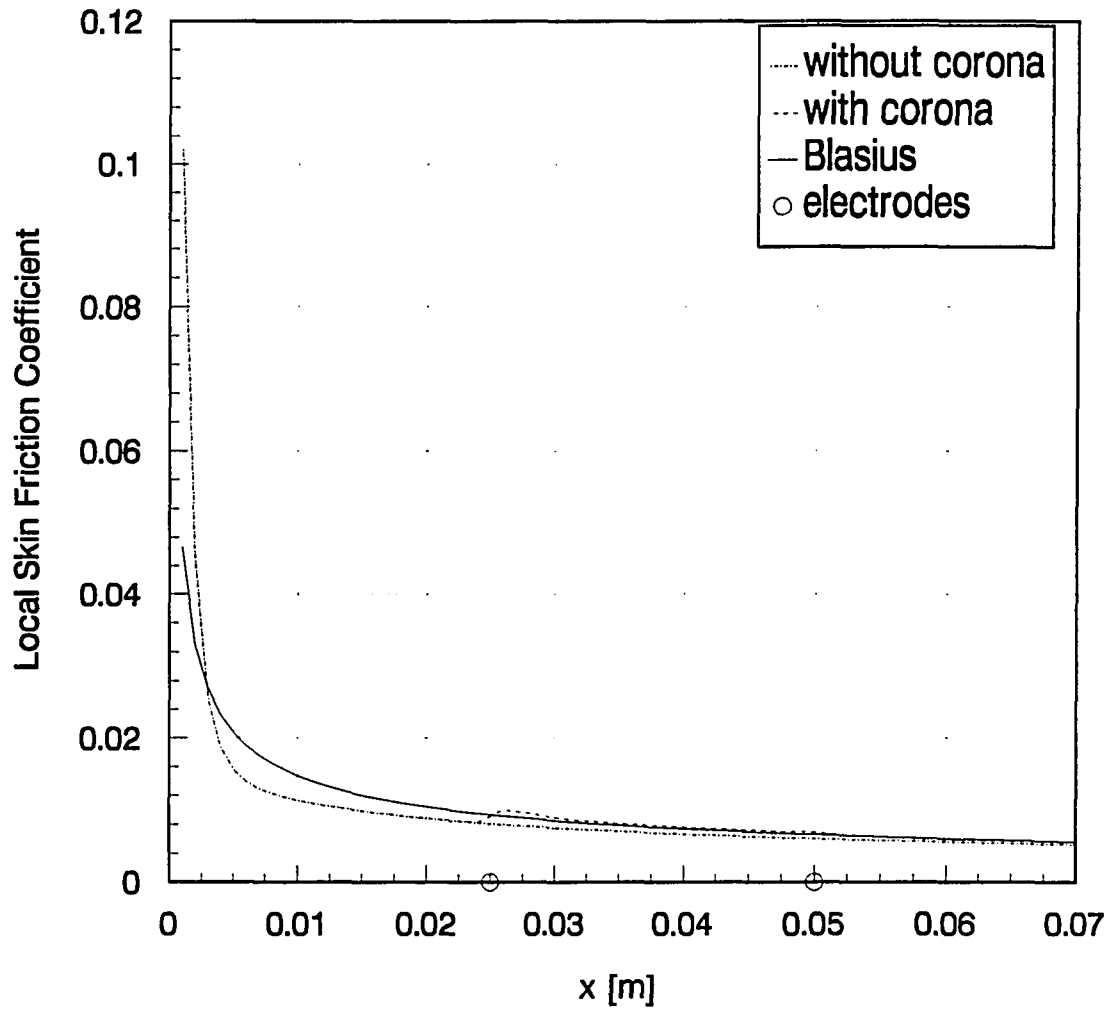


Figure 5.33: Local skin friction coefficient without and with corona effect with ion deposition to surface ($U=3$ m/sec, corona wire is upstream)

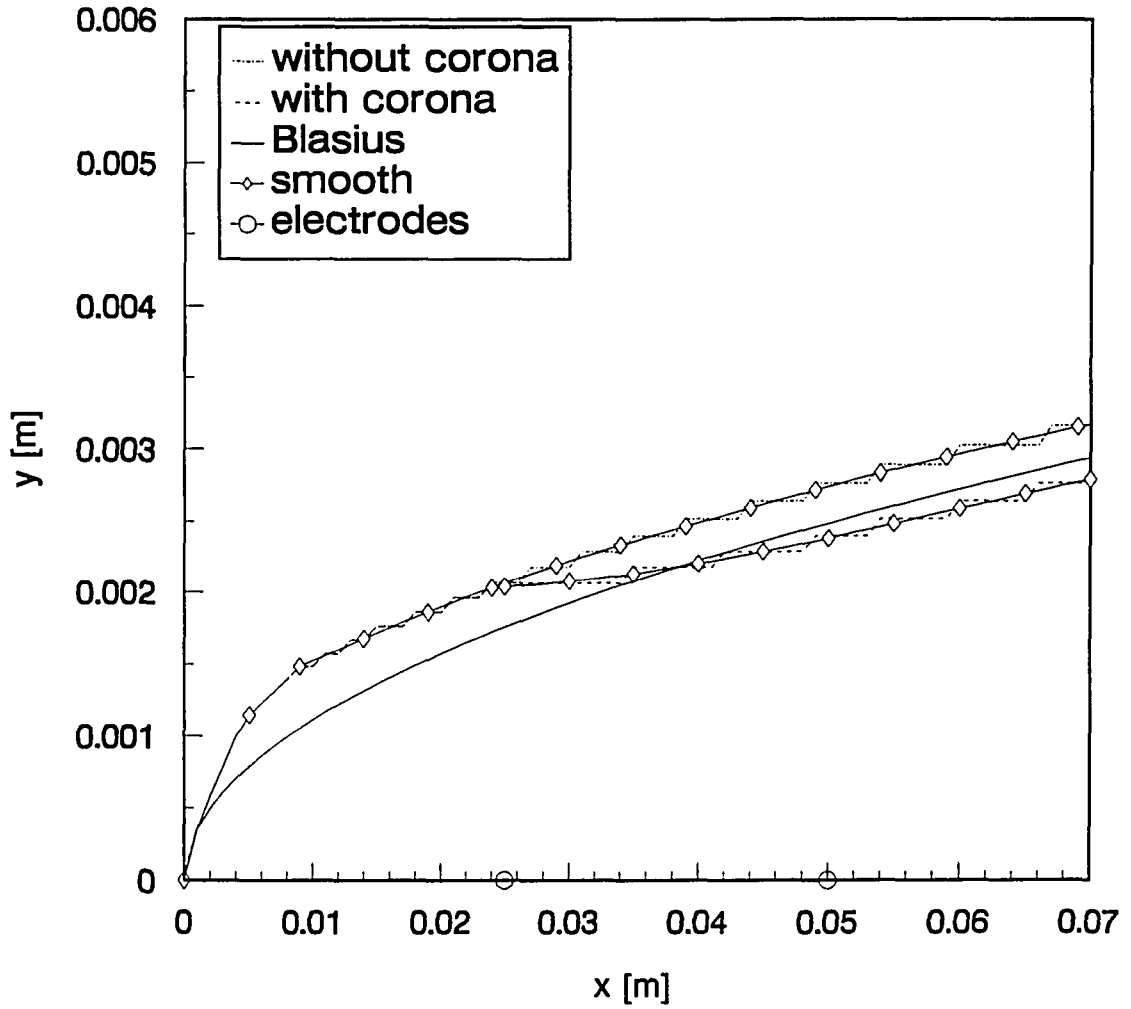


Figure 5.34: Boundary-layer thickness without and with corona effect with ion deposition to surface ($U=3$ m/sec, corona wire is upstream)

Table 5.2: Boundary layer information without corona effect ($\beta = 1.005$)

Velocity [m/sec]	L^* [mm]	L_1^{**} [mm]	L_3^{***} [mm]	δ_{iu}^+ [mm]	$n_{iu}^\#$	δ_{id}^{++} [mm]	$n_{id}^{##}$
1.0	25.0	14.80	25.0	3.6	42	4.8	49
2.0	25.0	7.40	25.0	2.5	34	3.3	40
3.0	25.0	4.93	25.0	2.1	30	2.8	36
4.0	25.0	3.70	25.0	1.8	27	2.4	33
5.0	25.0	2.96	25.0	1.6	25	2.2	31
6.0	25.0	2.47	25.0	1.5	24	2.0	29
7.0	25.0	2.11	25.0	1.4	23	1.9	28
8.0	25.0	1.85	25.0	1.3	22	1.7	26
10.0	25.0	1.48	25.0	1.1	20	1.5	24
12.0	25.0	1.23	25.0	1.1	19	1.4	23
15.0	25.0	0.99	25.0	0.9	17	1.2	21
20.0	25.0	0.74	25.0	0.8	16	1.1	19
25.0	25.0	0.59	25.0	0.8	15	1.0	18
30.0	25.0	0.49	25.0	0.7	14	0.9	17

- * gap length between electrodes.
- ** downstream distance from the leading edge where the boundary layer equations are valid.
- *** location of upstream electrode measured from the plate leading edge.
- + boundary layer thickness at the location of the upstream electrode.
- ++ boundary layer thickness at the location of the downstream electrode.
- # number of grid points dividing the boundary layer thickness at the location of the upstream electrode.
- # number of grid points dividing the boundary layer thickness at the location of the downstream electrode.

discretization of the continuous domain and the definition of the boundary layer thickness as it is the height measured from the plate surface as the local horizontal velocity component equals 99% of the free stream velocity. Smoothing has been applied to these two profiles as shown in this figure. In Figures 5.33 and 5.34 the Blasius solution is added to show the accuracy level of the numerical simulation. Finally Figure 5.35 shows the ratio of the vertical component to the horizontal component of the body force term in the region between the two electrodes. This figure clarifies the restriction which should be considered in the current modeling. The figure shows that this ratio increases as the height from the plate surface increases and since the boundary-layer thickness increases as the free stream velocity decreases, these two facts make the current modeling is inaccurate for low speeds where the boundary-layer thickness is big enough that vertical component of the body force term can not be neglected in comparison to its horizontal component. If the polarity of the two electrodes are set to make the ionic wind moves against the fluid flow direction there will be another restriction in using the boundary layer equations. Since the boundary-layer equations are parabolic and a marching procedure is followed in the numerical solution of these equations and since the marching procedure can be applied only in the direction of the traveling vector and not against its direction, there will be a limit on the minimum value of the free stream velocity which should guarantee that the fluid flow does not make reverse flow in this case. The last restriction which should be considered in the current modeling is the location measured from the plate leading edge where the boundary-layer equations are valid ($Re_x = 1000$). In order to remove these restrictions the boundary-layer equations in this modeling should be replaced by the full Navier-Stokes equations. The graphs showing the behavior of the electrical quantities of this case are very similar to those shown in section 5.1.4.2 and therefore Figure 5.36 which shows the vector plot of the current density in the region between the two electrodes is the only one included here. This figure confirms that

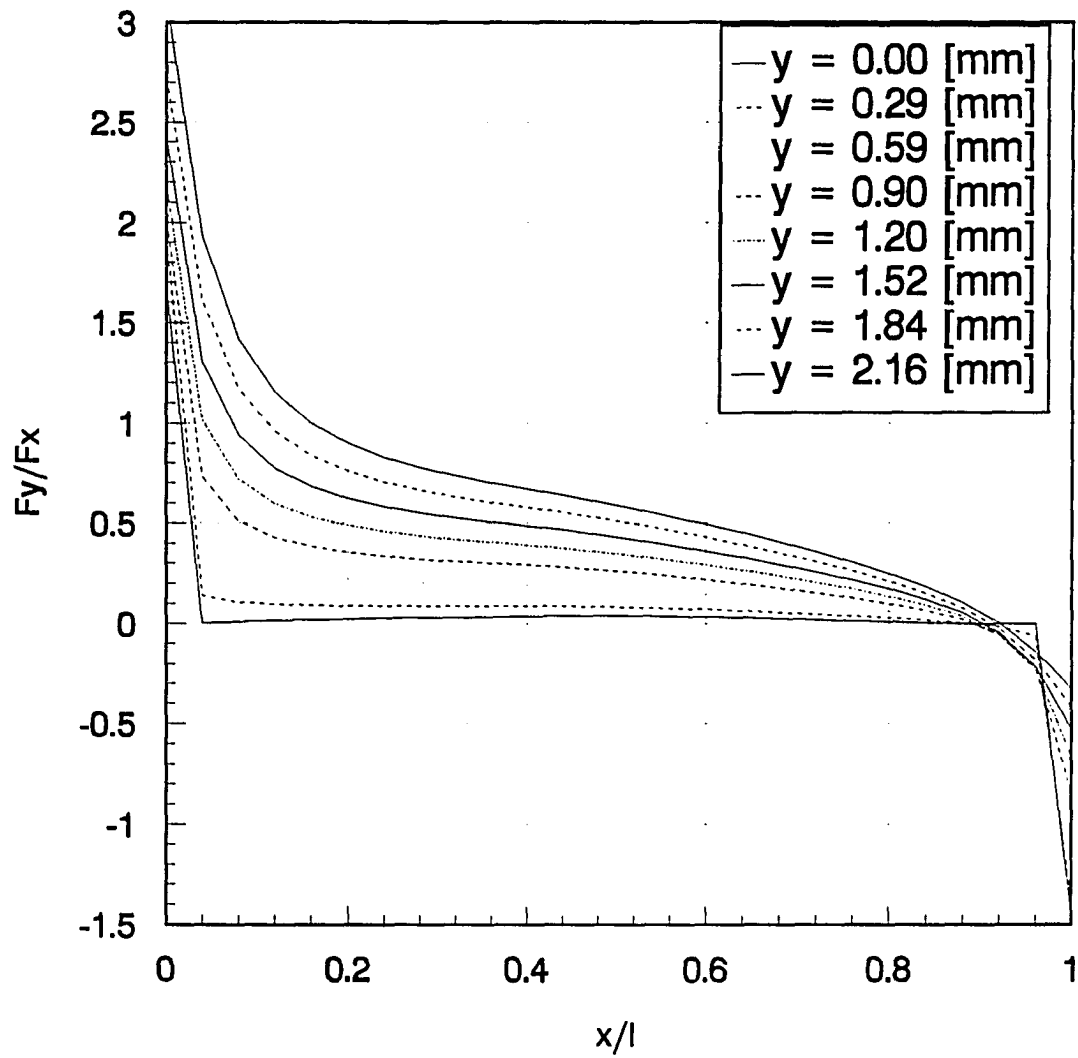


Figure 5.35: Ratio of body force components between the two electrodes at different levels above the surface ($U=3$ m/sec, corona wire is upstream)

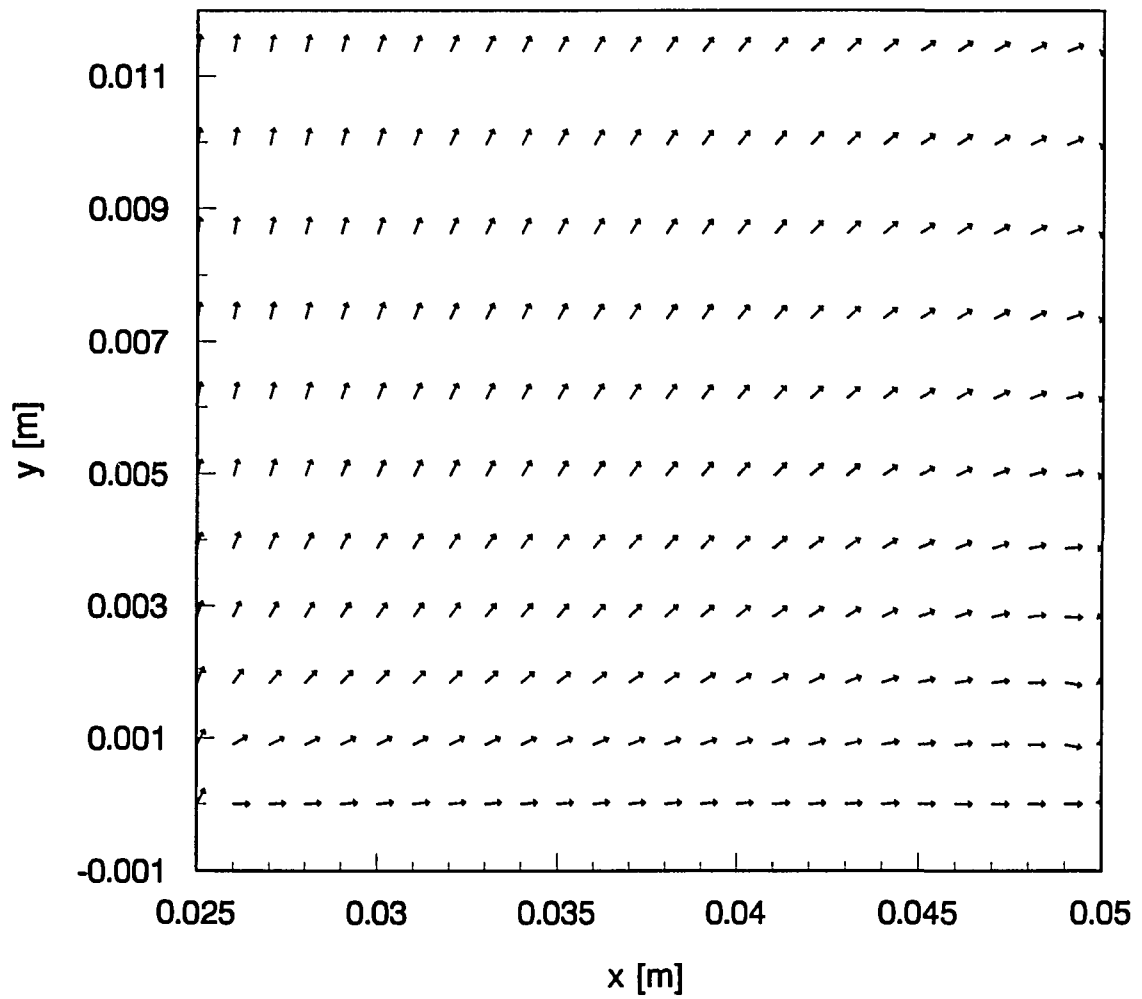


Figure 5.36: Vector plot of current density at different levels above the surface between electrodes with ion deposition to surface ($U = 3$ m/sec, corona wire is upstream)

not all the positive ions emitting at the corona wire will reach the other electrode but some of these ions will travel to infinity.

5.3 Corona Effect and Drag Reduction

As the corona discharge is applied inside the boundary-layer the gained drag reduction varies as the parameters accompany this discharge vary. Our analysis shows that the potential difference between the two electrodes, the gap length between the two electrodes, the location of the corona setup downstream from the leading edge, the diameter of the corona wire, and the value of the free stream velocity of the fluid are effective parameters on the value of the percentage drag reduction which can be achieved on the portion of the plate between the two electrodes. In order to evaluate the effect of each of these parameters the variation of one of them will be considered while the rest are kept constant. The Reynolds number used in this analysis is based on the gap length between the two electrodes.

Considering the variation of the fluid flow velocity and keep all other parameters unchanged. Table 5.3 shows these parameters and the output results for various fluid flow velocities. Figure 5.37 shows the drag force per unit width acting on the plate portion between the two electrodes with and without the effect of corona discharge. This drag force calculated twice; first based on the momentum deficit at the locations of the two electrodes and second based on the shear stress on the plate surface between the two electrodes. Figure 5.38 amplifies the drag force based on the shear stress of Figure 5.37. These two figures confirm the previous description of section 5.2 that the corona discharge along the direction of the fluid flow decreases the drag while it increases the velocity gradient on the surface and the shear stress. In Figure 5.3.7 the drag force based on the shear stress is less than that based on the momentum because it depends on the velocity gradient on the surface which

Table 5.3: Output results for various fluid flow velocities
 $(\Delta \phi = 4000 \text{ volts}, L = 25 \text{ mm}, L_3 = 25 \text{ mm}, d_3 = 2 \mu\text{m})$

Free Stream Velocity [m/sec]	Reynolds Number	Drag (mom.) without corona [N]	Drag (mom.) with corona [N]	DR%	Drag (shear) without corona [N]	Drag (shear) with corona [N]	C_D (Blasius) without corona	C_D (mom.) without corona	C_D (mom.) with corona	C_D (shear) without corona	C_D (shear) with corona
1.0	1689	0.0007	-0.0016	324.7	0.0002	0.0004	0.032	0.047	-0.106	0.013	0.027
2.0	3378	0.0020	-0.0005	124.4	0.0005	0.0007	0.023	0.034	-0.008	0.009	0.012
3.0	5068	0.0037	0.0012	68.6	0.0010	0.0011	0.019	0.027	0.009	0.007	0.008
4.0	6757	0.0058	0.0032	44.5	0.0015	0.0017	0.016	0.024	0.013	0.006	0.007
5.0	8446	0.0081	0.0055	31.8	0.0021	0.0022	0.015	0.021	0.015	0.0056	0.0059
6.0	10140	0.0106	0.0081	24.1	0.0028	0.0029	0.013	0.020	0.015	0.0051	0.0053
7.0	11820	0.0134	0.0108	19.0	0.0035	0.0036	0.012	0.018	0.015	0.0047	0.0049
8.0	13510	0.0164	0.0138	15.5	0.0042	0.0043	0.011	0.017	0.014	0.0044	0.0045
10.0	16890	0.0229	0.0204	11.0	0.0059	0.0060	0.010	0.015	0.013	0.0039	0.0040
12.0	20270	0.0302	0.0277	8.3	0.0077	0.0078	0.009	0.014	0.013	0.0035	0.0036
15.0	25340	0.0423	0.0398	5.9	0.0108	0.0108	0.008	0.012	0.011	0.0031	0.0032
20.0	33780	0.0653	0.0628	3.8	0.0164	0.0165	0.007	0.0108	0.0104	0.00272	0.00273
25.0	42230	0.0914	0.0890	2.7	0.0228	0.0229	0.006	0.0100	0.0090	0.00242	0.00242
30.0	50680	0.121	0.118	2.1	0.0299	0.0299	0.0059	0.0089	0.0087	0.00219	0.00220

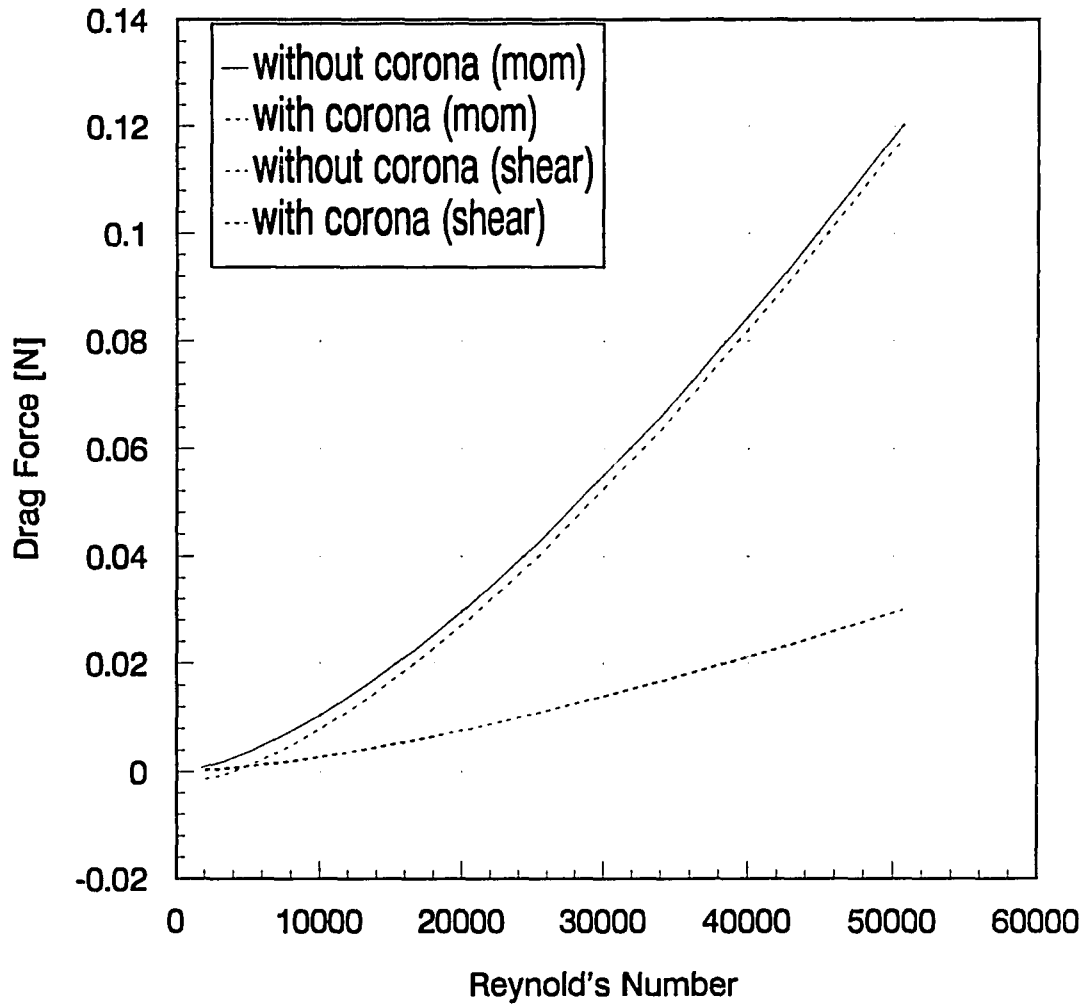


Figure 5.37: Corona effect on drag forces based on momentum and shear vs Reynolds number with ion deposition to surface and corona wire is upstream ($\Delta \phi = 4000$ volts, $L = 25$ mm, $L_3 = 25$ mm, $d_s = 2$ μ m)

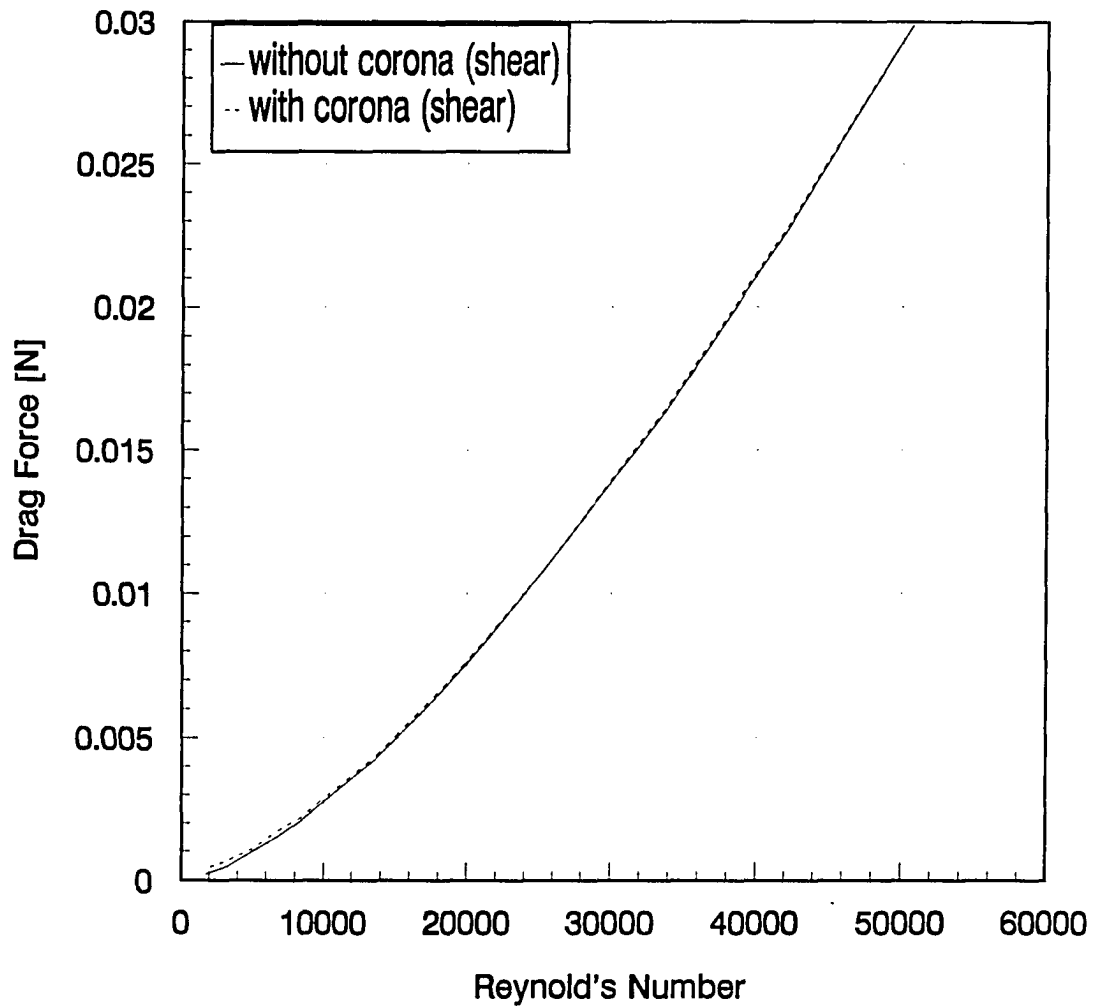


Figure 5.38: Corona effect on drag force based on shear vs Reynolds number with ion deposition to surface and corona wire is upstream ($\Delta \phi = 4000$ volts, $L = 25$ mm, $L_3 = 25$ mm, $d_s = 2$ μ m)

depends on the size of the first step of the grid in the vertical direction. If the first step size can be reduced to be close to the zero, the velocity gradient obtained numerically will be close to the actual one but this condition can not be practically reached due to the round-off error of the computing machine. Figure 5.39 shows the variation of the drag coefficient for different Reynolds numbers (actually it is for various free stream velocities as the gap length is kept constant). Again it confirms the interpretation of the drag force behavior with and without the corona effect. This figure clarifies that the effect of corona on drag reduction diminishes as the free stream velocity increases.

Considering the variation of the electric potential between the two electrodes and keep all other parameters unchanged. Figure 5.40 confirms that the corona effect on the percentage drag reduction diminishes as the free stream velocity increases and shows that this effect increases as the potential difference between the two electrodes increases.

Considering the variation of the gap length between the two electrodes and keep all other parameters unchanged. Figure 5.41 confirms that the corona effect on the percentage drag reduction diminishes as the free stream velocity increases and shows that this effect increases as the gap length between the two electrodes increases.

Considering the variation of the location of the corona setup (location of the upstream electrode) measured from the plate leading edge and keep all other parameters unchanged. Figure 5.42 again confirms that the corona effect on the percentage drag reduction diminishes as the free stream velocity increases and shows that this effect is proportional to how far the location of the corona setup downstream from the leading edge. The corona effect relatively increases as its setup is located farther downstream the leading edge. This is true because the corona effect is not function of this location while the drag force decreases as the location becomes farther downstream the leading edge. This result assures the significance of using the corona effect as a boundary layer control to delay the flow

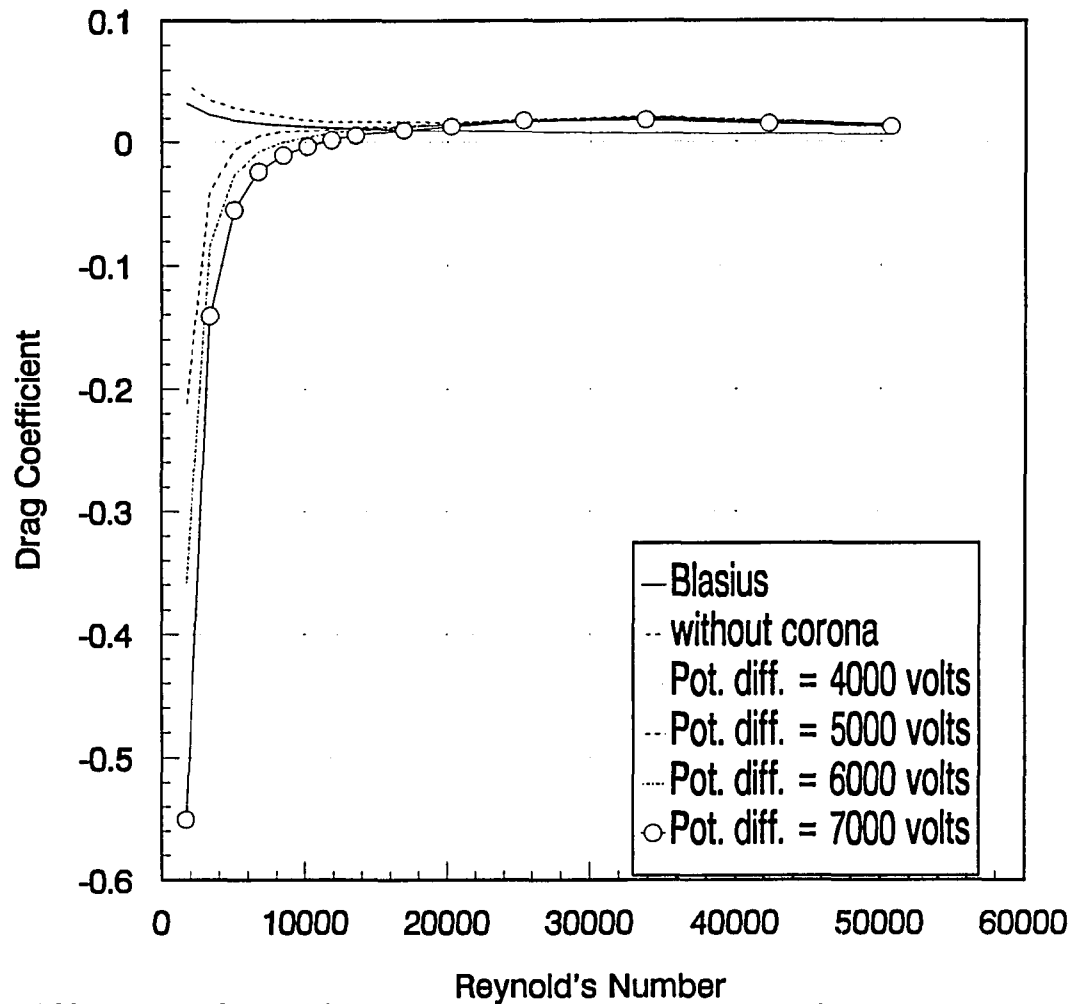


Figure 5.39: Corona effect on drag coefficient based on momentum and shear vs Reynolds number with ion deposition to surface and corona wire is upstream ($L=25\text{ mm}$, $L=25\text{ mm}$, $L_3=25\text{ mm}$, $d_s=2\text{ }\mu\text{m}$)

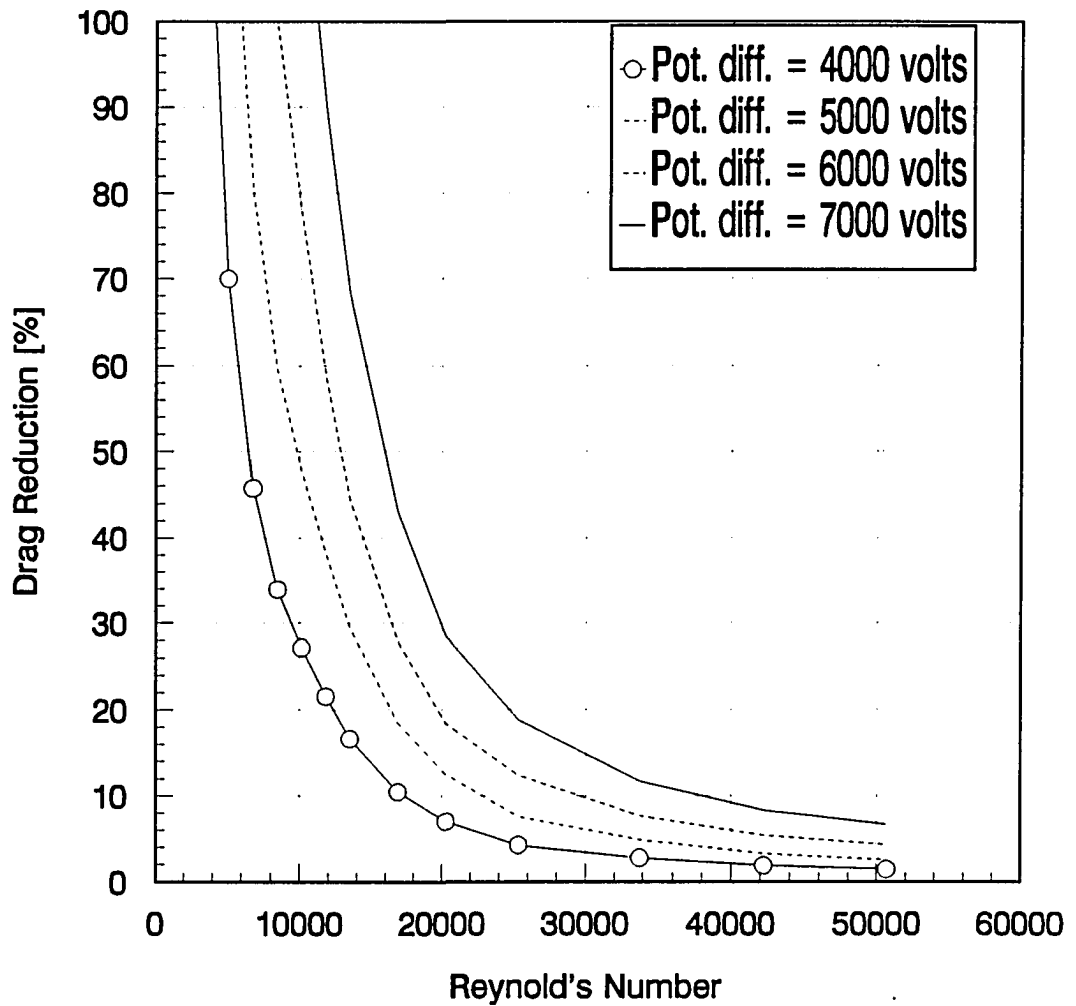


Figure 5.40: Corona effect on percentage drag reduction based on momentum vs Reynolds number for various potential difference between electrodes with ion deposition to surface and corona wire is upstream ($L=25\text{ mm}$, $L_3=25\text{ mm}$, $d_s=2\text{ }\mu\text{m}$)

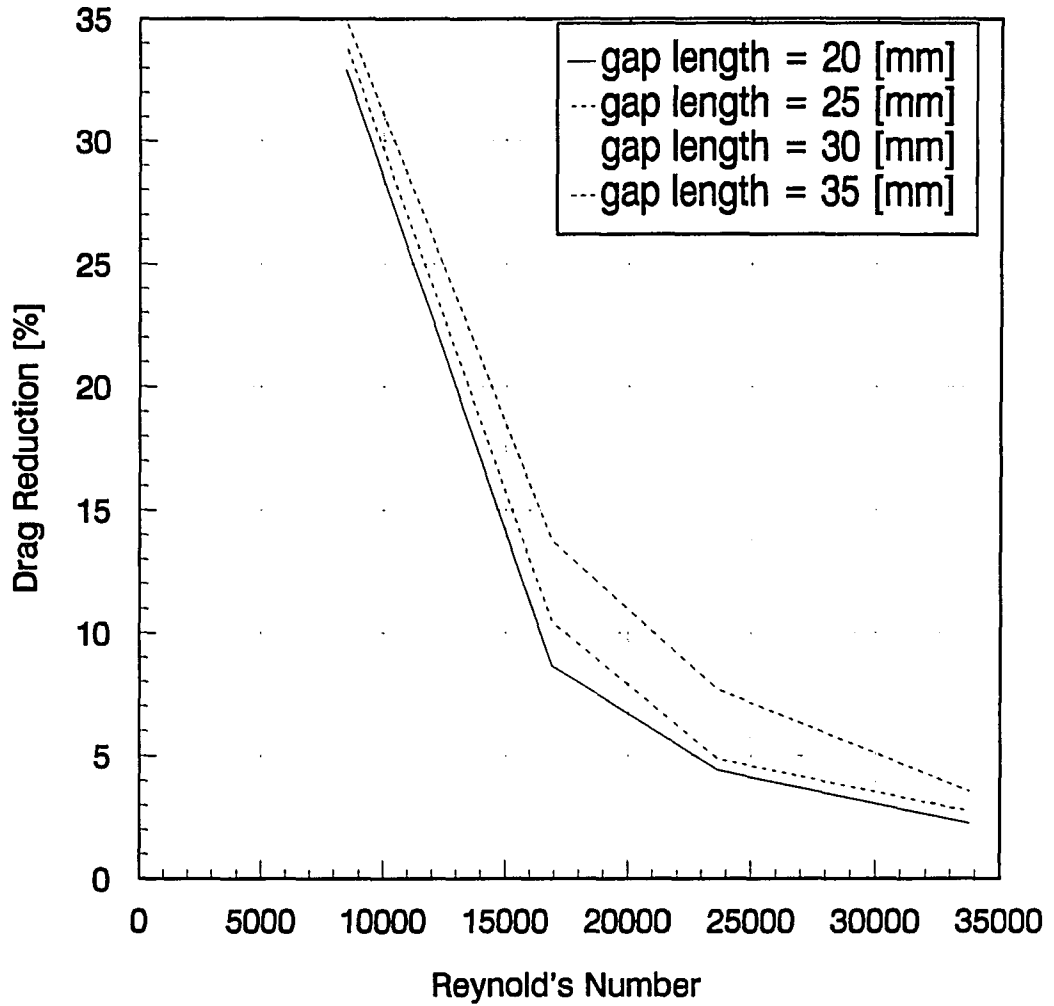


Figure 5.41: Corona effect on percentage drag reduction based on momentum vs Reynolds number for various gap lengths between electrodes with ion deposition to surface and corona wire is upstream ($\Delta \phi = 4000$ volts, $L_3 = 25$ mm, $d_s = 2$ μ m)

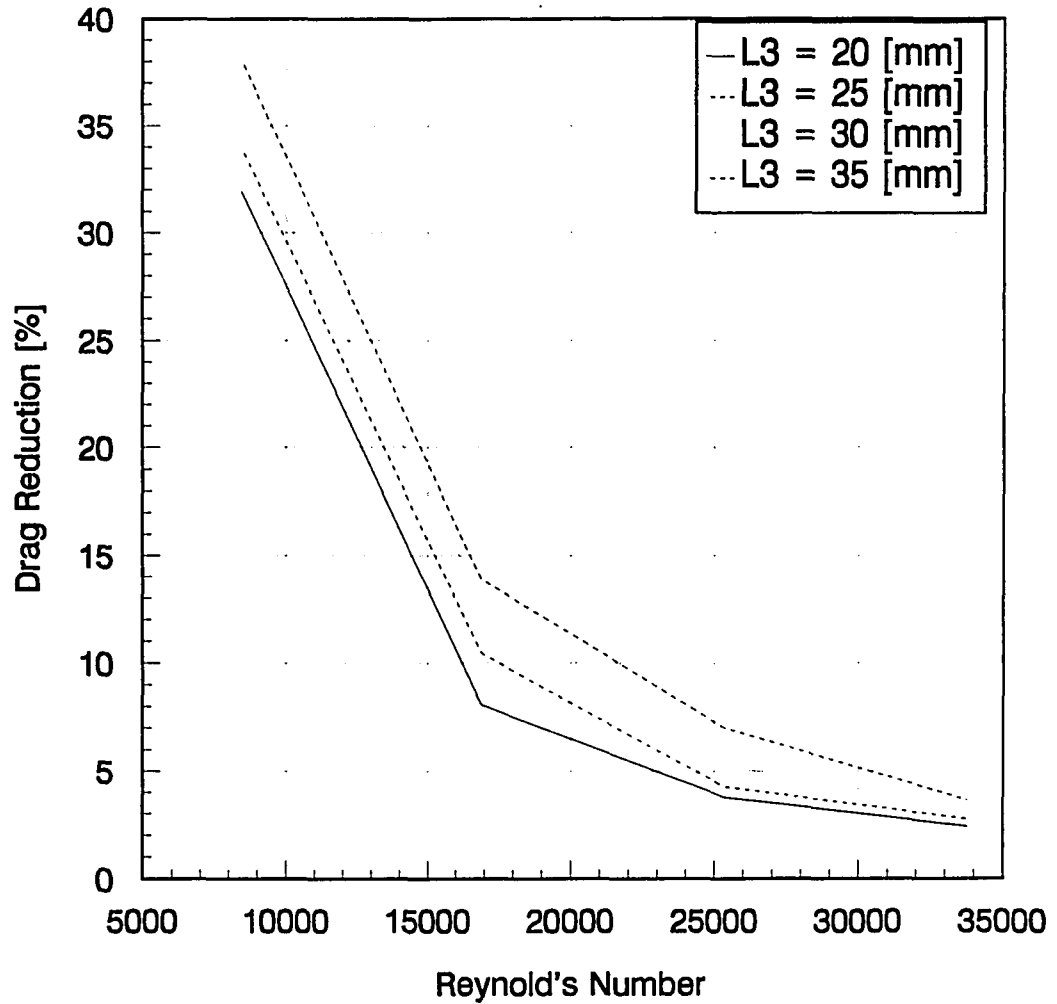


Figure 5.42: Corona effect on percentage drag reduction based on momentum vs Reynolds number for various locations of the corona setup downstream from plate leading edge with ion deposition to surface and corona wire is upstream ($\Delta \phi = 4000$ volts, $L = 25$ mm, $d_s = 2 \mu m$)

separation.

Considering the variation of the corona wire diameter and keep all other parameters unchanged. Figure 5.43 again confirms that the corona effect on the percentage drag reduction diminishes as the free stream velocity increases and shows that this effect is inversely proportional to the corona wire diameter.

5.4 Stability Conditions

The five-point scheme approximating Poisson's equation is an explicit one which is conditionally stable. Three parameters affect the stability of this scheme. These parameters are: the minimum and the maximum step size in the vertical direction of the electrostatic grid and the value of the electric charge density at each grid points. The minimum step size is controlled by the value of the stretching parameter. The maximum step size is chosen through trial and error approach by assigning a value to the screen upon request during the program running that can be changed to a lower one if the program becomes unstable. The charge density is function of the corona current which we do not have any control on it and the only way to handle any instability arise is by increasing the value of the minimum step size. In general the stability conditions for this scheme is obtained computationally for each case. Table 5.4 presents these conditions.

Table 5.4: Stability conditions

Potential Difference [volt]	Domain Height [mm]	Electrostatic Stretching Parameter	Δy_{\min} [mm]	Δy_{limit} [mm]	Δy_{\max} [mm]	$\Delta y_{\max}/\Delta y_{\min}$
3000	300	1.050	0.27	-----	2.92	10.66
4000	300	1.055	0.29	-----	2.86	9.86
5000	300	1.055	0.29	-----	2.86	9.86
6000	300	1.060	0.31	-----	2.81	9.06
7000	300	1.060	0.31	-----	2.81	9.06

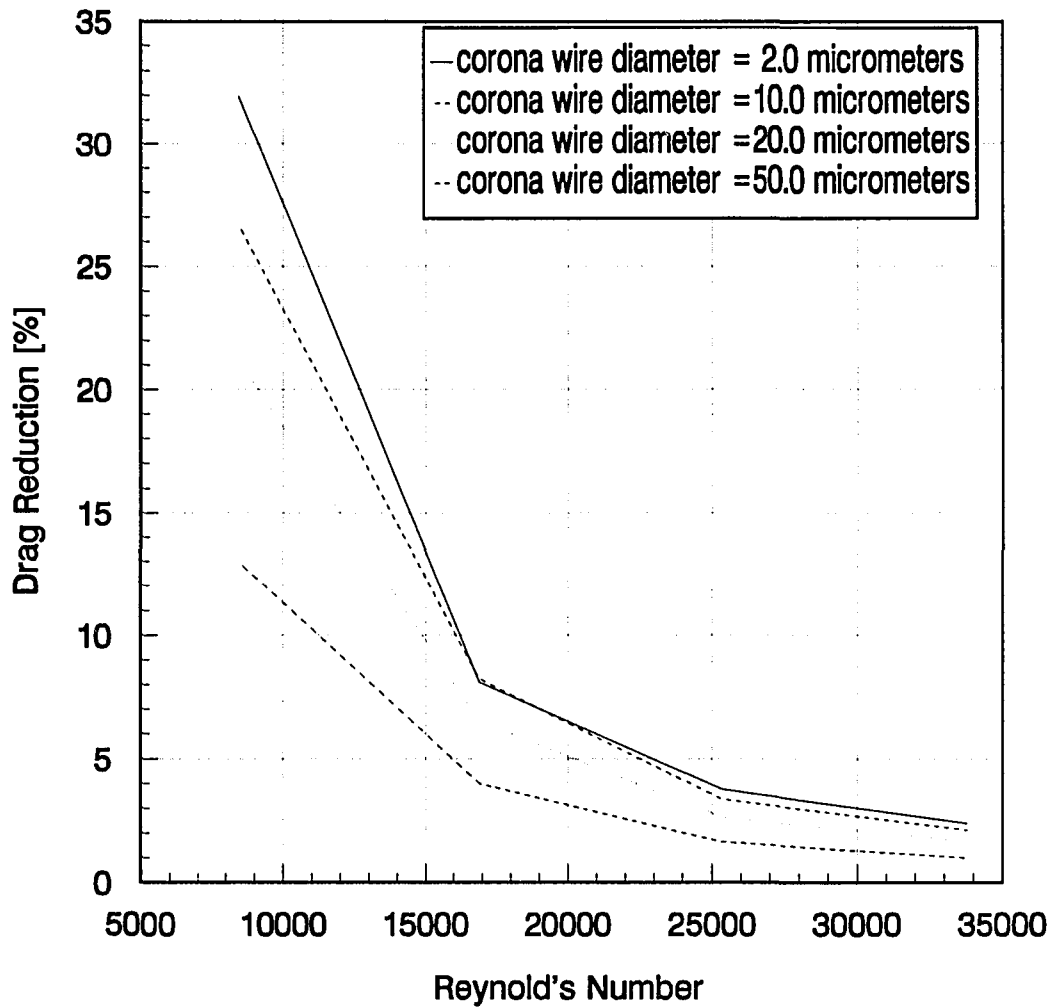


Figure 5.43: Corona effect on percentage drag reduction based on momentum vs Reynolds number for various corona wire diameters with ion deposition to surface and corona wire is upstream ($\Delta \phi = 4000$ volts, $L = 25$ mm, $L_3 = 25$ mm)

5.5 Relaxation Scheme

It was an objective to use this scheme to accelerate the iterative procedure during the solution of Poisson's equation. The numerical solution of the electrostatic equations requires an iterative procedure between Poisson's equation and the conservation of charge equation. Two approaches have been tried to accomplish this solution. First, the iterative procedure starts directly between Poisson's equation and the conservation of charge equation and the relaxation scheme fails to accelerate the iteration procedure and the only value for the relaxation parameter which makes the numerical model stable is ($w = 1.0$). Second, the iterative procedure starts between Poisson's equation and the conservation of charge equation after finishing an iterative procedure on Poisson's equation while dropping the source term and changing it into Laplace equation. During the iterative procedure on Laplace equation it was found that an over relaxation scheme was successful to accelerate this iteration to some extent. It is found that the relaxation parameter is very much related to the stretching parameter. As the value of the stretching parameter becomes smaller the relaxation parameter approaches 1.0. After the solution of Laplace equation converges and the iterative procedure starts between Poisson's equation and the conservation of charge equation it was found that any value for the relaxation parameter other than 1.0 makes the numerical model unstable. It is found that no more than 10% reduction in the number of iterations during Laplace equation solution can be achieved for some cases. The evaluation of the current study requires large number of runnings of the numerical solver and this makes not to use the relaxation scheme or the relaxation parameter equals 1.0 is more economic rather than the try and error method to find an optimum value for the relaxation parameter for each case.

6. CONCLUSIONS

Using corona discharge as a new technique of drag reduction and boundary layer control has been studied using a numerical model. The corona discharge generates an ionic wind which adds momentum to the flow that overcome the viscous effect inside the boundary layer in such a way to reduce the total drag on the moving body and increases the velocity gradient on its surface in such a way to delay the flow separation on the suction side of that body. Due to the complexity of the problem the technique has been evaluated on a flat plate of zero thickness at zero angle of attack for a steady state, two-dimensional, incompressible, viscous flow and the discharge is considered to be a dc positive corona. The boundary layer equations are solved after adding a body force term representing the effect of corona on the boundary layer flow. That requires a coupling between electrostatics and fluid mechanics. A system of five partial differential equations govern this technique. It requires a simultaneous solution accompanied by insufficient boundary conditions. The incomplete boundary conditions necessary for the numerical solution of Poisson's equation is compensated by making the model find the appropriate computational domain which leads to a unique solution. The high velocity gradient inside the boundary layer requires clustering the grid near the surface of the plate. Two grids are used; one grid for the electrostatic solution which is restricted by the stability conditions of the explicit scheme used to approximate Poisson's equation, and the other grid for the boundary layer solution which provides an accurate velocity profile as possible. An interpolation scheme must be added to recalculate the body force term from the electrostatic grid to the boundary layer grid and to recalculate the velocity components of the flow from the boundary layer grid to the electrostatic grid. Using the boundary layer equations is also restricted by minimum value of the free stream velocity which makes boundary layer thin enough to neglect the vertical component of the body force term in comparison to its horizontal component.

To precisely describe the body force term for the boundary layer equations, it requires an understanding of the corona discharge near a surface of finite conductivity. The finite conductivity of the surface has been used in the description of the boundary conditions of the problem. The corona discharge between wire-to-wire electrodes generates corona current in the order of micro amperes. In order to initiate corona between the two electrodes it requires to raise the electric potential between these electrodes to a value higher than the corona onset voltage. It has been concluded that the corona onset voltage is proportional to both the corona wire diameter and the gap length between the two electrodes. In order to determine the appropriate value of the corona current for the model under investigation the data collected by Soetomo for a similar model has been fit into Seaver's equation using the least-squares curve fitting technique and determined the numerical values of the coefficients of that equation which satisfy our model. It has been concluded that the corona current is proportional to the potential difference between the two electrodes. The analysis also shows that the corona current does not significantly respond to the variation of the gap length if the corona wire diameter is small and that the current is inversely proportional to the gap length between the electrodes for larger corona wire diameters.

There are two possibilities for the order of polarity of the two electrodes. First, the electrodes are set in such a way that the ionic wind moves along the direction of the fluid flow and second, are set in such a way that the ionic wind moves against the direction of the fluid flow. It has been concluded that the first setup where the ionic wind moves along the direction of the flow is more beneficial since the corona discharge adds momentum to the fluid flow that reduces the total drag on the plate and increases the velocity gradient on the surface that helps to delay the flow separation while the second setup where the ionic wind moves against the direction of the flow increases the momentum deficit that increases the

total drag on the plate and decreases the velocity gradient on the surface that helps for an early flow separation.

It has been concluded that the value of the drag reduction due to the corona discharge is function of many parameters. The drag reduction is proportional to both the electric potential difference and the gap length between the two electrodes and inversely proportional to the free stream velocity. It is also proportional to the location of the corona setup measured from the plate leading edge and inversely proportional to the corona wire diameter.

Based on that evaluation the corona discharge can be applied to reduce drag on bodies when the Reynolds number is relatively small or more precisely for low free stream velocities. The best way to achieve maximum gain out of this discharge is to install a series corona setups (pairs of electrodes) along the span of that body perpendicular to the direction of the fluid flow. Each pair has a gap length of about one inch and the pairs are separated by about two gap lengths. This arrangement will significantly affect the boundary layer flow by reducing the total drag and delaying the flow separation. The applicability of this technique is very economic, since an electric power of the order of few watts will save tremendous amount of fuel by significantly reducing the total drag on the body. In addition to that it will improve the flight characteristics of the body by delaying the possibility of the flow separation which allow the body to achieve higher angles of attack.

As a final result of this study the corona discharge can be used with higher efficiency in electrostatic cooling. Its higher effect at low flow speeds confirms its ability to significantly enhance the cooling rate around a hot body by boosting the convection of the flow around that body. The quantitative analysis of electrostatic cooling is the natural extension of this study. In addition to that the corona discharge can be applied to other electrostatic applications based on the achieved understanding of the surface-gas interactions.

REFERENCES

- [1] Bartnikas, R., and McMahon, E. I. *Engineering dielectrics Volume I Corona measurements and interpretation*. ASTM special technical publication 669, Baltimore, MD, 1979.
- [2] Velkoff, H. R., and Godfrey, R. "Low-velocity heat transfer to a flat plate in the presence of a corona discharge in air," *Journal of Heat Transfer*, Vol. 101, pp. 157-163, February 1979.
- [3] Munson, B., Young, D., and Okiishi, T. *Fundamentals of fluid mechanics*. John Wiley & Sons Inc., New York, NY, 1990.
- [4] Bushnell, D. M., and Hefner, J. N. *Viscous drag reduction in boundary layer*. Volume 123, Progress in Astronautics and Aeronautics, AIAA, Washington D.C., 1990.
- [5] Bushnell, D. M., Anders, J. B., Walsh, M. J., and McInville, R. V. "Turbulent drag reduction research," *AGARD conference proceedings no. 365*, pp. 17-1 to 17-13, Brussels, Belgium, May 1984.
- [6] Bushnell, D. M. "Turbulent drag reduction for external flows," *AIAA-83-0227. AIAA 21st Aerospace Sciences Meeting*, Reno, Nevada, January 1983.
- [7] Malik, M. R., Weinstein, L. M., and Hussaini, M. Y. "Ion wind drag reduction," *AIAA-83-0231. AIAA 21st Aerospace Sciences Meeting*, Reno, Nevada, January 1983.
- [8] Velkoff, H. R. "Evaluating the interactions of electrostatic fields with fluid flows," *ASME Paper No. 71-DE-41*, 1971.
- [9] Velkoff, H. R., and Kulacki, F. A. "Electrostatic cooling," *ASME Paper No. 77-DE-36*, 1977.

- [10] Kibler, K. G., and Carter Jr., H. G. "Electrocooling in gases," *J. Applied Physics*, Vol. 45, pp. 4436-4440, 1974.
- [11] White, H. J. *Industrial Electrostatic Precipitation*. Addison-Wesley Publishing Company, Inc., Reading, Massachusetts, 1963.
- [12] Perry, R. H., Green, D., and Maloney, J. O. *Perry's Chemical Engineer's Handbook*. Sixth edition, McGraw Hill Inc., New York, NY, 1984.
- [13] Leob, L. B. *Fundamental Processes of Electrical Discharge in Gases*. John Wiley & Sons, Inc., New York, NY, 1939.
- [14] Davidson, J. H., and McKinney, P. J. "EHD flow visualization in the wire-plate and barbed plate electrostatic precipitator," *IEEE Transactions on Industry Applications*, vol. 27, no. 1, pp. 154-160, January/February 1991.
- [15] Liu, X. K., Colver, G. M. "Capture of fine particles on charged moving spheres: a new electrostatic precipitator," *IEEE Transactions on Industry Applications*, vol. 27, no. 5, pp. 807-815, September/October 1991.
- [16] Cristina, S., Dinelli, G., and Feliziani, M. "Numerical computation of corona space charge and V-I characteristic in dc electrostatic precipitators," *IEEE Transactions on Industry Applications*, vol. 27, no. 1, pp. 147-153, January/February 1991.
- [17] Butler, A. J., Cendes, Z. J., and Hoburg, J. F. "Interfacing the finite-element method with the method of characteristics in self-consistent electrostatic field models," *IEEE Transactions on Industry Applications*, vol. 25, no. 3, pp. 533-538, May/June 1989.
- [18] Levin, P. L., Hoburg, J. F. "Donar cell-finite element descriptions of wire-duct precipitator fields, charges, and efficiencies," *IEEE Transactions on Industry Applications*, vol. 26, no. 4, pp. 662-670, July/August 1989.

- [19] Davis, J. L., Hoburg, J. F. "Wire-Duct precipitator field and charge computation using finite element and characteristics methods," *Journal of Electrostatics*, vol. 14, pp. 187-199, 1983.
- [20] Lawton, J., and Weinberg, F. J. *Electrical Aspects of Combustion*. Clarendon Press, Oxford, UK, 1969.
- [21] Weinberg, F. J. *Advanced Combustion Methods*. Academic Press Inc. Ltd., London, UK, 1986.
- [22] Colver, G. M., and Nakai, Y. "Flame stabilization by an electrical discharge and flame visualization of the influence of a semi-insulating wall on the ionic wind," *Proceeding of the 13th annual meeting of the IEEE Industry Applications Society*, pp. 95-104, Toronto, October 1978.
- [23] Chapman, T. C., and Wintle, H. J. "Surface-charge-limited transient currents on insulating surfaces," *Journal of Applied Physics* 53 (11), pp. 7425-7435, November 1982.
- [24] Sigmond, R. S., Goldman, M. "Some basic gas and surface discharge phenomena in electrostatics," The Institute of Physics, Bristol and London, Conf. Ser. No. 66, *Proceeding of the Sixth Conference on Electrostatic Phenomena*, pp. 81-91, Catherine's College, Oxford, April 1983.
- [25] Soetomo, F. "The influence of high voltage discharge on flat plate drag at low Reynolds number air flow," M.S. thesis, Iowa State University, Ames, Iowa, 1992.
- [26] Weinstein, L. M., and Balasubramanian R. "An electrostatically driven surface for flexible wall drag reduction studies," *Proceeding of Second International Conference on Drag Reduction*, pp. E5-55 to E5-76, St. John's College, Cambridge, England, August 1977.

- [27] Medvedev, V. F., and Krakov, M. S. "Flow Separation by means of magnetic fluid," *Journal of Magnetism and Magnetic Materials*, Vol. 39, Nos. 1&2, pp. 119-122, North-Holland, November 1983
- [28] Abdel-Salam, M. "Positive wire-to-plane coronas as influenced by atmospheric humidity," *IEEE Transactions on Industry Applications*, vol. IA-21, no. 1, pp. 35-40, January/February 1985.
- [29] Abdel-Salam, M., and Fouad, L. "Positive corona from two interacting thin points in air," *IEEE-IAS*, pp. 91-97, 1979.
- [30] Abdel-Salam, M., Abdel-Fattah, A., Saied, M. M., and El-Mohandes, M. T. "Positive corona pulse characteristics from two interacting needles in air," *IEEE Transactions on Industry Applications*, vol. IA-21, no. 4, pp. 912-918, July/August 1985.
- [31] Chapman, S. "The magnitude of corona point discharge current," *Journal of The Atmospheric Sciences*, pp. 1801-1809, Nov. 1979.
- [32] Anderson, D. A., Tannehill, J. C., and Pletcher, R. H. *Computational fluid mechanics and heat transfer*. Hemisphere Publishing Corporation, New York, 1984.
- [33] Patankar, S. V., and Spalding, D. B. *Heat and mass transfer in boundary layer*. Morgan-Grampian, London, 1967.
- [34] Hornbeck, R. W. *Numerical marching techniques for fluid flows with heat transfer*. Scientific and Technical Information Office, National Aeronautics and Space Administration, Washington, D.C., 1973.
- [35] Cobine, J. *Gaseous conduction*. Dover Publications Inc., New York, 1958.
- [36] Cross, J. *Electrostatics: principles, problems and applications*. Adam Hilger Bristol, England, 1986.

- [37] Charan, R. *Hand book of glass technology*. Third Edition, Published by Dr. R. Charan, Banaras Hindu University, Banaras, India, 1956.
- [38] Littleton, J. T., and Morey, G.W. *The electric properties of glass*. John Wiley & Sons, Inc., New York, NY, 1933.
- [39] Doremus, R. H. *Glass science*. John Wiley & Sons, Inc., New York, 1973.
- [40] Nayfeh, M. H., and Brussel, M. K. *Electricity and magnetism*. John Wiley & Sons, Inc., New York, NY, 1985.
- [41] Currie, I. G. *Fundamentals mechanics of fluids*. McGraw-Hill Book Company, New York, NY, 1974.
- [42] Schlichting, H. *Boundary layer theory*. Seventh Edition, McGraw-Hill Book Company, New York, NY, 1979.
- [43] White, F. M. *Viscous fluid flow*. McGraw-Hill, Inc., New York, NY, 1991.
- [44] Reitz, J. R., and Milford, F. J. *Foundation of electromagnetic theory*. Addison-Wesley Publishing Company, Inc., Reading, MA, 1964.
- [45] Becker, A. A. *The boundary element method in engineering; A complete course*. McGraw-Hill Book Company, New York, NY, 1992.
- [46] Hoffman, J. D. *Numerical methods for engineers and scientists*. McGraw-Hill, Inc., New York, NY, 1992.
- [47] Minkowycz, W. J., Sparrow, E. M., Schneider, G. E., Pletcher, R.H. *Handbook of numerical heat transfer*. John Wiley & Sons, Inc., New York, NY, 1988.
- [48] Prusa, J. M. "A spatial Stefan problem modified by natural convection: melting around a horizontal cylinder," PhD Thesis, University of Illinois at Urbana-Champaign, Urbana, IL, 1983.

- [49] Collins, W. M. and Dennis, S. C. R. "The steady motion of a viscous fluid in a curved tube," *The Quarterly Journal of Mechanics and Applied Mathematics*, Vol. XXXVIII, pp. 133-156, Clarendon Press, Oxford, 1975.
- [50] Jong, Suk Lee "Freezing problem in pipe flow," PhD Thesis, Iowa State University, Ames, IA, 1993.
- [51] Schaffert, R. M. *Electrophotography*. The Focal Press, London and New York, NY, 1971.
- [52] Oglesby, S., et al, *A manual of electrostatic precipitator technology - part I - fundamentals*. Southern Research Institute, Birmingham, Alabama, August 1970.
- [53] Seaver, A. E. "Calculation of unipolar space charge current and pressure at high potential," *IEEE/IAS 92 annual meeting*, Houston, TX, Conf. Record pp. 1539-1545.
- [54] Seaver, A. E. "Onset potential for unipolar charge injection," *IEEE/IAS*, pp. 1-7, Toronto, Canada, October 1993.
- [55] Hornbeck, R. W. *Numerical Methods*. Prentice-Hall, Inc., Englewood Cliffs, NJ, 1975.

APPENDIX A
EFFECTIVE ELECTROMAGNETIC FORCE ON CHARGED PARTICLES

If n positive ions per unit volume, each of charge q , are moving with velocity \vec{v} along the direction of an applied electric field \vec{E} between two electrodes apart by distance L , and at potential difference $\Delta\phi$, a current charge density will be created.

$$\vec{J} = nq\vec{v} \quad (\text{A.1})$$

Substituting for the drift velocity \vec{v} using equation (3.1.3) gives,

$$\vec{J} = nqk\vec{E} \quad (\text{A.2})$$

with

$$\vec{E} = \frac{\Delta\phi}{L}\vec{e} \quad (\text{A.3})$$

therefore,

$$\vec{J} = \frac{nqk\Delta\phi}{L}\vec{e} \quad (\text{A.4})$$

where \vec{e} is a unit vector along the electric field.

This electric current density creates a magnetic field \vec{B} as shown in Figure 3.1. The magnitude of this magnetic field can be obtained by using Ampere's law [40]:

$$\oint \vec{B} \cdot d\vec{l} = \mu_0 \int \vec{J} \cdot d\vec{A} \quad (\text{A.5})$$

Substituting for \vec{J} using equation (A.4), this integral gives,

$$\vec{B} = \frac{nqk\mu_0 \Delta\phi r}{2L} \vec{t} \quad (\text{A.6})$$

where \vec{t} is a unit vector along the magnetic field \vec{B} .

The force due to the magnetic field, which is known as Lorentz force, is defined as:

$$\vec{F}_m = \vec{J} \times \vec{B} \quad (\text{A.7})$$

Substituting for \vec{J} and \vec{B} and the drift velocity \vec{v} of the ions as function of the mobility k and the electric field \vec{E} and considering the number of ions n per unit volume gives the force due to the magnetic field as:

$$\vec{F}_m = \frac{(nqk \Delta\phi)^2 \mu_0 r}{2L^2} (-\vec{r}) \quad (\text{A.8})$$

where r is the radius of the current beam and \vec{r} is a unit vector along this radius.

This means that the magnetic field pushes the ions towards the center of the current beam. On the other hand the force due to the electric field pushes the ions along the current beam and has a value of:

$$\vec{F}_e = \frac{nq \Delta\phi}{L} \vec{e} \quad (\text{A.9})$$

Using the appropriate numbers from Appendix G, both \vec{F}_m and \vec{F}_e show:

$$\begin{aligned} F_e &= 5.44 \text{ N} \\ F_m &= 9 * 10^{-14} \text{ N} \end{aligned} \quad (\text{A.10})$$

It is concluded that the force due to the magnetic field is very small compared with that due to the electric field and can be neglected. Thus, the electromagnetic force acting on the charged particles can be considered as due to the electric field only.

APPENDIX B
CORONA CURRENT

The corona current will be calculated according to Seaver equation which can be written below as:

$$I_c = \frac{1}{b} [e^{a(\Delta\phi - V_0)} - 1] \quad [mA] \quad (B.1)$$

In order to determine the numerical values of a . and b in equation (B.1) we will fit Soetomo's data into this equation by using the least-squares curve fitting technique. Soetomo's setup is composed of two wire electrodes each is of 2-micrometer diameter and 28-mm length. The gap length between the two electrodes is 25 mm. Table B.1 provides the current-voltage measurements of Soetomo [25].

Table B.1: Soetomo' current-voltage measurements

potential difference between electrodes [kV]	corona current measured [mA]
14.0	0.0001023
16.0	0.02577
18.0	0.09337
20.0	0.1457

The onset corona voltage is calculated according to equations (3.4.1 and 3.4.3) which will be rewritten here as:

$$E_c = 30 m \delta \left(1 + \frac{0.301}{\sqrt{a \delta}}\right) \quad (\text{B.2})$$

$$V_o = E_c a \ln\left(\frac{S}{a}\right) \quad (\text{B.3})$$

where a is the radius of the corona wire ($a = 2.0$ micrometers), m is an irregularity factor which has the value 0.72 for standard wires and, δ is a factor related to the gas (air) according to equation (3.4.2).

$$\delta = \frac{3.92b}{273 + t} \quad (\text{B.4})$$

where b is the air pressure in centimeters of mercury, and t is the temperature in degrees centigrade. At 25°C and 76 cm Hg. $\delta \approx 1.0$.

According to equation (B.2)

$$\begin{aligned} E_c &= 671.76 \quad [kV / cm] \\ &= 67.176 * 10^6 \quad [V / m] \end{aligned} \quad (\text{B.5})$$

According to equation (B.3) and for the $2 \mu m$ wire diameter and the 25 mm gap length between the two electrodes, the corona onset voltage will have the value

$$V_o = 0.68027 \quad [kV] \quad (\text{B.6})$$

The value of the corona onset voltage can be added to Table B.1 as the potential difference between the two electrodes corresponding to zero corona current.

Defining

$$x = \Delta\phi - V. \quad (\text{B.7})$$

equation (B.1) becomes

$$I_c(x) = \frac{1}{b} [e^{ax} - 1] \quad (\text{B.8})$$

Generating a least-squares equation using equation (B.8) and the data of Table B.1

$$d = \sum_{i=1}^n (I(x_i) - f(x_i))^2 \quad (\text{B.9})$$

where n is the number of the data points and $f(x_i)$ is the value of the measured current at each point.

Usually the least-squares equation will be differentiated with respect to each of the unknown coefficients, one at a time, and put equal to zero. This procedure generates number of equations equal to the number of unknowns which can be solved for these unknowns. Because of the complexity of equation (B.9) the optimum values of a and b will be obtained numerically. A range of values for a and b will be initially assumed and a FORTRAN code is written and run to find out the optimum values of a and b which represent the best fit of Soetomo's data into Seaver's equation. The program will continue to calculate the value of "d" in equation (B.9) using all the assumed values of a and b , pair at a time, until the minimum value of "d" is obtained for specific values of a and b . These a .

and b are the ideal values for the best fit of Soetomo's data into Seaver's equation. The numerical values found out of this program are listed here

$$a_0 = 0.365 \quad [kV]^{-1} \quad (\text{B.10})$$

and

$$b = 7615.0 \quad [mA]^{-1} \quad (\text{B.11})$$

which gives

$$R = 2.086 \quad [M\Omega] \quad (\text{B.12})$$

APPENDIX C
DERIVATION OF BOUNDARY LAYER EQUATIONS
WITH CORONA DISCHARGE

In general it is possible to state that the boundary layer thickness increases with viscosity or in other words it decreases as the Reynolds number increases. It is clear from several exact solutions of the Navier-Stokes equations that the boundary layer thickness is proportional inversely to the square root of the Reynolds number and to the square root of kinematic viscosity [41,42].

$$\left. \begin{aligned} \delta &\approx \sqrt{\nu} \\ \delta &\approx \frac{1}{\sqrt{\text{Re}}} \end{aligned} \right\} \quad (\text{C.1})$$

To simplify the Navier-Stokes equations so as to obtain the boundary layer equations, which include a body force term due to the corona discharge inside the boundary layer, it is assumed that for all points in the boundary layer except those near the leading edge the boundary layer thickness is very small compared with a still unspecified characteristic length L , e.g. the distance from the leading edge, i.e.,

$$\frac{\delta}{L} \ll 1 \quad (\text{C.2})$$

An order of magnitude analysis for each term in the mass continuity equation and the Navier-Stokes equations can be carried out. The procedure starts by putting the equations in a non-dimensional form by referring all velocities to the free stream velocity U , all electric field components to the average electric field between the two electrodes E_{av} , and all linear dimensions to the characteristic length L , which will ensure that the dimensionless derivative

$\frac{\partial \bar{u}}{\partial \bar{x}}$ does not exceed unity in the region under consideration. The fluid density inside the boundary layer is referred to the free stream flow density and the charge density ρ_c to the charge density at the positive electrode ρ_{c^0} . This requires introducing the following non-dimensional parameters:

$$\begin{aligned} \bar{x} &= \frac{x}{L} & \bar{y} &= \frac{y}{L} \\ \bar{u} &= \frac{u}{U} & \bar{v} &= \frac{v}{U} \\ \bar{\rho} &= \frac{\rho}{\rho_\infty} & \bar{p} &= \frac{p}{\rho_\infty U^2} \\ \bar{v} &= \frac{v}{UL} = \frac{1}{R_L} & \bar{\rho}_c &= \frac{\rho_c}{\rho_{c^0}} \\ \bar{E}_x &= \frac{E_x}{E_{av}} & \bar{E}_y &= \frac{E_y}{E_{av}} \end{aligned}$$

where,

$$E_{av} = \frac{\Delta\phi}{L}$$

Inside the thin boundary layer we assume (our calculations will confirm this assumption) the x-component of the electric field is of the same order of magnitude as E_{av} while the y-component is very small compared with E_{av} except very close to the electrodes.

$$\left. \begin{aligned} E_x &\approx E_{av} \\ E_y &\ll E_{av} \\ E_y &\ll E_x \end{aligned} \right\} \quad (C.3)$$

i.e., if E_x can be described as of order 1, E_y can be described as of order δ .

Substituting in equation (3.6.1.3) using the non-dimensional parameters, leads to a non-dimensional form as follows:

$$\frac{U}{L} \frac{\partial \bar{u}}{\partial \bar{x}} + \frac{U}{L} \frac{\partial \bar{v}}{\partial \bar{y}} = 0 \quad (\text{C.4})$$

which can be written as:

$$\frac{\partial \bar{u}}{\partial \bar{x}} + \frac{\partial \bar{v}}{\partial \bar{y}} = 0 \quad (\text{C.5})$$

Repeating the same procedure with equation (3.6.1.4) gives,

$$\bar{u} \frac{U^2}{L} \frac{\partial \bar{u}}{\partial \bar{x}} + \bar{v} \frac{U^2}{L} \frac{\partial \bar{u}}{\partial \bar{y}} = \frac{1}{\bar{\rho} \rho_\infty} \bar{\rho}_c \rho_{c^0} \bar{E}_x E_{av} - \frac{1}{\bar{\rho} \rho_\infty} \frac{\rho_\infty U^2}{L} \frac{\partial \bar{p}}{\partial \bar{x}} + \bar{v} UL \left(\frac{U}{L^2} \frac{\partial^2 \bar{u}}{\partial \bar{x}^2} + \frac{U}{L^2} \frac{\partial^2 \bar{u}}{\partial \bar{y}^2} \right) \quad (\text{C.6})$$

and since $\frac{\rho_{c^0}}{\rho_\infty} E_{av}$ has the unit of $[m/sec^2]$ which is the same as for $\frac{U^2}{L}$ the above equation can

be written as:

$$\bar{u} \frac{\partial \bar{u}}{\partial \bar{x}} + \bar{v} \frac{\partial \bar{u}}{\partial \bar{y}} = \frac{\bar{\rho}_c}{\bar{\rho}} \bar{E}_x - \frac{1}{\bar{\rho}} \frac{\partial \bar{p}}{\partial \bar{x}} + \bar{v} \left(\frac{\partial^2 \bar{u}}{\partial \bar{x}^2} + \frac{\partial^2 \bar{u}}{\partial \bar{y}^2} \right) \quad (\text{C.7})$$

Finally equation (3.6.1.4) can be written in the following non-dimensional form:

$$\bar{u} \frac{\partial \bar{u}}{\partial \bar{x}} + \bar{v} \frac{\partial \bar{u}}{\partial \bar{y}} = \frac{\bar{\rho}_c}{\bar{\rho}} \bar{E}_x - \frac{1}{\bar{\rho}} \frac{\partial \bar{p}}{\partial \bar{x}} + \frac{1}{R_L} \left(\frac{\partial^2 \bar{u}}{\partial \bar{x}^2} + \frac{\partial^2 \bar{u}}{\partial \bar{y}^2} \right) \quad (\text{C.8})$$

A similar procedure can be followed with equation (3.6.1.5) which finally can be written in the following non-dimensional form:

$$\bar{u} \frac{\partial \bar{v}}{\partial \bar{x}} + \bar{v} \frac{\partial \bar{v}}{\partial \bar{y}} = \frac{\bar{\rho}_c}{\bar{\rho}} \bar{E}_y - \frac{1}{\bar{\rho}} \frac{\partial \bar{p}}{\partial \bar{y}} + \frac{1}{R_L} \left(\frac{\partial^2 \bar{v}}{\partial \bar{x}^2} + \frac{\partial^2 \bar{v}}{\partial \bar{y}^2} \right) \quad (\text{C.9})$$

An order of magnitude estimation of each term of equations (C.5), (C.8) and (C.9) helps one in neglecting small terms and achieving a simplification of the governing equations. Since the term $\frac{\partial \bar{u}}{\partial \bar{x}}$ in equation (C.5) is of order 1, it follows that the term $\frac{\partial \bar{v}}{\partial \bar{y}}$ is also of order 1 and since at the wall $v=0$, it follows that the boundary layer velocity component v and also \bar{v} are of order δ and consequently the dimensionless linear length \bar{y} is also of order δ . Thus one retains both terms of equation (C.5).

Following a similar approach with equation (C.8), both inertia terms of the left hand side will be of order 1 and the first of the viscous terms of the right hand side will be of order 1 and the second term will be of order $\frac{1}{\delta^2}$. The Reynolds number is assumed to be large which makes the ratio $\frac{1}{R_L}$ small. Some of the viscous terms must be of the same order of magnitude as the inertia terms at least in the immediate neighborhood of the wall. It follows that the viscous forces in the boundary layer can become of the same order of magnitude as the inertia forces if the Reynolds number is of the order $\frac{1}{\delta^2}$ (see equation C.1).

The non-dimensional space charge density inside the boundary layer is at most of order 1 while the x-component of the electric field will be of order 1 while the y-component of the electric field will be of order δ at locations not very close to the electrodes. The order of magnitudes of all terms of equation (C.2) are as follows:

$$\left. \begin{array}{l} \bar{u} \frac{\partial \bar{u}}{\partial \bar{x}} + \bar{v} \frac{\partial \bar{u}}{\partial \bar{y}} = \frac{\bar{\rho}_c}{\bar{\rho}} \bar{E}_x - \frac{1}{\bar{\rho}} \frac{\partial \bar{p}}{\partial \bar{x}} + \frac{1}{R_L} \left(\frac{\partial^2 \bar{u}}{\partial \bar{x}^2} + \frac{\partial^2 \bar{u}}{\partial \bar{y}^2} \right) \\ 1 \quad 1 \quad \delta \quad \frac{1}{\delta} \quad \frac{1}{1} \quad 1 \quad \delta^2 \quad \frac{1}{1} \quad \frac{1}{\delta^2} \end{array} \right\} \quad (\text{C.10})$$

Two conclusions can be drawn from this equation:

- 1- The pressure gradient term is at most of order 1.
- 2- The term $\frac{\partial^2 \bar{u}}{\partial \bar{x}^2}$ is very small compared with the term $\frac{\partial^2 \bar{u}}{\partial \bar{y}^2}$ and can be neglected.

Based on the above analysis, equation (B.8) can be simplified inside the boundary layer to be as follows:

$$\bar{u} \frac{\partial \bar{u}}{\partial \bar{x}} + \bar{v} \frac{\partial \bar{u}}{\partial \bar{y}} = \frac{\bar{\rho}_c}{\bar{\rho}} \bar{E}_x - \frac{1}{\bar{\rho}} \frac{\partial \bar{p}}{\partial \bar{x}} + \frac{1}{R_L} \frac{\partial^2 \bar{u}}{\partial \bar{y}^2} \quad (\text{C.11})$$

To simplify equation (C.9), a similar order of magnitude analysis will be applied to each of its terms.

$$\left. \begin{aligned} \frac{\partial \bar{v}}{\partial \bar{x}} + \bar{v} \frac{\partial \bar{v}}{\partial \bar{y}} &= \frac{\bar{\rho}_c}{\bar{\rho}} \bar{E}_y - \frac{1}{\bar{\rho}} \frac{\partial \bar{p}}{\partial \bar{y}} + \frac{1}{R_L} \left(\frac{\partial^2 \bar{v}}{\partial \bar{x}^2} + \frac{\partial^2 \bar{v}}{\partial \bar{y}^2} \right) \\ \frac{1}{1} \frac{\delta}{\delta} & \quad \frac{\delta}{\delta} \frac{\delta}{\delta} \quad \frac{1}{1} \frac{\delta}{\delta} & \quad \delta^2 \quad \frac{\delta}{1} \quad \frac{\delta}{\delta^2} \end{aligned} \right\} \quad (\text{C.12})$$

All terms of the above equation are, at most, of order δ which makes the pressure gradient term no larger than order δ . The pressure increase across the boundary layer which would be obtained by integrating equation (C.9) to be of order δ^2 , i.e. it is very small. Thus the pressure in a direction normal to the boundary layer is practically constant and can be assumed equal to that at the outer edge of the boundary layer [42]. This pressure can be obtained by solving the potential flow around the body. Outside the boundary layer the velocity component v , the body force term, and the viscous terms are small enough to be

neglected and the velocity component u is as U which reduces equation (B.2) to the following dimensional form :

$$U \frac{dU}{dx} = -\frac{1}{\rho} \frac{dp}{dx} \quad (\text{C.13})$$

This equation expresses the pressure gradient term as function of the velocity of the potential flow around the body and this term will be zero for non accelerating flow over a flat plate at zero incidence, i.e. the model under investigation. Furthermore, from the order of magnitude balance for the two Navier-Stokes equations, it is evident that the inertia effect in the y direction is of order δ smaller than that in the x direction and so equation (C.9) may be neglected by comparison. Also, the viscous terms in the y direction are of order δ smaller than those which act in the x direction and similarly can be neglected by comparison. Summing up the above analysis to describe the fluid flow inside the boundary layer at high Reynolds number when corona discharge takes place, equation (C.5) remains unaltered, equation (C.8) can be simplified by dropping the x -component viscous term and equation (C.9) can be dropped completely at locations not very close to the electrodes. Thus, the boundary layer equations which govern the model under investigation can be written in a dimensional form as follows:

$$\frac{\partial u}{\partial x} + \frac{\partial v}{\partial y} = 0 \quad (\text{C.14})$$

$$u \frac{\partial u}{\partial x} + v \frac{\partial u}{\partial y} = \frac{\rho_c}{\rho} E_x + \frac{1}{R_L} \frac{\partial^2 u}{\partial y^2} \quad (\text{C.15})$$

Near the electrodes the y -component of the electric field E_y is of order 1. Therefore the body force term in the y -direction can not be neglected and should be balanced by other

force. In this case the fluid flow should be described by the full Navier-Stokes equations (equations 3.6.1.3, 3.6.1.4, 3.6.1.5). In the boundary layer (away from the electrodes) the effect of E_y is very small and it is adequate to use the boundary layer equations (C.14, C.15) to describe the fluid flow for the model under investigation.

APPENDIX D
ANALYTIC SOLUTION OF CHARGE DENSITY
AT THE INTERFACE BETWEEN THE TWO ELECTRODES
FOR OHMIC SURFACE

The availability of an analytic solution for the charge density distribution at the interface in the region between the two electrodes is an important tool to verify the correctness of the numerical solution at this interface and consequently in the whole computational domain where the same numerical scheme is used. In order to obtain this analytic solution for the charge density distribution at the interface in the region between the two electrodes the following assumptions will be considered:

1. The positive electrode is the only source of positive ions in the domain under investigation.
2. No ion deposition takes place from the gaseous phase to the surface current.
3. The electric field on the surface between the two electrodes is constant.
4. The gas ion mobility of air is constant.
5. The surface is ohmic.

These assumptions can be written as follows:

$$J_y = 0 \quad (D.1)$$

$$E_x|_{wall} = \frac{\Delta\phi}{L} \quad (D.2)$$

$$k = \text{constant} \quad (D.3)$$

Using the conservation of current density equation at steady state conditions and Gauss law which can be written here as:

$$\nabla \cdot \vec{J} = 0 \quad (\text{D.4})$$

$$\nabla \cdot \vec{E} = \frac{\rho_c}{\epsilon_0} \quad (\text{D.5})$$

where

$$\vec{J} = \rho_c k \vec{E} \quad (\text{D.6})$$

where k is the air mobility and ρ_c is the charge density.

Equation (D.5) can be written in two-dimensional Cartesian form as:

$$\frac{\partial E_x}{\partial x} + \frac{\partial E_y}{\partial y} = \frac{\rho_c}{\epsilon_0} \quad (\text{D.7})$$

The first term of the left hand side of equation (D.7) can be dropped since $E_x = \text{constant}$ at the interface between the two electrodes and consequently this equation can be simplified to:

$$\frac{\partial E_y}{\partial y} = \frac{\rho_c}{\epsilon_0} \quad (\text{D.8})$$

Using equation (D.6), the y-component of the electric field at the interface between the two electrodes can be written as:

$$E_y = \frac{J_y}{\rho_c k} \quad (\text{D.9})$$

Combining equations (D.3), (D.8) and (D.9) gives

$$\frac{1}{k} \frac{\partial}{\partial y} \left(\frac{J_y}{\rho_c} \right) = \frac{\rho_c}{\epsilon_0} \quad (\text{D.10})$$

Carrying out the above differentiation and using equation (D.1) gives

$$\frac{\partial J_y}{\partial y} = \frac{k}{\epsilon_0} \rho_c^2 \quad (\text{D.11})$$

Using equation (D.6) at the interface between the two electrodes the surface current at this region can be described as:

$$J_x = k \rho_c E_{x_{wall}} \quad (\text{D.12})$$

Combining equations (D.11) and (D.12) gives

$$\frac{\partial J_y}{\partial y} = \frac{1}{k \epsilon_0} \left(\frac{J_{x_{wall}}}{E_{x_{wall}}} \right)^2 \quad (\text{D.13})$$

Using equation (D.13) in equation (D.4) after writing it in two-dimensional Cartesian form at the interface between the two electrodes gives

$$\frac{\partial J_{x_{wall}}}{\partial x} + \frac{1}{k \epsilon_0} \left(\frac{J_{x_{wall}}}{E_{x_{wall}}} \right)^2 = 0 \quad (\text{D.14})$$

Dropping the suffix wall and rearranging, equation (D.14) can be written as:

$$\frac{\partial J_x}{\partial x} + \frac{1}{\varepsilon_0 k E_x^2} J_x^2 = 0 \quad (\text{D.15})$$

Defining

$$C = \frac{1}{\varepsilon_0 k E_x^2} \quad (\text{D.16})$$

equation (D.15) can be written as:

$$\frac{\partial J_x}{\partial x} + C J_x^2 = 0 \quad (\text{D.17})$$

Separating variables in equation (D.17) gives

$$\frac{dJ_x}{J_x^2} = -C dx \quad (\text{D.18})$$

Integrating equation (D.18) from J_{x_0} at x_0 to J_x at x for constant E_x (ohmic surface) gives

$$J_x = \frac{J_{x_0}}{1 + C J_{x_0} (x - x_0)} \quad (\text{D.19})$$

Combining equations (D.12) and (D.19) at the interface between the two electrodes and manipulating, equation (D.19) can be rewritten as:

$$\rho_c = \frac{\rho_{c_0}}{1 + C k \rho_{c_0} E_x (x - x_0)} \quad (\text{D.20})$$

Substituting back for the constant C by equation (D.16) and for E_x at the interface between the two electrodes by equation (D.2), equation (D.20) can be rewritten as:

$$\rho_c = \frac{\rho_{c_0}}{1 + \frac{L\rho_{c_0}(x-x_0)}{\epsilon_0 \Delta\phi}} \quad (\text{D.21})$$

where L is the gap distance and $\Delta\phi$ is the potential difference between the two electrodes respectively and ρ_{c_0} is charge density at the positive electrode.

Equation (D.21) represents the analytic solution for the charge density distribution at the interface between the two electrodes for an ohmic surface.

APPENDIX E
ELECTRIC POTENTIAL DISTRIBUTION
AT THE EXTENSION OF THE FLAT PLATE

The electric potential distribution upstream of the flat plate is described by the Laplace equation. There is insufficient boundary conditions to solve this equation at this region. Instead a conformal mapping transformation was used to transfer a solution of known problem to this problem.

A flat plate at constant electric potential ϕ_0 and a uniform electric field strength E_0 perpendicular to this flat plate are to be assumed. A transformation will be introduced to change the (x', y') plane to the (x, y) plane and consequently the angle at the origin from π to 2π as shown in Figure E.1.

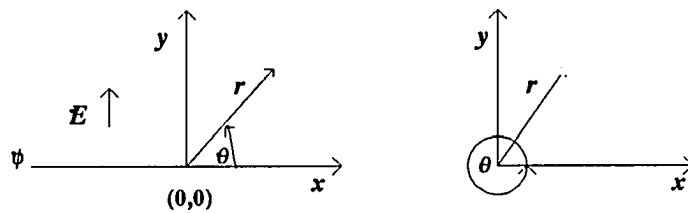


Figure E.1: Transformation of (x', y') plane to (x, y) plane

Introducing the transformation

$$w(x,y)=[z(x',y')]^n \quad (\text{E.1})$$

or

$$r e^{i\theta} = [r' e^{i\theta'}]^n \quad (\text{E.2})$$

Comparing the similar terms of both sides of equation (E.2) yields

$$n = 2 \quad (\text{E.3})$$

and consequently

$$(x + iy) = (x' + iy')^2 \quad (\text{E.4})$$

which gives

$$\begin{aligned} x &= (x')^2 - (y')^2 \\ y &= 2x'y' \end{aligned} \quad (\text{E.5})$$

To balance the units of both sides of the two equations of (E.5), a constant, which has the unit of length, will be multiplied by the left hand side of both equations which can be rewritten as:

$$\begin{aligned} cx &= (x')^2 - (y')^2 \\ cy &= 2x'y' \end{aligned} \quad (\text{E.6})$$

Combining both equations of (E.6) to omit x' we obtain

$$cx = \left(\frac{cy}{2y'}\right)^2 - (y')^2 \quad (\text{E.7})$$

Then, considering the constant electric field strength which can be defined as:

$$E_0 = - \frac{\partial \phi}{\partial y} \quad (\text{E.8})$$

Separating variables of equation (E.8) and integrating for y between 0 and y' and ϕ between ϕ_u and ϕ' we obtain

$$\phi' - \phi_u = - E_0 y' \quad (\text{E.9})$$

and assuming

$$\phi = \phi' - \phi_u \quad (\text{E.10})$$

therefore,

$$y' = - \frac{\phi}{E_0} \quad (\text{E.11})$$

Substituting (E.11) into (E.7) we obtain

$$c x = \left(\frac{c E_0 y}{2 \phi} \right)^2 - \left(\frac{\phi}{E_0} \right)^2 \quad (\text{E.12})$$

Along the extension of the flat plate where $y = 0.0$, equation (E.12) becomes

$$c x = - \left(\frac{\phi}{E_0} \right)^2 \quad (\text{E.13})$$

or

$$\phi = E_0 (-c x)^{1/2} \quad (\text{E.14})$$

Since c and E_0 are constants of unknown value, it can be concluded that:

$$\phi \approx x^{1/2} \quad (\text{E.15})$$

Since ϕ is governed by Laplace equation, it is adequate to assume

$$\phi = c_1 x^{1/2} + c_2 \quad (\text{E.16})$$

where c_1 and c_2 are constants to be determined by the boundary conditions where x positive upstream. At $x=0.0$ (at the leading edge of the flat plate) $\phi = \phi_u$ while upstream the leading edge at a characteristic length L , $\phi = 0.0$. This characteristic length is also one of the unknowns in this problem and it will be obvious to be chosen as the height, h , of the computational domain which will satisfy the boundary conditions of Poisson's equation. This decision is based on the fact that the electric potential at both locations is zero. Using these two boundary conditions in equation (E.16), the electric potential along the extension of the flat plate in the negative direction of the x -axis can be determined according to this equation

$$\phi = \phi_u \left[1 - \left(\frac{-x}{h} \right)^{1/2} \right] \quad (\text{E.17})$$

Equation (E.17) represents the electric potential distribution upstream of the leading edge up to the characteristic length, h , and upstream of h the electric potential is zero.

In this derivation it is considered that the flat plate tip is rounded and of radius larger than the radius of the corona wire to avoid corona initiation at the leading edge.

APPENDIX F
DRAG FORCE BY MOMENTUM INTEGRAL METHOD

The momentum integral method is an alternative method to calculate the drag force on a flat plate [3]. A uniform fluid flow passing over a flat plate with free stream velocity U is considered with a constant pressure throughout the flow field. An imaginary control volume is constructed over the plate as shown below in Figure F.1 where the upper section of this control volume is a stream line.

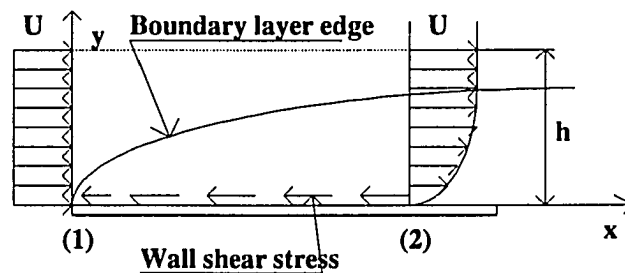


Figure F.1: Control volume on a flat plate

The flow entering the control volume at the leading edge of the plate at section (1) is uniform while the flow leaving the control volume at section (2) varies from zero at the plate surface to the free stream velocity outside the boundary layer. Applying the x-momentum equation to the steady flow of the fluid within the control volume gives

$$\sum F_x = \rho \int_{(1)} u \bar{v} \cdot \bar{n} dA + \rho \int_{(2)} u \bar{v} \cdot \bar{n} dA \quad (\text{F.1})$$

where \bar{n} is a unit vector normal to each section in outward direction and $\sum F_x$ is the net drag force that the plate exerts on the fluid.

$$\sum F_x = -D \quad (\text{F.2})$$

and

$$D = D_{vis} - F_{cor} \quad (\text{F.3})$$

where D is the net drag force due to the viscous and the corona discharge effects that the fluid exerts on the plate.

Evaluating equation (F.1) on the control volume of Figure F.1 gives

$$-D = \rho U(-U)bh + \rho b \int_0^h u u dy \quad (\text{F.4})$$

Rearranging this equation the net drag force acting on the plate can be written as:

$$D = \rho U^2 bh - \rho b \int_0^h u^2 dy \quad (\text{F.5})$$

where b is the width of the flat plate and h is the height of the control volume. Usually h is considered as the boundary layer thickness at section (2) but for the model under investigation it will be considered as the height of the computational domain.

Equation (F.5) shows the balance of the shear drag and the deficit in the momentum of the fluid flow. As the distance measured from the leading edge of the flat plate increases

the drag increases and consequently the boundary layer thickness increases to overcome the drag of the viscous shear stress on the plate.

APPENDIX G
PHYSICAL PARAMETERS

Values of some important parameters of the bulk media and the interface of the model under investigation are listed here.

Permittivity constant of free space [40]	$\epsilon_0 = 8.854 * 10^{-12} C^2 / Nm^2$
Permeability constant of free space [40]	$\mu_0 = 12.6 * 10^{-7} N / A^2$
Mobility of positive ions for dry air at STP [11]	$k^+ = 2.2 * 10^{-4} m^2 / volt.sec$
Elementary charge [40]	$q = 1.6 * 10^{-19} C$
Dielectric strength of air [40]	$E_{max} = 3 * 10^6 volt / m$
Dielectric strength of glass [44]	$E_{max} = 9 * 10^6 volt / m$
Dielectric Constant of glass [40]	$K = 5-10$
Surface Resistivity of glass in dry air [38,39]	$R' = 10^{14} ohms/square$
Surface Conductivity of glass in dry air	$\sigma_{cs} = 10^{-14} (ohms / square)^{-1}$
Air density at STP [3]	$\rho = 1.2 kg / m^3$
Dynamic viscosity of air at STP [3]	$\mu = 1.79 * 10^{-5} N.sec / m^2$
Kinematic viscosity of air at STP [3]	$\nu = 1.46 * 10^{-5} m^2 / sec$
Boltzmann constant [40]	$kk = 1.38 * 10^{-23} J / ^\circ K$